# THE INFLUENCE OF DIMENSIONAL AND DIMENSIONLESS PARAMETERS ON THE DYNAMICS OF THE HORSESHOE VORTEX UPSTREAM OF A CIRCULAR CYLINDER

By:

Manar Safar Alyas Al-Saffar

A thesis submitted in partial fulfilment of the requirements for
the degree of Doctor of Philosophy

The University of Sheffield

Faculty of Engineering

Department of Civil and Structural Engineering

August, 2016

**“Turbulence was probably invented by the Devil on the seventh day of Creation when the Good Lord was not looking”**

**Peter Bradshaw-1994**

# Abstract

Previous studies characterising horseshoe vortices upstream of circular cylinders in open channels have focused on changes in the Reynolds number. This study investigates the effect of the Froude number and other flow and geometrical parameters on the nature of the horseshoe vortex system that develops in front of a circular cylinder. The results show horseshoe vortex dynamics dominated by cylinder diameter, Froude number and flow depth. Instantaneous vorticity fields were classified into either two or three groups of vortex formations based on their turbulence stress magnitudes with a high dependence shown upon the Froude number and cylinder diameter. The peak stress properties of the horseshoe vortex system was found to be controlled within a certain threshold of Froude numbers ($\mathrm{Fr} \lesssim 0.3$ and $\mathrm{Fr} \gtrsim 1.7$). It was also found that a single point under the horseshoe vortex can represent the vortices better than the whole field that encompasses the whole system. The characteristics of the horseshoe vortex formed upstream of a wall-mounted circular cylinder in an open channel were studied using two dimensional Particle Image Velocimetry. Experiments were conducted for different flow conditions and focused on Froude numbers, cylinder diameters, flow depths and bulk flow velocities. Two groups of experiments were conducted. The first consisted of twenty five experiments with a wide range of Froude numbers, including sub-critical, critical and super-critical flow conditions. This group was analysed as a whole and then the lower sub-critical experiments followed by the upper sub-critical to super-critical experiments. Another set of nine sub-critical experiments were conducted focusing on the experimental design to segregate flow and geometrical parameters. Quadrant analysis was used to analyse the contribution of near-bed turbulent stresses in the region upstream of the cylinder. Applying multivariate statistical techniques, the relationship between geometrical parameters, flow conditions and the changes in the location and magnitude of the turbulent stresses under the horseshoe vortex were examined.

This study, introduces the Froude number as a new governing parameter of the horseshoe vortex system, which can be important for fluvial systems with change of hydraulics regimes as mountainous rivers.

**To My Family**

# Acknowledgements

The first three years of this PhD study scholarship was fully sponsored by the human capacity development program (HCDP), Ministry of Higher Education and Scientific research, Kurdistan Regional Government of Iraq. During these long four years of this research study, the author would like to show his gratitude to the following people for their contributions, encouragement, or support.

- The first supervisor, Dr. Chris Keylock for his time, advice, and support. It was my pleasure to work with him and gain experience in understanding the physical meaning of research.
- The second supervisor, Dr. Wernher Brevis for his advice, support and constructive criticism, especially with technical issues.
- The technicians in the Department of Civil and Structural Engineering for their support in the fluid mechanics laboratory, especially, Mr. Paul Osborne.
- Dr. Stuart Walker and The University of Hull for making the laser available for the PIV measurements.
- The people who were with me in rooms D106, and D105 including Dr. Will Shepherd, Dr. Simon Doncaster, Dr. Stewart Husband, Dr. Sam Fox, Dagmara Starczewska, Sally Jones, Dr. Will Furnass, Dr. Fred Sonnenwald, and Dr. Katherine Fish for the time I spent with them especially the half hour tea brake in the mornings, and Jonathan Higham for the time we spent discussing issues related to the research.
- A special thank you goes to my wife Farah Alkhayat for her encouragement, support and time she spent taking care of our two boys Michael and Matias, thanking them as well for refreshing my day, after long hours at the university, with their smile when they were waiting me at the door.
- I should not forget to thank my parents for the values that they taught me and their trust about my ability to accomplish what I am doing. My brothers and sisters, especially my brothers Masar and Syrean who were chasing my scholarship issues back home. Also I would like to thank my grandmothers, uncles and aunts, relatives and friends who always supported me and asked about the progress of my study.

Sheffield, August 2016 Manar Al-Saffar

# Contents

# List of Figures

# List of Tables

# Chapter 1

# Introduction

## 1.1 Background

The formation and dynamics of the horseshoe vortex (HV) system in front of a wall-mounted obstacle is of practical relevance due to its impact on the stability of real world structures, e.g. bridge piers and offshore wind-farm foundations. These vortex systems sometimes denoted as necklace vortex (Kirkil and Constantinescu, 2012) due to the three-dimensional shape it forms around a bluff body, where there are two primary types: laminar and turbulent. These may be discriminated based on the dimensionless Reynolds number (Re) that characterises the ratio of inertial forces to viscous forces. It is written as $\mathrm{Re} = \frac{\rho U l}{\mu}$, where, $\rho$ is the fluid density ($kg/m^3$), $U$ is the bulk velocity of flow ($m/s$), $l$ is the characteristics length ($m$), $\mu$ is the dynamic viscosity of the fluid ($kg/m.s$). The bulk flow velocity, $U = \frac{Q}{bh}$, $Q$ is the discharge ($m^3$/s), $b$ is the flume width ($m$), and $h$ is the flow depth ($m$).

According to Dargahi (1989), the HV formation is produced by the separation of the three-dimensional boundary layer, and this is induced by the adverse pressure caused by the presence of a wall-mounted bluff-body. The flow detaches from the boundary layer at the so-called separation lines. After the flow separates, it rolls up to form a vortex which then moves downstream (Sumer et al., 1997). A primary vortex is developed as a consequence of the largest flow separation and attached to it, immediately in the upstream near the wall region, a secondary vortex is also formed, as shown in Figure 1.1. The formation of these flow structures govern the amplification of the magnitude of the turbulent and wall stresses in front of the obstacle. The characteristics of the flow around cylinders have been extensively studied by different researchers (Baker, 1979, 1980; Dargahi, 1989; Sahin et al., 2007) and the common conclusion of these studies has been that the horseshoe vortex system is very complex. The formation process of the HV begins when the incoming flow rotates downwards as a result of encountering an obstacle. According to (Kirkil et al., 2008, p. 572) “a difficult aspect of local scour, is the complex, highly 3D and unsteady character of the flow field producing scour. Turbulence structures over a wide range of turbulent scales are present around the cylinder, and control the entrainment and transport of sediment from the scour hole”.

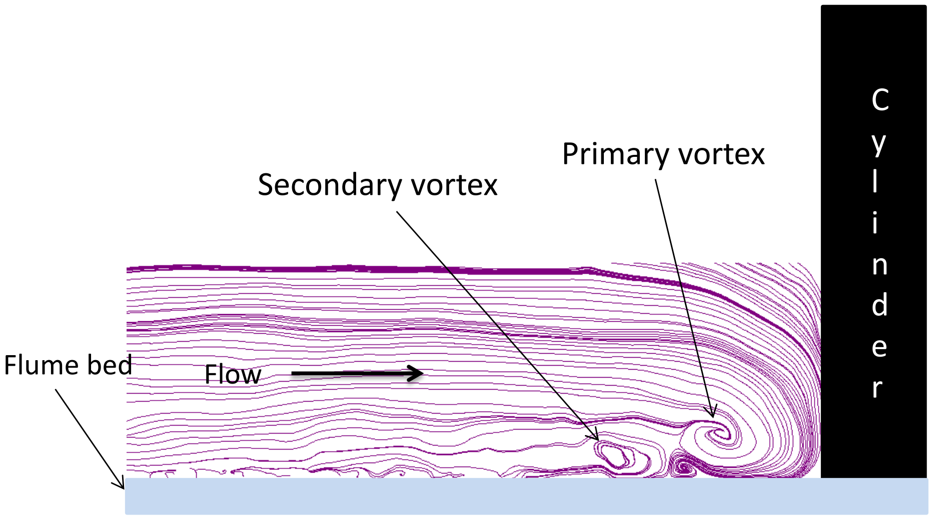

Figure 1.1: An instantaneous streamlines of horseshoe vortex system in the plane of symmetry upstream of a circular cylinder for one of the experiments of this study (dimensions are not to scale).

The problem of local scour around bridge piers and abutments is still a major factor for bridge failure due to hydraulic deficiencies (Yanmaz and Ustun, 2001), as opposed to structural deficiencies. According to Briaud et al. (1999) an accurate prediction of the scour depth and pattern is essential for the safe and economic design of bridge foundations, while (Kirkil et al., 2005*a*, p. 1) state that: A clear understanding of the scour mechanism and in particular of the structure of the horseshoe vortex system that forms at the base of the piers or abutments, is still lacking. According to Dargahi (1989) the horseshoe vortex system is the main factor that causes scouring upstream of bridge piers.

The studies above showed that the scour around cylinders is caused by the HV system which has a very complex nature that needs to be understood for better understanding of the scour mechanism. I believe that an important part of understanding this mechanism is defining the parameters that control it. Hence, this study is conducted to separate the effect of different dimensional and dimensionless parameters (Froude number Fr, $Q$, $U$, cylinder diameter $D$, $h$, cylinder diameter Reynolds number $\mathrm{Re}_D$, and flow depth Reynolds number $\mathrm{Re}_h$) on the near wall flow dynamics under the HV system. It is the hypothesis of this work that Fr has a significant supplementary control on the HV geometry and dynamics. Therefore, the experimental design of this study segregates the effect of flow and geometrical parameters on the turbulent stresses for two regions, under the HV system and across the flow field for a wide range of Fr numbers. The independent and dependent parameters of the experiments were analysed using multivariate statistical techniques (stepwise regression, Press (2012) and $K$-Means classification, Everitt et al. (2011)). While, the former was used to find the effect of the controlling parameters on the dynamics of the HV system, the latter was used to explore the effect of the same parameters on the geometry of the system.

### 1.1.1 Coherent Structures

Coherent structures (CSs) exist in most turbulent flows, including the wakes and boundary-layers found in nature (Ashworth et al., 1996; Venditti et al., 2013). They are regions of large-scale organised motion that have a relatively long lifetime with respect to intrinsic flow timescales. Coherent structures were first experimentally investigated by Grant (1958); Keffer (1965) and then Kline et al. (1967) using visualisation methods. At the same time, the presence of CSs was confirmed by the analytical study of Bakewell Jr and Lumley (1967). The recent developments in experimental techniques and computational power have permitted better investigation and understanding of the dynamics of these structures. So far, there is no clear definition for what a CS is, but Hussain (1983) said “coherent structure is a connected, large-scale turbulent fluid mass with a phase-correlated vorticity over its spatial extent”. Vortices, as examples for CSs, are common formations in turbulent flows. The existence of vortices is an old idea, however more criteria needs to be available for the identification of a vortex. Horseshoe vortices, and cylinder wake vortices are a few of many examples of a vortex formation. Following from this definition, there have been a large number of attempts to formulate local and non-local definitions of CSs from the properties of the velocity gradient tensor. Local methods (Hunt et al., 1988; Hussain, 1983; Chakraborty et al., 2005, e.g.) are typically based on the eigenvalues of this velocity gradient tensor, or tensors derived from it. Given that the vorticity field may be obtained from the velocity gradient tensor, there are clear formal connections to the notion of vorticity, although the nonlocality of the action of the pressure field and the vorticity field add an additional complexity (Chevillard et al., 2011).

### 1.1.2 Froude Number (Fr)

The Froude Number is a dimensionless parameter measuring the ratio of the inertia force on an element of fluid to the weight of the fluid element, in other words, it is the ratio between the inertia forces and the gravitational forces. It is a fundamental fluid dynamics quantity that is of immense importance in channel flows and river studies where wave and surface behaviour need to be characterised. It is typically defined as:

$$Fr = \frac{U}{\sqrt{gh}} \tag{1.1}$$

where, g is the acceleration due to gravity. The flow in open channel is classified as sub-critical, critical or super-critical if (Fr $\lesssim$ 1, Fr $\sim$ 1, or Fr $\gtrsim$ 1) respectively. For flows where Fr $<$ 0.5, an instability that develops on the free surface can be dissipated. For super-critical flow, standing waves develop that perturb the free surface and the water column beneath, affecting the formation of bedforms in mobile bed channels. For example, Simons and Richardson (1961) classified the flow in open channels with movable beds to be either lower flow regime for Fr $<$ 1 where the bedforms of lower stage plane beds, ripples, and dunes exist, or upper flow regime for Fr $>$ 1 with the existence of upper stage plane beds, in-phase wave, chutes, and pools. Although, Froude number is one of the crucial flow characteristics of open channels, no study has been conducted to show if there is any change in the characteristics of the horseshoe vortex around a cylinder as a function of Froude number. This is important because bridges or similar structures that affect flow in-channel will not be located where the Froude number remains constant for all times. Consequently, changes to scour potential as a function of horseshoe vortex modification need to be understood. Froude number is an important factor in scour depth prediction equations around bridge piers and imprecise prediction leads to a weakening of the bridge foundation during flood events, which causes bridge failure. The Colorado State University (CSU) equation 1.2 and Froehlich equation 1.3 are examples for pier scour depth prediction:

$$y_s = 2.0k_1k_2k_3k_4(a)^{0.65}(y_3)^{0.35}(Fr_3)^{0.43} \tag{1.2}$$

Where, $y_s$ is scour depth, $k_1$ is correction factor for pier nose shape, $k_2$ is correction factor for angle of attack of flow, $k_3$ is correction factor for bed condition, $k_4$ is correction factor for armouring of bed material, $a$ is pier width, $y_3$ is flow depth directly upstream of pier, and $\mathrm{Fr}_3$ is Froude number directly upstream of the pier.

$$y_s = 0.32\phi_f(a^{'})^{0.62}(y_3)^{0.47}(Fr_3)^{0.22}(D_{50})^{-0.09} + a \tag{1.3}$$

where, $a^{'}$=a(cos$\theta_p$ ) is projected pier width with respect to the direction of flow, $\theta_p$ is the angle of attack, $\phi_F$=1.3 for square-nosed piers, $\phi_F$=1.0 for round-nosed piers, and $\phi_F$=0.7 for sharp-nosed piers (Akan, 2011).

## 1.2 Thesis Aims

In this study, the main concern is with the behaviour of the horseshoe vortex system upstream of a circular cylinder, and the general aim of this work is three-fold:

1. To explore the effect of seven control parameters ( Fr, $Q$, $U$, $D$, $h$, $\mathrm{Re}_D$, and $\mathrm{Re}_h$) on the dynamics and geometry of the HV system, in different flow conditions with Fr as a reference, and isolating the controls according to the significance of their

effect.

2. Finding to what extent the Froude number has a direct or indirect effect on the HV dynamics. The parameters are shown in Table 1.1 with the reason for including each of the parameters in this study.

3. Compare the characteristics of the HV system for very low Fr (lower sub-critical flow conditions) and high Fr (upper sub-critical and super-critical flow conditions) with that of more typical natural flow conditions.

The first two aims above are strongly connected, and the answer to the second should emerge from the first. To fulfil the aims, the study has to be divided into two phases represented by two groups of experiments.

Table 1.1: The dimensional and dimensionless parameters used in the study

| Parameter | The reasons for including the parameter |
|---|---|
| Fr | It is hypothesised that free-surface deformation and vortex suppression as a function of Fr will affect the HV system. |
| $Q$ | To explore the combined effect of flow velocity and flow depth, which affect vertical pressures (head) acting on the HV system, as well as the momentum flux into the HV region. |
| $U$ | To explore the effect of incoming momentum on the HV system. |
| $D$ | A parameter found to have effect on the HV system (Dargahi, 1989) that influences the geometry of the system as a consequence of lateral momentum flux. |
| $h$ | To explore the independent effect of the remaining parameters in Fr, under constant gravity, and to examine how pressure head affects the geometry of the HV system. |
| $\mathrm{Re}_D$ | Previous work highlights its importance: (Baker, 1979, 1980; Dargahi, 1989; Rodríguez y Domínguez et al., 2006). This is because of the combined effect of incoming momentum ($U$) and the control exerted by diameter on lateral momentum flux, assuming constant viscosity. |
| $\mathrm{Re}_h$ | Previous studies included it (Dargahi, 1989), and it focuses attention on vertical momentum transport down the front of the cylinder rather than lateral fluxes. |

## 1.3 Methodology and Experimental Approach

To fulfil the above mentioned objectives, the study has been divided into two phases of experimental design which provide a control on the various flow variables, allowing us to determine the factors affecting the near wall flow dynamics with some confidence.

Firstly, in phase one, a group of experiments has been conducted with a wide range of Fr, from low sub-critical flow conditions to high super-critical flow conditions. In some cases, the Froude number was kept constant while changing the cylinder Reynolds number by varying the cylinder diameter and keeping the flow velocity constant, the results have been analysed in Chapter 3.

The second phase was the investigation of the same dynamics with lower, sub-critical flow conditions (Fr $< 0.5$), as the studies shown in the literature review section, Section 1.4, are under this range of Fr. This work was divided into three groups of experiments, in each of which different flow parameters were held constant or varied in order to provide a thorough exploration of the controls on the HV dynamics so that statistically significant effects could be elucidated, the results are presented in Chapter 4 .

The work is experimental but the approach spans the RANS and eddy-resolving frameworks in that analyses of the vorticity field in the plane of symmetry upstream of a circular cylinder are used to couple the observed flow topology (vortex formation) to the Reynolds stresses (and the quadrant decomposition thereof). Two dimensional Particle Image Velocimetry (PIV) is used to determine instantaneous flow fields for the longitudinal, $u$, and vertical, $w$, velocity components, as well as the vorticity field, (Landreth and Adrian, 1990):

$$\omega = \frac{\partial w}{\partial x} - \frac{\partial u}{\partial z}. \tag{1.4}$$

where $x$ and $z$ are the horizontal and vertical coordinates, respectively. Identification of the region affected by the HV system was performed using a Proper Orthogonal Decomposition (POD) of the PIV results, while classification of individual PIV frames was undertaken using a $K$-Means classifier.

## 1.4 Focused Literature Review

Horseshoe vortex system dynamics have been studied using experimental and numerical techniques, but also using several geometrical configurations, such as flat plates, circular and square cylinders, and triangular cross-sections (Schwind, 1962; Seal et al., 1995; Lin et al., 2002, 2003, 2008). According to Sahin et al. (2007) the circular cylinder has attracted the interest of researchers, more than other shapes, because of its relevance to industry. In addition, due to the combination between its simple geometry and the unsteadiness in the flow field induced by oscillations of the separation region or in other words of the HV system (Pattenden et al., 2005). Therefore, most of the fundamental observations of the relevant fluid dynamics are mainly related to studies of this configuration (Baker, 1979, 1980; Dargahi, 1989; Sahin et al., 2007).

In his review paper, Simpson (2001) presented important studies that have examined both laminar and turbulent junction flows. As a consequence of the pressure drop around an obstacle, a three-dimensional separation occurs, which is different for the laminar and turbulent cases. In the latter case, this mechanism is responsible for the high turbulent intensities, fluctuations of the surface pressure, and the scouring upstream of the obstacle in case of movable beds.

Existing studies may be classified as experimental and numerical. The section on experimental studies shows how research in the area has developed and how it relates to our experimental study. The section on numerical studies highlights the limitations of current numerical simulations when the Froude number is high.

### 1.4.1 Experimental Studies

Most of the previous studies that have examined various aspects of horseshoe vortex systems are similar in their flow conditions and the range of Reynolds number used. Thus, these experimental studies either do not refer to the Froude number, or have been performed under sub-critical flow conditions. One of the first works that studied the characteristics of flow around a circular cylinder was by Fage and Falkner (1931), where they used a wind tunnel with three circular cylinders of 0.0744 $m$, 0.1496 $m$ and 0.2261 $m$

in diameter. They noticed that for a 0.0744 $m$ diameter cylinder, the flow characteristics (boundary layer thickness, pressure coefficient, and surface friction), with the exception of the surface friction, were not affected by the change in Reynolds number. However, for the other two cylinder sizes the flow characteristics changed progressively with the Reynolds number.

Roshko (1961) used a circular cylinder of 0.457 $m$ diameter in a pressurised wind tunnel and he tested the drag force coefficient for Reynolds numbers between $10^6$ and $10^7$ noticing that the drag coefficient increased with the Reynolds number to reach 0.7 at $\text{Re} = 3.5 \times 10^6$, where upon it remained constant. At this same threshold, obvious vortex shedding occurred at a Strouhal number (Sr) of 0.27 ($\text{Sr} = \frac{fD}{U}$, where, $f$ is the frequency). Baker (1979, 1980) noticed from flow visualisations and pressure measurements, upstream of a circular cylinder of diameter $D$, that up to six vortices were generated from the oscillation of the HV system. From laminar flow measurements, he found that the oscillations of the HV system become irregular as the Reynolds number based on cylinder diameter $\text{Re}_D = UD/\nu$, where $\nu$ is the kinematic viscosity, increased and concluded that these oscillations were not a result of cylinder wake vortex shedding. From his study under turbulent conditions, Baker (1980) studied the flow around different circular cylinders with diameters of 0.025 $m$ to 0.101 $m$ using oil and smoke visualisation technique. His study was undertaken for a range of cylinder diameter Reynolds numbers (4000 to 90 000). He noticed from his oil-flow visualisation that only four vortices exist (0,1,1‘, and 2) as shown in Figure 1.2.

Thomas (1987) found from his experimental study that the vortex shedding in front of a cylinder is controlled by the convection and stretching of the mean flow near the cylinder, which is a function of cylinder diameter.

Dargahi (1989) studied the HV system around a cylinder of $D = 0.15$ $m$ in a flume with a fully turbulent flow with flow depth Reynolds number, $\text{Re}_h$, ranging from 6600 to 65000 and Froude number ranging from 0.05-0.21. He found that while the number of vortices was a function of $\text{Re}_h$, the size of the vortices was dependent only on the cylinder diameter. He also noticed that the HV system was shedding in a quasi-periodically way, independently of the wake vortices. Figure 1.3 shows a vertical plane at the line of symmetry (a) and a horizontal plane view for the formation of the HV system (b).

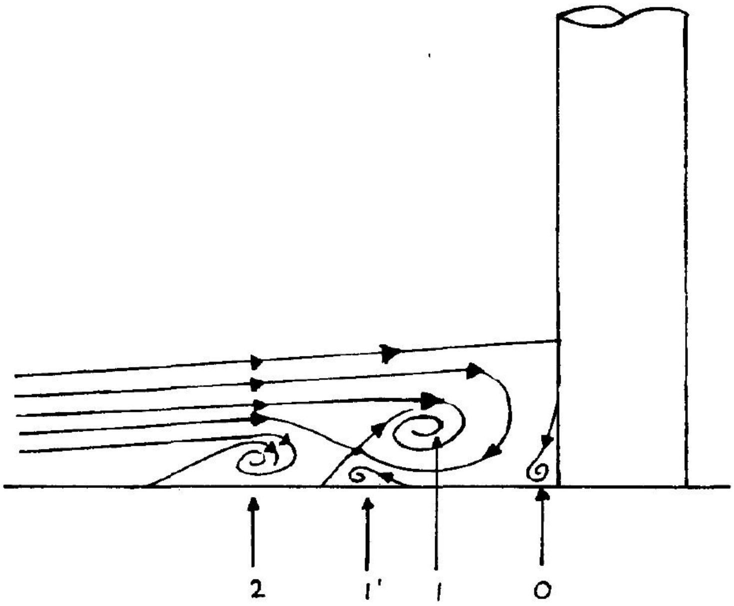

Figure 1.2: The four vortices of HV system (Baker, 1980).

Greater detail on the relevant process mechanics have emerged in subsequent studies working at greater spatial and temporal resolution.

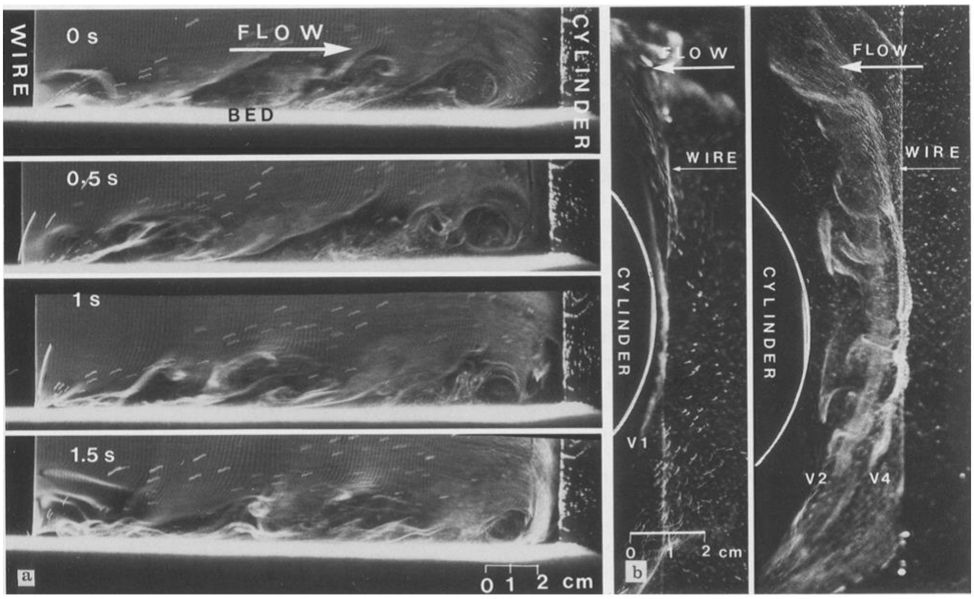

Figure 1.3: a- Vertical plane view for the HV system at the line of symmetry upstream of the cylinder, b- Horizontal plane view close to the bed (Dargahi, 1989).

For example, Devenport and Simpson (1990) investigated the turbulent boundary layer in front of a cylindrical wing mounted normally to a flat surface. Their objective was to explore the time-dependent and time-averaged turbulent structure in the region. Close to the cylinder they found turbulent stresses with values many times larger than the ones observed in normal turbulent flows.

Baker (1991) re-analysed existing experimental data from different sources (Roper (1967); Norman (1972); Baker (1979, 1980); Sharma (1988)) and mainly focused on the phenomenon of the oscillatory behaviour of the HV when it is undergoing a transition from low Reynolds number, where the steady laminar HV exists, to higher Reynolds number where fully turbulent HV occur. In his study, Baker re-analysed the data according to two hypotheses: the HV oscillations are either because of the whole vortex system oscillations; or, because of the instabilities of the HV core. Both types of oscillation were found to exist as a function of spatial position and effective cylinder width. Roulund et al. (2005) investigated numerically and experimentally the influence of the flow depth, Reynolds number, and bed roughness on the HV system, Fr ranged between 0.2 and 0.5 in the study. They found the influence of $\mathrm{Re}_D$ on HV to be significant. In the laminar regime, the HV size and bed shear stress under the system were found to increase with higher $\mathrm{Re}_D$, but the situation was the opposite in turbulent flows where the HV size and bed shear stress decreased with increasing $\mathrm{Re}_D$. Also, the results showed an increase in the size of the HV and bed shear stress with an increasing ratio between the thickness of the boundary layer and cylinder diameter $h/D$. Above a certain threshold, no changes on the size and bed stresses were found and no significant effects of the bed roughness on the HV size and the bed shear stress were found. Roulund et al. (2005) also found that the scour depth was influenced by the Froude number.

An experimental study by Rodríguez y Domínguez et al. (2006) used a laser illumination of seeded particles to visualise the horseshoe vortices in front of a circular cylinder ($D = 0.05\ m$) between two parallel plates, using different $\mathrm{Re}_D$ and different height to width ratios. Four regimes of the HV system were shown: (i) steady vortex systems with variation of the number of vortices present; (ii) oscillatory vortex system; (iii) amalgamating vortex system; and, (iv) the breakaway vortex system. The frequency of periodic vortices (which scaled with the Strouhal number) was also studied, and as the Reynolds number was increased, a systematic growth of the dimensionless frequency was observed. The study showed that height to diameter ratio has a significant effect on the behaviour of the vortex system for a dimensionless height of the cylinder is less than or equal to 1.

The number of vortices and their strength was increased with a greater height to diameter ratio, until a threshold, at which the vortex system properties remained constant. This showed that for tall cylinders the flow became independent of the height to diameter ratio. In this study sufficiently tall cylinders will be used to ensure the independence from cylinder height effects. Sahin et al. (2007) studied the behaviour of the horseshoe vortex system around a circular cylinder using high-image density particle image velocimetry by generating the laser plane at four different elevations. The measurements were under a constant diameter Reynolds number of $\mathrm{Re}_D = 4000$. The results showed that the dimensionless Reynolds stress covariances $u'v'/U^2$, where $u'$ and $v'$ are the velocity fluctuations in the stream-wise and span-wise directions respectively. It was found that studying the behaviour of the HV system at all elevations is important as the turbulence quantities varied with elevation.

### 1.4.2 Numerical Studies

In the 1990s, numerical studies of flow around circular bodies started to emerge when Richardson and Panchang (1998) and Olsen and Kjellesvig (1998) used a hydrodynamic model for modelling three dimensional flow and scour around a circular cylinder mounted in a sand bed flume. The former used a $k$-$\epsilon$ turbulence model, and for the latter a computational fluid dynamics model named FLOW-3D® was used. The results were compared with the laboratory observations as well as with empirical formulae for local scour. In studies by Song and Yuan (1990), Tseng et al. (2000), Travin et al. (2000), Wang and Moin (2002), Salaheldin et al. (2004), Roulund et al. (2005), Kirkil et al. (2005*a*,*b*, 2006, 2008, 2009), Paik et al. (2007, 2010), Escauriaza and Sotiropoulos (2011) Khosronejad et al. (2012), the Navier-Stokes equation was used and different numerical simulation methods conducted, like Reynolds Average Navier-Stokes equations (RANS), Large Eddy Simulation (LES), Detached Eddy Simulation (DES) and Direct Numerical Simulation (DNS), to simulate different flow conditions.

Recently many more numerical studies have been conducted to characterise the HV system. Kirkil et al. (2005*b*) studied the structure of HV system around wall mounted circular cylinders, in a shallow open channel with a fixed bed, using LES with a fully turbulent

inflow boundary conditions and $\mathrm{Re}_D$ of 18000. The main finding of their study was that the structure of the HV system changes with time in a non-linear manner, and the turbulent kinetic energy and pressure fluctuations near the bed and the bed shear stress values increased beneath the HV system. In their study, Constantinescu and Koken (2005) also used LES to study the physical behaviour of the HV system, and they found that in a laminar boundary layer case, the HV system structure is organised and periodic, while in the case of a turbulent boundary layer, a broad range of coherent structures exist inside the HV system and its velocity and pressure power spectra contains a wide range of energetic frequencies. Also they found in their study that the maximum values of bed shear stress exist under the HV system.
Kirkil et al. (2005*a*) found from their study that the bed shear stress, turbulent kinetic energy, and pressure fluctuation levels close to the bed increased as a result of the general effect of the HV system, and the effect of this in mobile bed conditions is to scour the bed material away from the area where the HV is developed. Although the study of Chang et al. (2011) using DES was for a non-circular cylinder, it is a very important study because it showed the importance of instantaneous flow fields rather than the mean flow field on the scour dynamics. Comparing their study results with others based on RANS, they found that the sediment entrainment from around the cylinder was increased by 50%.
Escauriaza and Sotiropoulos (2011) studied a configuration based on the experimental results of (Dargahi, 1989) using DES at two different Reynolds numbers. The researchers found that the HV dynamics were different for the smaller Reynolds number than in the larger one. From the comparison of the instantaneous flow fields for $\mathrm{Re}_D$=20000 with $\mathrm{Re}_D$=39000, they found that the flow separation happens earlier and that five vortical structures formed the HV system, which are more periodic and more organised for the higher Reynolds number. In addition, the shedding of the vortex is more frequent, and the mode of hairpin instability is weaker, with smaller magnitude eruptions of the wall vorticity occurring. The same is also the case for the pockets of concentrated high instantaneous shear stress upstream of the cylinder.

However, there was either no reference to the Froude number or it was less than 0.5, the only numerical study so far that has used a high Froude number was by Kawamura et al.

(2002) for three different Froude numbers of 0.2, 0.5 and 0.8. They used LES to investigate the interaction between the surface waves and the viscous wakes underneath them in a turbulent flow around a free surface circular cylinder. From the computational results, the researchers found that periodic vortex shedding weakened close to the free surface at high Froude number. However, the region where the periodic wake vortex shedding attenuated extended to about one cylinder diameter below the mean flow level, implying that near the wall, Froude number effects are not significant, except for particularly shallow flows.

## 1.5 Conclusion

The experimental and numerical studies, that have been conducted to characterise the horseshoe vortex system refer in many cases to the dimensional parameters as effective factors on the dynamics of the HV system, hence, in this work every single parameter is taken into consideration to find out which of these factors are the most effective. The hypothesis of this work is based on that Fr plays a significant role, alongside other parameters on the HV geometry and dynamics. Therefore, the experimental design of this study is done to segregate the effect of flow and geometrical parameters on the turbulent stresses for both regions under the HV system and across the flow field for a wide range of Fr, including the lower part of sub-critical flow conditions ($\mathrm{Fr} < 0.2$) and the upper part of the sub-critical, as well as critical, and super-critical flow ($\mathrm{Fr} > 0.6$), in which the literature shows a clear lack of studies. To find out which of the flow and geometry parameters in the experiments are affecting the HV system, various analysis of ten parameters with a physical meaning have been done. Those parameters have been extracted from the near-bed turbulent stresses in the region where the HV system exists. The idea of analysing the near-wall turbulent stresses is due to the fact that they are characteristics of the HV system and as a consequence, they define the scouring potential.

## 1.6 Thesis Structure

The thesis consists of five chapters:

Chapter one has outlined an introduction to the study area and the aim and objectives of the study. Also, a focused literature review has been presented on the studies that have been conducted in this area of research, both experimentally and numerically. This has highlighted the lack of work on Froude number effects. This will provide a justification for the approach taken in this study.

Chapter two will focus on the experimental work and methods, in particular the apparatus used in the study, specific details of the laboratory work will be explained, and the research design details will be provided. Data pre-processing and analysis methods will also be discussed. In Chapters three and four the results on the HV system and the near-bed turbulent stresses upstream of the cylinders for different groups of experiments will be presented with discussion section at the end of each chapter. In the former, a full range of flow conditions from sub-critical, critical to super-critical will be considered. The latter chapter focuses on a group of 9 experiments designed under lower sub-critical flow conditions to permit the various potential controls on the dynamics to be isolated. Finally, Chapter five will focus on the conclusions of the research, limitations and the future work needed.

# Chapter 2

# Experimental Approach and Methodology

## 2.1 Objectives and Structure of the Chapter

The main objectives of this chapter are:

1. Section 2.2 - To describe the water flume and the cylinder models used in the experiments;
2. Section 2.3 - To explain the experimental design, which considers different flow conditions (from sub-critical, through critical, to super-critical) and systematically varies conditions for selected sub-critical Froude numbers;
3. Section 2.4 - To provide a technical description of the PIV system used to measure the velocity of flow, which includes:
   (a) Operation principles and system components;
   (b) High quality PIV data;
4. Section 2.5 - To determine the necessary minimum sampling length of the experiments, which ensures that the recorded data is enough to capture the dynamics of the flow (hence, convergence based on cumulative summation and on integral time scale statistics have been applied);

5. Section 2.6 - To describe the data processing methodology;
    (a) Defining the region affected by the horseshoe vortex system;
    (b) Quadrant analysis;
    (c) Stepwise regression;
    (d) $K$-Means classification;
6. Section 2.7 - To give summary of this chapter and what is coming in the next chapters;

## 2.2 Introduction

The experiments for this study were conducted in the fluid mechanics laboratory, at the Civil and Structural Engineering Department, The University of Sheffield, in The United Kingdom. The slope-adjustable recirculating flume is 16 $m$ long, 0.5 $m$ wide and 0.5 $m$ deep. The flume is made from a steel frame with fully glass walls and bottom, allowing the laser sheet to be oriented at different angles, including illumination from the bottom and imaging access from the side. The glass provides a smooth bed for the development of the HV system, independent of roughness considerations. The flume glass roughness is 0.0015 $mm$ and that equates in all the experiments to 0.004% or less of the boundary layer thickness, which according to Townsend (1976) and Castro (2009), can be considered hydro-dynamically smooth.

The water was pumped into the flume by a recirculating pump with an inlet connected to the water tank and an outlet to the upstream end of the flume. The discharge ranged from $0.007 - 0.04$ $m^3 s^{-1}$ and was controlled by a mechanical valve that opened and closed due to pressure supplied by an air compressor. This was in turn controlled from a desktop computer using a *LabView* software. An electromagnetic flow meter was used to measure the flow rate supplied to the flume. The flume was connected to a water tank with a capacity of 14.5 $m^3$ and dimensions of 5.0 $m$ long, 1.1 $m$ height and 2.65 $m$ width. The flow depth was controlled by a tail gate at the end of the flume. A honeycomb of 0.1 $m$ thick was installed at the inlet, along with a foam panel of 1 $m$ length, 0.5 $m$ width, and 0.07 $m$ thickness with a 1 $kg$ weight on top. These damped any water surface undulation and the impact of the pump on flow characteristics. The fully developed section was found to be 7-9 $m$ from the inlet and Fig. 2.1 shows a schematic diagram of the flume with the relevant details.

There were 13 cylinder models made from circular cross-section acrylic tubes of different diameters (Fig. 2.2). They were 0.5 $m$ long and painted with a matte black paint to avoid any reflection of the laser light. The cylinder needed to be heavy enough to remain stable against the flowing water, so a stainless steel shaft of 0.25 $m$ length was fixed inside each cylinder. The cylinders were mounted vertically on the bed along the longitudinal centre-line of the flume in the fully developed section, 8 $m$ downstream the flume inlet.

A PIV system mounted adjacent to the flume was used to measure the two-dimensional velocity fields in the plane of symmetry, upstream of the surface mounted cylinders, with an acquisition frequency of 15 Hz. There are many studies about the HV system using the plane of symmetry to represent its characteristics (Baker, 1979, 1980; Devenport and Simpson, 1990; Lin et al., 2002, 2003; Rodríguez y Domínguez et al., 2006; Kirkil et al., 2006; Sahin et al., 2007; Escauriaza and Sotiropoulos, 2011). The dynamics at the plane of symmetry in front of the cylinder, showed a good representation of the HV system (Escauriaza and Sotiropoulos, 2011). According to laser safety regulations, the PIV system as well as the flume were encased by wooden panels. Figure 2.3 shows the laser safety covering.

The experimental aim is to collect high quality data from the plane of symmetry just upstream of the cylinder, very close to the bed, where the HV system is active and upstream of that region, to provide a control case. Hence, using these data, it became possible to analyse the controls on the dynamics and geometry of the HV system.

## 2.3 Experimental Design

Previous research has rarely adopted an experimental design that permits the separation of the controls upon the geometry and dynamical properties of the HV system. For example, Dargahi (1989) made use of a single cylinder diameter, making it difficult to

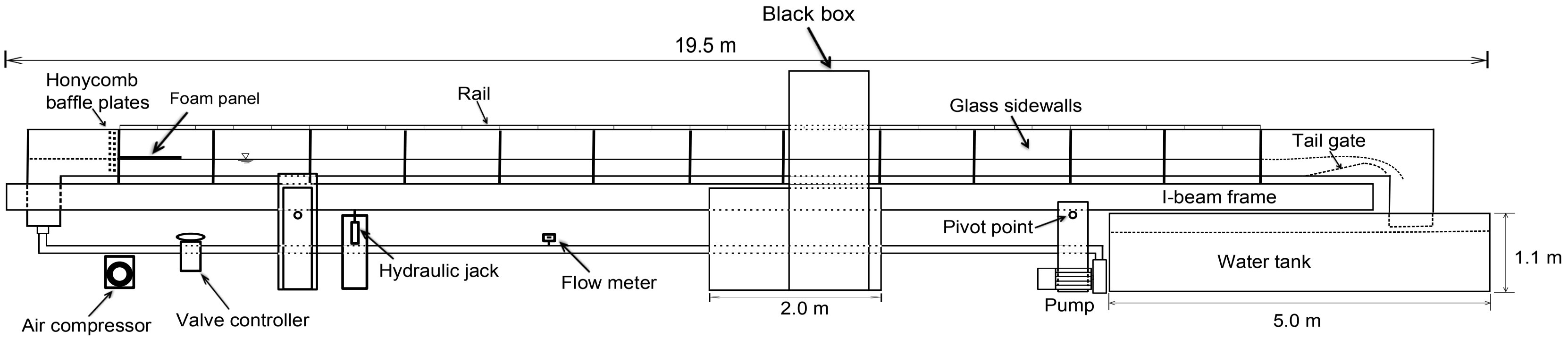

Figure 2.1: A schematic diagram of the water flume showing details of the main parts.

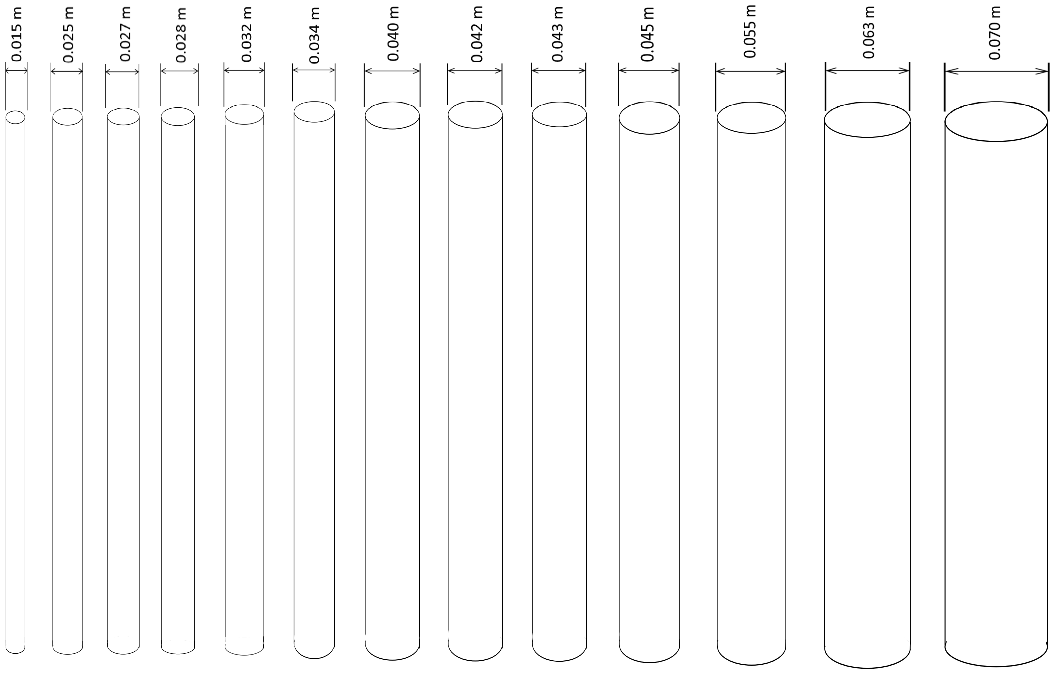

Figure 2.2: The thirteen cylinders used in the study, each with a different diameter. They scaled for the reference of the reader.

Figure 2.3: Water flume covered by wooden panels for laser safety requirements as well as the box enclosing the PIV system.

separate out the effects due to $\mathrm{Re}_D$ and $\mathrm{Re}_h$ as the former was altered purely by changes in $U$. Other studies Devenport and Simpson (1990); Simpson (2001); Escauriaza and Sotiropoulos (2011) found a dependence upon $\mathrm{Re}_D$, but also adopted a single cylinder diameter. It is clearly the case that the dynamics of the *wake* depend upon $\mathrm{Re}_D$ because diameter controls the size of the flow structures in the $X-Y$ plane, while their advection is controlled by $U$. However, in the plane-of-symmetry at the front of the cylinder, the primary vorticity is oriented in the $X-Z$ plane and, as a consequence, it does not necessarily follow that in this region, the dynamics are a function of $\mathrm{Re}_D$.

The experiments of this study were designed so that the effect of the various flow variables on the flow structure and stress distributions could be determined. There were two groups of experiments designed as follows:

### 2.3.1 Sub-critical to Super-critical Flow Conditions (Fr $\in \{0.015-2.46\}$)

This part of the study was designed to cover a wide range of Froude numbers and then divided into two parts of experiments. The first one covered the low Froude numbers ranging from $0.015-0.2$, and listed as numbers 1 to 11 in Table 2.1. The second part of experiments covered sub-critical, critical, and super-critical flow conditions with Fr ranging from $0.6-2.46$ and represented by experiments 15 to 25 in Table 2.1. In addition, all twenty five experiments were also considered simultaneously; these experiments permit us to understand the effect of a wide range of Fr with an opportunity to discriminate between the various potential controls on the dynamics of HV system. The twenty five experiments include seventeen choices of Froude number $\mathrm{Fr} \in \{0.015, 0.02, 0.03, 0.04, 0.05, 0.059, 0.10, 0.15, 0.20, 0.4, 0.6, 0.8, 1.0, 1.2, 1.4, 1.934, 2.46\}$. Across these groups of experiments, there was control of:

- $Q$, $D$ and $\mathrm{Re}_h$, (Group 1);
- Fr, $Q$, $U$, $h$, and $\mathrm{Re}_h$ (Group 2);
- $\mathrm{Re}_D$ (Group 3).

- Fr, $Q$, $U$, $h$, and $\mathrm{Re}_h$ (Group 4);
- Fr, $Q$, $U$, $h$, and $\mathrm{Re}_h$ (Group 5); and,
- Fr, $Q$, $U$, $h$, and $\mathrm{Re}_h$ (Group 6);

### 2.3.2 Selected Sub-critical Flows (Fr $\in \{0.2, 0.35, 0.5\}$)

The experimental design for three selected sub-critical Froude numbers permitted us to discriminate between the various potential controls on the HV system in addition to the potential Froude number effect. Nine experiments were undertaken in total for three choices of Froude number: Fr $\in \{0.20, 0.35, 0.50\}$ (Table 2.2). Across these sets of experiments, there was control of:

- $Q$, $D$ and, $\mathrm{Re}_h$ (Group 1);
- $U$, $D$, and, $\mathrm{Re}_D$ (Group 2); and,
- $h$, and $\mathrm{Re}_D$ (Group 3).

Although, there are a restricted number of cases considered, this experimental design was useful for applying multivariate statistical techniques (stepwise regression and $K$-Means in our case) to identify the controlling variables from a limited number of experiments by systematically varying each of the variables.

## 2.4 Particle Image Velocimetry (PIV)

PIV was used to measure the flow velocity in all of the experiments of this study. The technique was selected to obtain non-intrusive Synoptical time series, allowing the analysis of spatial-temporal characteristics of the flow (Lin et al., 2002, 2003; Hill and Younkin, 2006; Rodríguez y Domínguez et al., 2006; Gurka et al., 2006; Sahin et al., 2007, 2010; Adrian and Westerweel, 2011). PIV may be used for discovering flow physics and for providing quantitative data for validating the computational simulation of complex flows

Table 2.1: Flow conditions of sub-critical, critical and super-critical flow experiments conducted in the laboratory.

| Exp. | Group | Fr | $Q$ $(m^3s^{-1})$ | $U$ $(ms^{-1})$ | $h$ $(m)$ | $D$ $(m)$ | $\mathrm{Re}_D$ | $\mathrm{Re}_h$ |
|---|---|---|---|---|---|---|---|---|
| 1 | 1 | 0.015 | 0.007 | 0.031 | 0.446 | 0.055 | 1705 | 13826 |
| 2 | 1 | 0.020 | 0.007 | 0.038 | 0.368 | 0.055 | 2090 | 13984 |
| 3 | 1 | 0.030 | 0.007 | 0.050 | 0.281 | 0.055 | 2750 | 14050 |
| 4 | 1 | 0.040 | 0.007 | 0.060 | 0.232 | 0.055 | 3300 | 13920 |
| 5 | 1 | 0.050 | 0.007 | 0.070 | 0.200 | 0.055 | 3850 | 14000 |
| 6 | 2 | 0.059 | 0.032 | 0.130 | 0.493 | 0.015 | 1950 | 64090 |
| 7 | 2 | 0.059 | 0.032 | 0.130 | 0.493 | 0.025 | 3250 | 64090 |
| 8 | 2 | 0.059 | 0.032 | 0.130 | 0.493 | 0.055 | 7150 | 64090 |
| 9 | 3 | 0.100 | 0.023 | 0.166 | 0.278 | 0.043 | 7138 | 46148 |
| 10 | 3 | 0.150 | 0.021 | 0.210 | 0.200 | 0.034 | 7140 | 42000 |
| 11 | 3 | 0.2 | 0.021 | 0.255 | 0.165 | 0.028 | 7140 | 42075 |
| 12 | 4 | 0.4 | 0.015 | 0.361 | 0.0.083 | 0.025 | 9025 | 29963 |
| 13 | 4 | 0.4 | 0.015 | 0.361 | 0.0.083 | 0.042 | 15162 | 29963 |
| 14 | 4 | 0.4 | 0.015 | 0.361 | 0.0.083 | 0.055 | 19855 | 29963 |
| 15 | 5 | 0.60 | 0.015 | 0.476 | 0.063 | 0.025 | 11900 | 29988 |
| 16 | 5 | 0.60 | 0.015 | 0.476 | 0.063 | 0.042 | 19992 | 29988 |
| 17 | 5 | 0.60 | 0.015 | 0.476 | 0.063 | 0.063 | 29988 | 29988 |
| 18 | - | 0.80 | 0.021 | 0.641 | 0.0655 | 0.032 | 20512 | 41986 |
| 19 | 6 | 1.00 | 0.021 | 0.75 | 0.056 | 0.027 | 20250 | 42000 |
| 20 | 6 | 1.00 | 0.021 | 0.75 | 0.056 | 0.045 | 33750 | 42000 |
| 21 | 6 | 1.00 | 0.021 | 0.75 | 0.056 | 0.063 | 47250 | 42000 |
| 22 | - | 1.20 | 0.021 | 0.84 | 0.050 | 0.025 | 21000 | 42000 |
| 23 | - | 1.40 | 0.016 | 0.853 | 0.0375 | 0.025 | 21325 | 31988 |
| 24 | - | 1.934 | 0.038 | 1.407 | 0.054 | 0.04 | 56280 | 75978 |
| 25 | - | 2.46 | 0.038 | 1.652 | 0.046 | 0.04 | 66080 | 75992 |

Table 2.2: Flow conditions for the selected experiments at sub-critical Froude numbers conducted in the laboratory.

| Exp. | Group | Fr | $Q$ $(m^3s^{-1})$ | $U$ $(ms^{-1})$ | h $(m)$ | D $(m)$ | Re$_D$ | Re$_h$ |
|---|---|---|---|---|---|---|---|---|
| 26 | 1 | 0.20 | 0.0075 | 0.181 | 0.083 | 0.060 | 10860 | 15023 |
| 27 | 1 | 0.35 | 0.0075 | 0.268 | 0.056 | 0.060 | 16080 | 15008 |
| 28 | 1 | 0.50 | 0.0075 | 0.326 | 0.046 | 0.060 | 19560 | 14996 |
| 29 | 2 | 0.20 | 0.0370 | 0.308 | 0.240 | 0.045 | 13860 | 73920 |
| 30 | 2 | 0.35 | 0.0120 | 0.308 | 0.078 | 0.045 | 13860 | 24024 |
| 31 | 2 | 0.50 | 0.0060 | 0.308 | 0.039 | 0.045 | 13860 | 12012 |
| 32 | 3 | 0.20 | 0.0130 | 0.211 | 0.123 | 0.070 | 14770 | 25953 |
| 33 | 3 | 0.35 | 0.0230 | 0.374 | 0.123 | 0.040 | 14960 | 46002 |
| 34 | 3 | 0.50 | 0.0330 | 0.537 | 0.123 | 0.028 | 15036 | 66051 |

(Christensen and Scarano, 2015).

The following sections cover the operation principles and hardware components of the PIV system. Attention is also paid to the system settings and parameters, which may be adjusted to acquire high quality images. The sections that follow, explain the pre-and post-processing steps that were implemented in this study.

### 2.4.1 Operation Principles and System Components

In this study, a Dantec Dynamics commercial PIV system controlled by *DynamicStudio* v3.31 was used to measure velocity field upstream of the wall-mounted cylinders. A typical PIV system consists of four main parts: A laser source, camera(s), synchronizer and a personal computer. A double pulse Nd:YAG laser operating at a maximum of 15 Hz (i.e. fifteen pairs of frames a second) and manufactured by *New Wave Research* (model Solo 120 15 Hz) was used. The laser had a pulse width of 3-5 $ns$ and a beam diameter of 4.5 $mm$, producing a green light of 532 $nm$ wave length with maximum energy output of 120 $mJ$. The aforementioned system was used to measure two velocity components (stream-wise, $u$ and vertical, $w$) within the plane of symmetry upstream of the cylinder. Figure 2.4 shows the setup for the experiments; the laser sheet was kept to a width of $\sim 1$ $mm$ by using first a spherical lens, followed by a cylindrical lens with a negative focal length. The horizontal laser plane was reflected by using a mirror tilted by 45°,

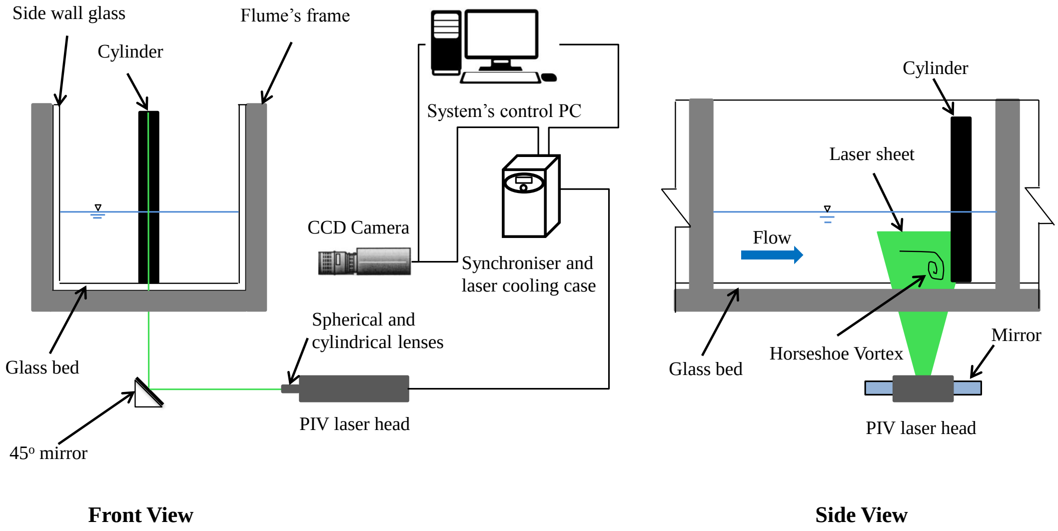

Figure 2.4: Setup of the PIV system showing the laser plane upstream to the cylinder with other system components.

as shown in Fig. 2.5. The water was seeded with $d_{50} = 21\ \mu\ m$ diameter and density 1.016 $g/cm^3$, natural colour, polyamide 12 particles. More information about the seeding particles can be found in Adrian and Westerweel (2011). The images were recorded using a Dantec Dynamics digital camera (*FlowSenseEO_2M*) of 1200 by 1600 pixel resolution with a maximum acquisition rate of 44 frames per second and a pixel depth of $8-14$ bits/pixel. The lens adopted was a PC-E NIKKOR 24 $mm$ f/3.5D ED wide-angle tilt-shift adaptor from Nikon. *DynamicStudio* v3.31 software from Dantec was used to derive the velocity fields.

The operation of the PIV system starts when a pulse of the laser illuminates the seeding particles in the flow, and the camera records the scattered light. Then, after a very short time, a second laser pulse is triggered and the second image in the pair is obtained. The image pairs are divided into interrogation areas, where the initial interrogation areas were 64 by 64 pixels, with a 50% relative overlap with the neighbouring interrogation area in both horizontal and vertical directions. Using a multi-pass approach, this was subsequently reduced to 32×32 pixels interrogation areas with the same degree of overlap. For local neighbourhood validation a local median was used direct and with a low-pass Gaussian filter (Westerweel and Scarano, 2005). The normalised cross-correlation between two interrogation areas of two images is:

$$R(F_1, F_2) = \frac{1}{N_a - 1} \sum \frac{(F_1(i,j) - \overline{F}_1)(F_2(i,j) - \overline{F}_2)}{\sigma(F_1)\sigma(F_2)} \tag{2.1}$$

where, $N_a = I \times J$ and $i = 1, \ldots, I$, $j = 1, \ldots, J$, $F_1$ and $F_2$ are the $N_{ai,j}$ interrogation areas for images 1 and 2, $\overline{F}_1$ and $\overline{F}_2$ are the pixel mean values for each interrogation area, and $\sigma(F_1)$ and $\sigma(F_2)$ are the standard deviations of the pixels in each interrogation area. Because convolution operations are implemented more rapidly in the Fourier domain, the cross-correlation between each interrogation area is undertaken using the Fast Fourier Transform. Peak matching gives the displacement distance, while the known time between image pairs permits a velocity vector to be derived (Fig. 2.6). For each pair of frames, a velocity field is created and Fig. 2.7 shows such a velocity field from one of the experiments (Fr $= 0.2$, $D = 0.06\ m$).

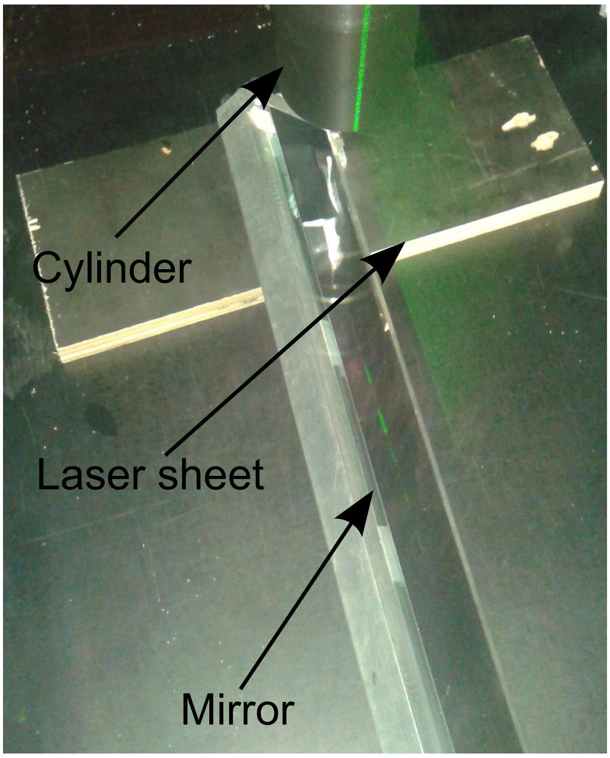

Figure 2.5: The green laser sheet at the vertical plane of symmetry reflected by a mirror upstream of a cylinder painted with matte black paint to reduce the reflections of the laser light.

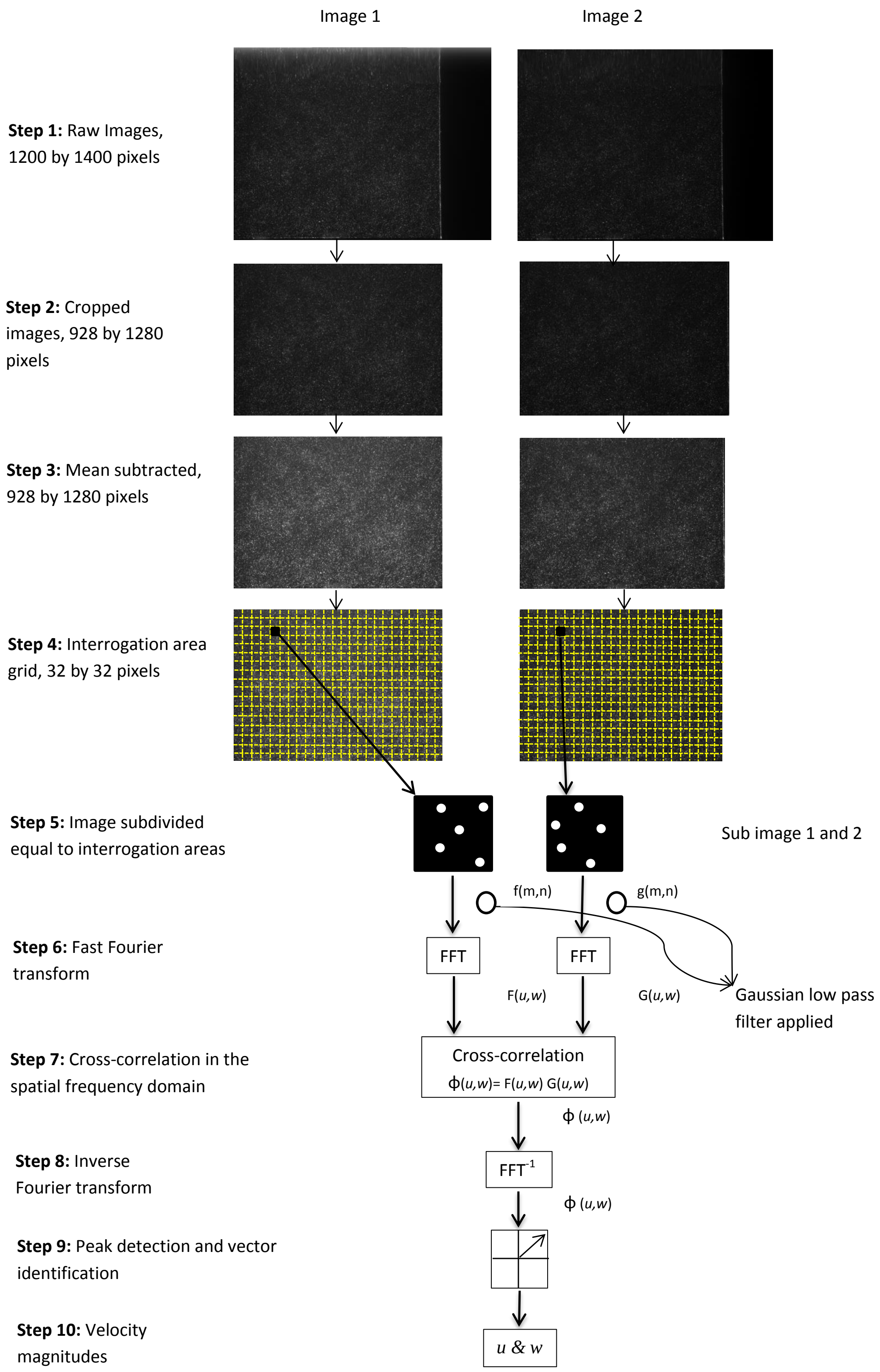

Figure 2.6: A flow chart showing the steps applied to the raw PIV images to obtain a velocity vector for each interrogation area in the image.

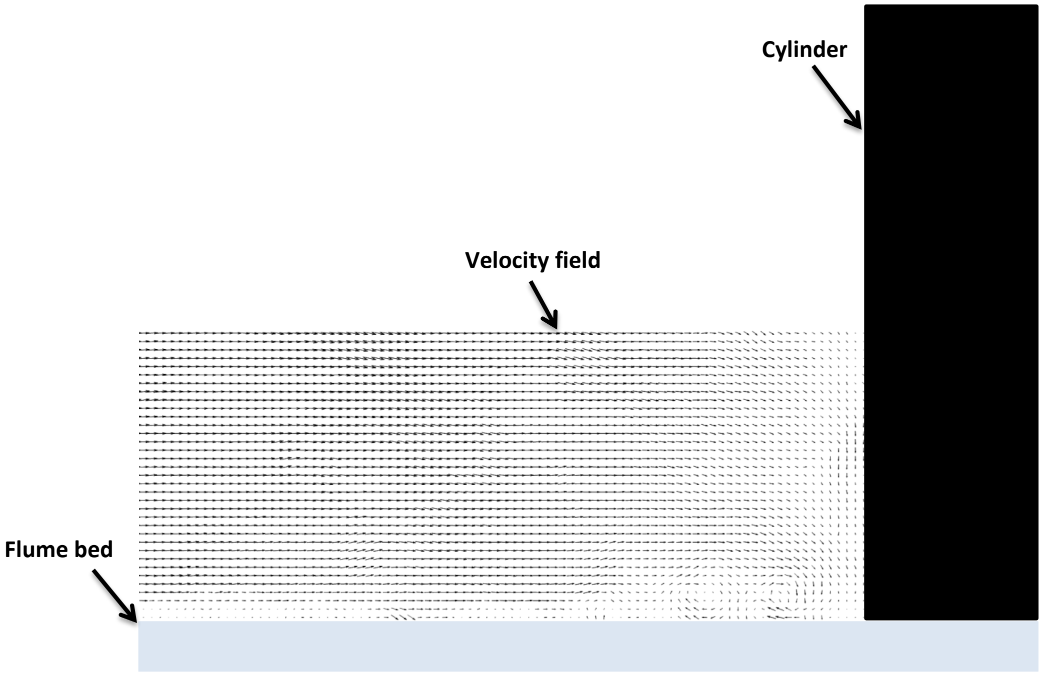

Figure 2.7: Instantaneous $u, w$ velocity field derived in the vertical plain of symmetry upstream of a cylinder for one of the experiments (Fr $= 0.2$, $D = 0.06$ $m$). This velocity field contains 4218 vectors with a spatial resolution of 1.23 $mm$ by 1.23 $mm$.

### 2.4.2 High Quality PIV Data

The signal to noise ratio of the data from the PIV measurements mainly depends on the quality of the images recorded. This is achieved, by using the following pre- and post-processing steps:

1. Physical Design of Experiments

   In order to obtain high quality imags, the camera should be focused exactly on the laser plane. This has been achieved by focusing the camera on a calibration target fixed exactly in the plane of symmetry before triggering the laser. After this, the target was removed. According to Adrian and Westerweel (2011), best results are obtained if each seeding particle, in each individual image, are distinct from the particles surrounding. In addition to the very short time of laser light (nanoseconds) and short exposure camera time (500 $\mu s$), the only light to be detected by the camera should be the laser light, as any additional light tends to reduce image sharpness and the cross-correlation between each pair of images. For this reason, and due to safety regulations, the system was encased in an enclosed box, and the top, bottom, and sides of the flume were entirely covered with wooden panels. To minimise internal light reflections, the test cylinders were painted with a matte black paint.

To ensure a homogeneous seeding density in all of the images throughout the duration of the experiment, and especially for the experiments with a very low flow velocity, a submerged pump was incorporated into the flume water tank. The water jet from this increased the turbulence inside the tank and kept the seeding particles always thoroughly mixed with the water. According to Guide (2012), each particle should occupy 2-3 pixels in diameter, and that was achieved by selecting a suitable particle size for a given distance of the camera from the laser sheet.

2. Pre-processing Procedure

   The pre-processing procedures were applied to each set of image pairs for a given experiment. The steps described in this section are numbers 1 to 3 in Fig. 2.6. The first step is to define the area of interest within the PIV images. For this, the region of the interest of the images was cropped. The cropped size was always kept as the maximum available size to cover the region of HV system activity and enough of the area upstream where no HV system existed. The third step was to remove the noise from the images by calculating the mean of each pixel through time using the full series of snapshots and then subtracting it from the series of images for each experiment. The mean subtraction was performed after transforming the image format from 8 bit integer to double format.

3. Processing the Images

   The image processing consists of undertaking the cross-correlation over the interrogation areas shown in steps 4 to 10 of Fig. 2.6. The images were uploaded to DynamicStudio v3.31 and settings were chosen following the guidelines of the manual. Two different interrogation areas of 64 × 64, and 32 × 32 pixels with 50% overlap were chosen. The size of the interrogation area was based on the displacement across the image pairs (about a quarter of the size of the interrogation area) given the time between images in a pair. The Fast Fourier Transformation (FFT) was used to perform the cross-correlations rapidly (steps 6 to 8 in Fig. 2.6). The 50% spatial overlap between the interrogation areas lessens the problem of particles moving out of the interrogation area between the two laser pulses.

According to the manual, in order to fulfil the Nyquist sampling criterion, each particle in the image should occupy between 2-3 pixels in diameter. The Nyquist sampling criterion is the maximum frequency at which we can get meaningful information from a set of data. According to this criterion, high quality data are obtained when the sampling frequency is twice that of the maximum frequency of interest in the phenomenon being measured. (Chatfield, 1996). In practice, it was found that some particles occupied 1-2 pixels and because this could violate the Nyquist criterion and produce pixel locking, a low-pass Gaussian filter was used to remove such occurrences.

For each of the flow conditions, trial-and-error precursor experiments were conducted to achieve the maximum signal to noise ratio and match the other criteria mentioned above. This was mainly done by changing the time between two pulses and then fixing it when the results were acceptable. To cover the very different flow conditions, the time between pulses of the experiments that have been conducted ranged from 100 - 12000 $\mu$ $s$, with the former for the fastest flow, and the latter for the slowest flow.

4. Post-processing Procedure

After obtaining the vector maps from the previous steps, outliers were detected spatially then removed from the images using an iterative variant of the median filter proposed by (Westerweel and Scarano, 2005), where $< 3\%$ of the vectors were removed as outliers in all of the cases. A $5 \times 5$ vector neighbourhood was used for the median calculation. The local median filter threshold was set to 5, and the normalisation level set to 0.1 pixels. Then, using *DynamicStudio* v3.31, each vector map was transformed to two orthogonal velocity fields, which were corrected for the error caused by lens distortion. This was done by creating two matrices: one with the coordinates of the centres of spots of the calibration grid before imaging; another with coordinates of the same positions recorded from an image of the calibration grid installed in the same position as the laser plane, with the camera at an identical position to the experiments. An empirical transformation was then formulated to map from one matrix into the other and a linear interpolation between two points using a build-in Matlab function "TriScattered", (Brevis and García-Villalba, 2011).

The velocity signal for each component through time at each pixel was despiked using a Matlab code based on a two step technique developed by Goring and Nikora (2002). The first step is to detect the spike of the signal by using a three-dimensional phase-space thresholding method, with the phase-space formed by the signal and its first and second derivatives. The points that are outside an ellipsoid defined by a universal thresholding criterion (Donoho and Johnstone, 1994) are considered as spikes. These are replaced by interpolation (a third order polynomial is fitted to the 12 points on each side of the spike and used to re-estimate the value at the centre of this 25 point time series). Figure 2.8 shows the despiked time series in red for the two velocity components ($u$, and $w$), with the original data shown in black, $<$ 1% of the points were considered as spikes in all of the cases.

Data analysis then consisted of two primary methods: Direct analysis of the pixel-by-pixel time series for $u$ and $w$, and transformation of the velocity fields, into a vorticity field, $\omega$, using equation 1.4, and then using a modal decomposition method to extract the dominant spatio-temporal characteristics of the horseshoe vortex (HV) system, as explained further below.

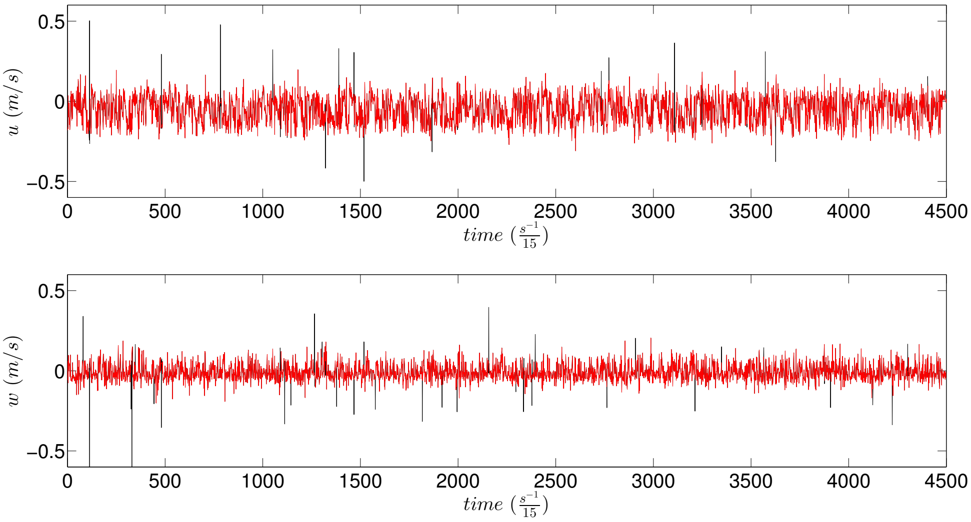

Figure 2.8: The despiking of two time series. The top plot shows the results for the longitudinal velocity component $u$, and the bottom shows the results for the vertical velocity component, $w$. The black and red colours indicate the signal before and after despiking, respectively.

## 2.5 Sampling Duration

Two methods were used to ensure that the collected data was adequate for the intended analysis. A statistical convergence was checked using a cumulative summation test for both the two velocity components and the Reynolds stress signal for the all 34 experiments. Also, the integral time scale was checked using the auto-correlation function of the two velocity components.

### 2.5.1 Convergence Based on Cumulative Summation

A technique for statistical quality control was used to analyse the time series called cumulative summation and this technique is consists of a series of statistical tests developed in 1940s for the purpose of quality control of the war materials production lines, (Bolsin and Colson, 2000). This technique was applied to test the convergence of the stream-wise velocity component, vertical velocity component, and Reynolds stress for a point under HV system for all of the 34 experiments. The results showed that 50 seconds is an acceptable time for the three quantities to converge. Figure 2.9 shows an example for experiment number 26 with Fr $= 0.2$ and $D = 0.06\ m$.

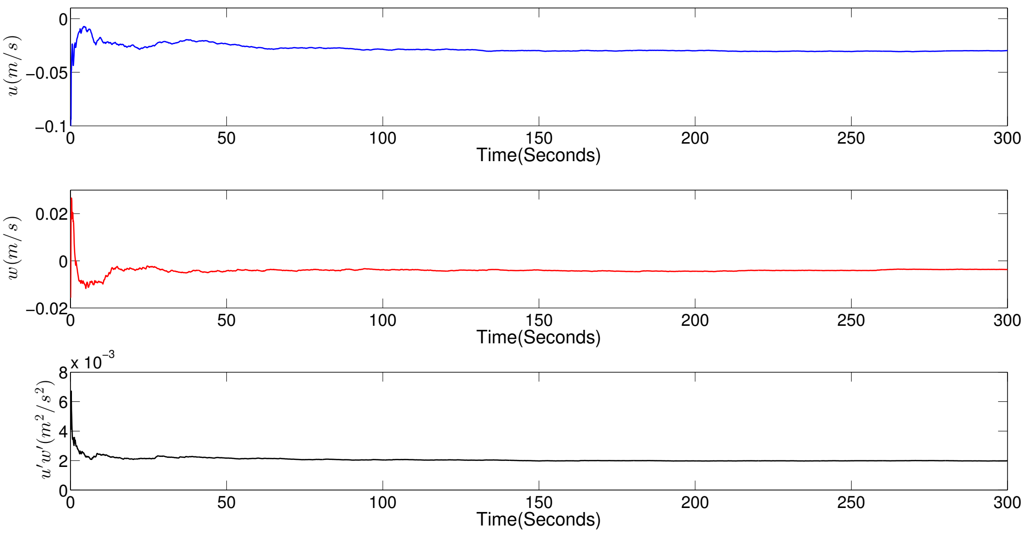

Figure 2.9: Cumulative summation of $u$, $w$, and $u'w'$ at a location of peak turbulent stresses under the HV system for experiment with Fr=0.2, and $D = 0.06\ m$.

### 2.5.2 Convergence in Terms of Integral Time Scales

The integral time scale, $T_i$, is a quantitative characterisation of the necessary time for a signal, of a measured quantity in a turbulent flow, to de-correlate (Quadrio and Luchini, 2003). In this study it is considered to be the time on the x-axis of Fig. 2.10 where each curve intersects the zero value of $R(T_i)$. The blue lines of Fig. 2.10 are the auto-correlation functions of the stream-wise velocity components of the 34 experiments. The integral time scale of each experiment was found to be between 0.2-3 seconds. It was found that the recording time provided a minimum case of 100 integral time scale in any experiment.

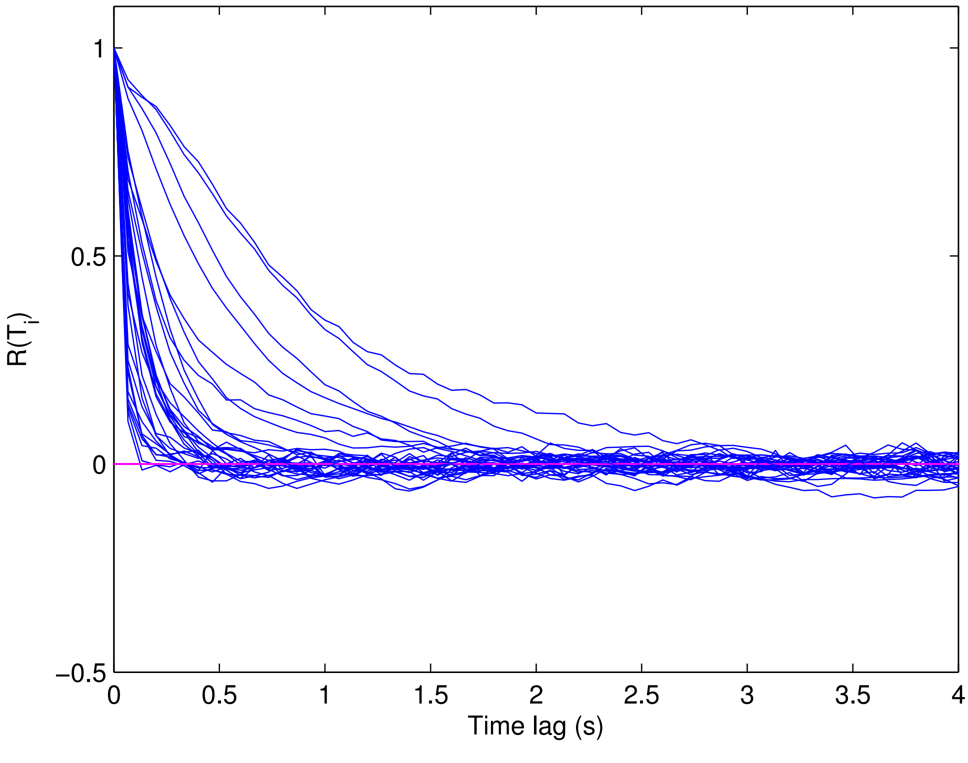

Figure 2.10: Auto-correlation for $u$ velocity component at a location of peak turbulent stresses under the HV system for experiments 1-34 conducted in this study.

## 2.6 Data Processing Methodology

### 2.6.1 Defining the Region Affected by the Horseshoe Vortex System

We employed the Proper Orthogonal Decomposition (POD) to identify the extent of the HV system. This technique is commonly used to identify coherent structures in experimental or numerical data sets (Lumley, 1967; Berkooz et al., 1993; Kurniawan and Altinakar, 2002; Cai et al., 2009; Brevis and García-Villalba, 2011) and is based on the linear decomposition of the flow signal. It extracts the best set of statistically uncorrelated modes, permitting a lower order representation of the system dynamics (Berkooz et al., 1993). The direct POD method was selected as it is used when the number of measurement fields, $T$, is greater than the number of spatial locations in each field ($X_T \times Z_T$). First, a set of vorticity fields are defined as:

$\boldsymbol{\Omega}(x, z, t)$, where $x = 1, \ldots, X_T$, $z = 1, \ldots, Z_T$, and $t = 1, \ldots, T$, and form the length $Y_T = X_T \times Z_T$ column vector, $\tilde{\Omega}(y)$ for each field, $\boldsymbol{\Omega}(x, z, t = \text{const})$. The $Y_T \times T$ matrix, $\mathbf{B}$, is then produced from the sequential compilation of all $T$ column vectors, $\tilde{\Omega}$. $\mathbf{B}$ is decomposed using a singular value decomposition (SVD):

$$\mathbf{B} \equiv \mathbf{WSV}^{\mathrm{T}} \tag{2.2}$$

and we obtain the eigenvalues, $\lambda_i$, from a renormalization of diag($\mathbf{S}$):

$$\lambda = \frac{\text{diag}(\mathbf{S})^2}{Y_T - 1} \tag{2.3}$$

where the eigenvalues are ordered such that $\lambda_1 \geq \lambda_2 \geq \ldots \geq \lambda_N$. The matrix $\mathbf{W}$ contains information on the spatial structure of each mode, which may be recovered by reshaping any of the $T$ columns in $\mathbf{W}$ back into an $X_T \times Z_T$ image. The matrix $\mathbf{V}$ contains information on the time evolution of each mode.

The decision on performing a POD decomposition of vorticity is supported by the results of Kostas et al. (2005). They found that it was more efficient to capture the fluctuation of enstrophy using a vorticity-based POD rather than working with turbulent kinetic energy variant, following a velocity-based POD. The mean vorticity field was not subtracted in **B**, thus the first mode always correspond to the mean field. This was done to measure and characterise the importance of the fluctuating field relative to the mean behaviour. In this thesis, it was found that a POD decomposition for analysing the vorticity field was a more effective means for vortex identification than adopting a criterion such as Q-criterion (Dubief and Delcayre, 2000), $\lambda_2$, (Jeong and Hussain, 1995), or swirling strenght (Chakraborty et al., 2005). Furthermore, the POD of the vorticity field is easier to relate to the physical quantities studied here using regression and clustering methods.

Figure 2.11 shows the second POD mode for the vorticity data for experiment 26 in Table 2.2 (Froude number of 0.2 and cylinder diameter of 0.06 $m$). That is, 4500 vorticity fields were derived from the PIV data and the figure corresponds to the information in the second column of **W** following a reshaping operation. The leading mode corresponded to the mean flow, meaning that the second mode contains the dominant coherent flow structure. Based on the eigenvalues, the first mode contained 32% of the total energy, while the second mode represented about 2%. For this analysis, a region extending from the cylinder to 48 $mm$ upstream was selected in all experiments to limit the area affected by the HV system. For more detailed analysis, $Ns = 40$ points were then regularly sampled from within this region at $Z = 1.23$ $mm$ from the bottom wall.

### 2.6.2 Quadrant Analysis

Quadrant analysis is used to identify the ejection-sweep cycle in turbulent boundary layers (Lu and Willmarth, 1973; Rajagopalan and Antonia, 1982; Bogard and Tiederman, 1986) based on the fluctuating values for $u$ and $w$ (Table 2.3). Because of potential confusion with sign reversals occurring as a consequence of the direction of $u$ varying locally in front of the cylinder, we define all quadrants in a consistent frame relative to the bulk velocity $U$ to ease interpretation, i.e.:

$$\begin{aligned} u' &= u - \overline{u} \quad \text{if } \overline{u} \geq 0 \\ u' &= \overline{u} - u \quad \text{if } \overline{u} < 0 \end{aligned} \tag{2.4}$$

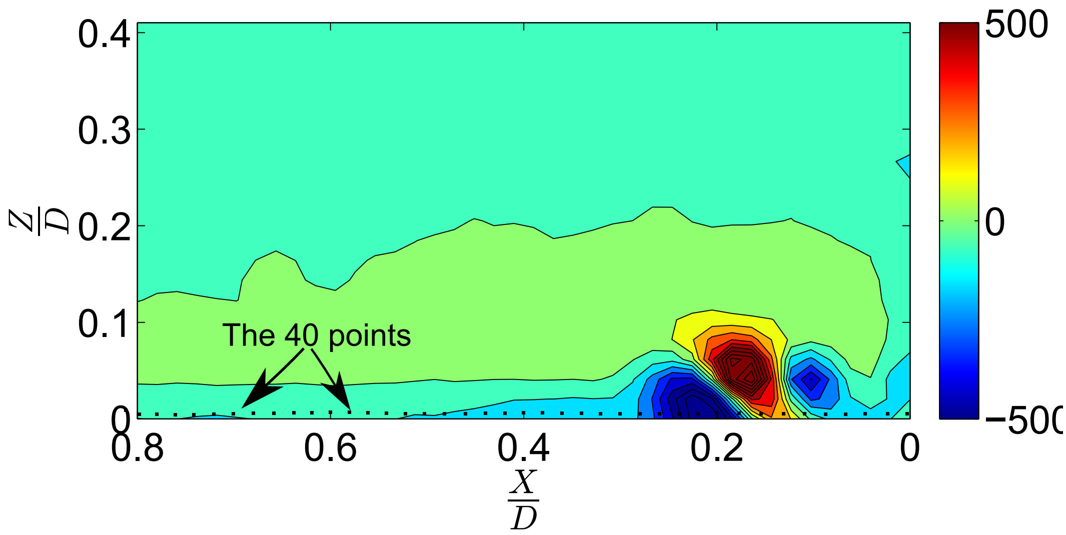

Figure 2.11: The second mode from a POD of the vorticity field $\omega$ ($s^{-1}$) showing the horseshoe vortex system upstream of the cylinder with the 40 near-bed points. The upstream edge of the cylinder is the origin for the horizontal axis used in this study. The relevant parameters for this experiment are Fr = 0.2, $D = 0.06$ $m$.

where $\overline{u}$ is the time-mean longitudinal velocity at a given position, and $u'$ is the fluctuating longitudinal velocity.

Table 2.3: Definition of quadrants used in flow event analysis

| Quadrant name | $u'$ | $w'$ |
|---|---|---|
| $Q_1$ (outward interactions) (△) | + | + |
| $Q_2$ (ejections) (◯) | - | + |
| $Q_3$ (inward interactions) (▽) | - | - |
| $Q_4$ (sweeps) (□) | + | - |

The principal Reynolds stress in a wall-bounded flow, $\tau_{Re} = -\rho\overline{u'w'}$ is decomposed, so that the instantaneous contribution $u'w'$ to the velocity covariance, $\overline{u'w'}$, and the absolute velocity covariance, $\overline{|u'w'|}$, may be evaluated per quadrant. This is necessary because, in an examination of only $\tau_{Re}$, contributions from quadrants 1 and 3 reduce the value for $\overline{u'w'}$ (Keylock, 2015), but may be important dynamically (Nakagawa and Nezu, 1977; Heathershaw and Thorne, 1985; Nelson et al., 1995). Hence, the contribution of each quadrant is studied relative to the absolute velocity covariance at the $Ns = 40$ points at $0 < X \leq 48$ $mm$, $Z = 1.23$ $mm$ $(0.018 - 0.044D)$ from the bed and relative to the 40 control points, shown in Fig. 2.11, to understand the manner in which the HV system affects the near-wall stress states. For each position, $n \in \{1, \ldots, Ns\}$, the local values for $u'$ and $w'$ are used to form a $i = 1, \ldots, T$-length data vector, $\mathrm{q}_i$, indicating quadrant membership ($q_i \in \{1, 2, 3, 4\}$). The term $\delta_i$ is introduced for the quadrant of interest, Q:

$$\begin{aligned} \delta_i &= 0\,,\ q_i \neq Q \\ \delta_i &= 1\,,\ q_i = Q \end{aligned} \tag{2.5}$$

and we then calculate

$$\alpha(Q, n) = \frac{1}{T}\sum_{i=1}^{T} |u_i' w_i'|\delta_i \tag{2.6}$$

The quadrant contribution to the velocity covariance was calculated to determine the contribution of the different quadrants in each of the 40 positions, either normalised by the summation of all quadrants and all positions ($n \in \{1, \ldots, Ns\}$),

$$\beta(Q_{1,2,3,4}) = \frac{1}{T}\sum_{n=1}^{Ns}\sum_{i=1}^{T} |u_{i,n}' w_{i,n}'| \tag{2.7}$$

or the summation of all quadrants at a specific position, $n$:

$$\gamma(Q_{1,2,3,4}, n) = \frac{1}{T}\sum_{i=1}^{T} |u_i' w_i'| \tag{2.8}$$

or the summation of quadrants 1,3, and 4 at a specific position, n:

$$\eta(Q_{1,3,4}, n) = \frac{1}{T}\sum_{i=1}^{T} |u_i' w_i'| \tag{2.9}$$

or the summation of quadrants 1,3, and 4 and all position, ($n \in \{1, \ldots, Ns\}$),

$$\zeta(Q_{1,3,4}) = \frac{1}{T}\sum_{n=1}^{Ns}\sum_{i=1}^{T} |u_{i,n}' w_{i,n}'| \tag{2.10}$$

We then studied $\gamma$, $\frac{\gamma}{U^2}$, $\frac{\gamma}{\beta}$, $\frac{\alpha}{U^2}$, $\frac{\alpha}{\beta}$, $\frac{\alpha}{\gamma}$, $\eta$, $\frac{\eta}{U^2}$, as well as $\eta$ relative to the summation of the stresses over all point, $\frac{\eta}{\zeta}$.

### 2.6.3 Stepwise Regression

We make use of stepwise regression in this study as a means to determine statistically significant relations between the observed vortex structure and the flow conditions. A generic linear model for a single response variable, $P$, and a suite of $G$ predictors, $E_1, \ldots, E_G$, may be written as:

$$P = \theta_0 + \theta_1 E_1 + \theta_2 E_2 + \ldots + \theta_G E_G \tag{2.11}$$

where the $\theta$s are the fitted coefficients. In practice, only $g \leq G$ predictors are statistically significant. Stepwise regression generates a model only containing the $g$ significant predictors. The procedure is to compare an initial model with one containing new variables and to add the variable with the greatest significance (smallest $p$-value) up to a maximum acceptable $p$-value based on a $F$-test of significance. If after the inclusion of the new term, it changes the $p$-value of any of the terms already in the model to $p > 0.1$ then the least significant term is removed from the model. This process continues until further changes do not improve the model.

### 2.6.4 *K*-Means Classification

One of the most popular data clustering algorithms is $K$-Means (Pham et al., 2005). This classification scheme is employed as a way to find natural clusters in selected frames that could represent the different forms of expression of coherent flow structure in front of the cylinder. Clusters are defined by minimising the variance within the cluster sum-of-squares differences, $C_k$. Hence, with $K$ clusters and $V$ data vectors ($K \leq V$), and a data vector, $\mathbf{u}$, indexed by $j$, one seeks to minimize

$$\mathbf{C} = \sum_{k=1}^{K} \sum_{\mathbf{u}_j \in C_i} ||\mathbf{u}_j - \mu_k||^2 \tag{2.12}$$

where $\mu_k$ is the 'true mean' for data grouping $k$. From an initial guess of the $K$-Means, $m_1^{(0)}, \ldots, m_K^{(0)}$, the standard algorithm alternates between assignment and update steps.

Thus, each datum is firstly assigned to a group, $r$:

$$C_k^{(t)} = \{u_r : ||u_r - m_j^{(t)}||^2 \leq ||u_r - m_k^{(t)}||^2 \;\; \forall \;\; 1 \leq k \leq K\} \tag{2.13}$$

Following the assignment of $u_r$ to just one group, the cluster means are updated:

$$m_k^{(t+1)} = \frac{1}{|C_k^{(t)}|} \sum_{u_j \in C_k^{(t)}} u_j \tag{2.14}$$

and the algorithm then proceeds until Eq. 2.12 is minimized.

## 2.7 Summary

This chapter has described the methodology and experimental design for the thesis. In addition, a full technical description for the apparatus used in the study (the flume, the cylinder models), as well as the PIV acquisition system and its positioning has been provided. The pre- and post-processing methods for the data have also been introduced, and results of preliminary experiments on the minimum necessary sampling length of the data have been undertaken. Finally, a description of the quadrant analysis method, Proper Orthogonal Decomposition (POD), and the statistical techniques used to analyse the data were explained. The next step is the analysis of the experimental data. These are considered in two separate chapters, reflecting the two groups of experiments proposed, above.

# Chapter 3

# Results: HV Behaviour under a Wide Range of Froude Numbers

## 3.1 Objectives and Structure of the Chapter

The main objective of this chapter is to explore the effect of Froude number and other flow and geometrical parameters on the nature of the horseshoe vortex system by analysing the experimental data collected. The primary focus is on the changes to the dynamics and geometry of the HV system and by studying the changes in the near-bed turbulent stresses and the entire region that contains the HV system. It has been chosen to focus on the near-bed stresses because a clear effect of the HV system on the near-bed stresses has been shown as a consequence of the link between vorticity and stress (Devenport and Simpson, 1990; Sumer et al., 1997; Kirkil et al., 2005*a*,*b*; Constantinescu and Koken, 2005). Studies by Baker (1979, 1980); Dargahi (1989); Lin et al. (2002); Kirkil et al. (2006); Sahin et al. (2010); Paik et al. (2010) showed that there is a spatial change in the HV system for different flow conditions, meaning that to understand near-bed stresses, it should be possible to relate the HV system to flow boundary conditions. The analyses of the turbulent stresses from specific points near the wall, both under and upstream of the HV system were divided into three sections:

In the first part of the chapter, the stresses at 40 points in near-bed locations were analysed with respect to their local peak stresses; For the second part, the stresses were disaggregated by quadrants, Bogard and Tiederman (1986), and the peak stress (which always arose in quadrant 2), from all locations, was used to normalise the turbulent stresses at all the other selected locations. In the third section, the peak value of the summation of the stresses of quadrants 1, 3, and 4 was used to represent the near-bed locations.

For each of these analyses, three different groups of experiments were considered:

- The first set of experiments is for a wide range of different flow conditions represented by 25 experiments ranging from low, sub-critical, to super-critical flow conditions (Fr=0.015-2.46) as shown in Table 2.1;
- The second and third groups covered the low Froude numbers (Fr=0.015-0.2) and upper sub-critical to super-critical Froude numbers (Fr=0.6-2.46) experiments, respectively.

By treating these cases separately, it was possible to determine if different controls were in operation for sub-critical and super-critical conditions. Multivariate statistical methods were applied to find the significant parameters that controlled the dependent variables in each group of experiments.

Experiments with Froude numbers ranging from 0.015 to 2.46 were used to explore the effect of different flow and geometrical parameters on the structure of the HV system and, thus, the impact on near-bed Reynolds stresses. The parameters that changed with the reason of choosing them are shown in Table 1.1.

The structure of this chapter consists of five main sections. The objectives and structure of the chapter are in Section 3.1. Section 3.2, explains the physical meaning of the dependent parameters used in this study. Section 3.3 deals with the Reynolds stresses at once. The following section, Section 3.4, based on partitioning the Reynolds stresses into four quadrants. Section 3.5 deals with the summation of the stresses in quadrants 1, 3, and 4. Each of the Sections 3.3, 3.4 and 3.5 has been divided into three primary subsections; The first section covers the 25 experiments ranging from low, sub-critical Froude numbers to super-critical cases. The second section is based on 11 experiments with low sub-critical

Fr, and the other one consisted of another group of eleven experiments covering the high Fr cases.

## 3.2 The Dependent Parameters Analyses and Their Physical Interpretation

The dependent parameters were chosen to isolate different aspects of the dynamics and geometry of the HV system. Parameters that represent the near-bed turbulent stresses upstream of the cylinders, where the system is active, have been formulated. These parameters were derived from the five quantities, $\alpha$, $\beta$, $\gamma$, $\eta$, and $\zeta$ which have been calculated using equations, 2.6, 2.7, 2.8, 2.9, and 2.10 respectively. The parameters were considered in three groups due to the way that the stresses were dealt with:
The first set arose when the turbulent stresses were analysed as a whole, as a function of position number, $n$. These parameters were $\gamma$, $\gamma/U^2$, and $\gamma/\beta$. In the second time, $\alpha/U^2$, $\alpha/\beta$, and $\alpha/\gamma$ were used when the stresses were partitioned into quadrants. The third part was when the turbulent stresses were analysed as the summation of quadrants 1, 3, and 4, as a function of position number, $n$, and the parameters were $\eta$, $\eta/U^2$, and $\eta/\zeta$. The peak stress locations have been measured from the front of the cylinder using two forms of distance. Initially, the dimensional distance $x_{peak}$ in $mm$ was used, but this was subsequently normalised by the cylinder diameter of each experiment to give a more general set of results.

Regarding the flow parameters: $\gamma$ is used to reflect the strength of the HV system through the mean of absolute values of the turbulent stresses at each point under and upstream of the system, $\gamma/U^2$ normalises the turbulent stress by the square of the incoming bulk flow velocity. Hence, it describes the efficiency by which mean energy is transferred into the energy of the HV system. The term $\gamma/\beta$ gives the turbulence stress in each location relative to the total turbulence of the 40 locations. In other words, it reflects the percentage of the local stress contribution to the region of the HV system, and is calculated by dividing the mean turbulent stress at each location by the summations of the mean of absolute turbulent stresses produced in the 40 locations. For the case of partitioned stresses by quadrants, $\alpha/U^2$ is for the relative contribution of the turbulent stress from each quadrant and location to the bulk momentum represented by bulk flow velocity. Similarly, $\alpha/\beta$ is the relative turbulence production at each quadrant and location compared to the mean turbulent stresses in the region of the HV system. $\alpha/\gamma$ reflects the percentage contribution of each quadrant to the mean of absolute turbulent stresses in the same location and is used to detect changes that happen in different locations away from the cylinder. Coming to the last parameters that have been used in this study, $\eta$, $\eta/U^2$, and $\eta/\zeta$ are having the same explanation of $\gamma$, $\gamma/U^2$, and $\gamma/\beta$ respectively. The only difference is that the stress contribution from quadrant 2 is not included in calculations.

## 3.3 Turbulent Stresses in front of the Cylinder

The analysis in this section deals with the turbulent stresses from specific points under and upstream of the HV system formed in front of a circular cylinder. The turbulent stresses (expresses as velocity covariances) at each of the 40 near-wall locations ($Ns$=40) are shown in Figures 3.1, 3.2 and 3.3, where the abscissa is the distance from the upstream edge of the cylinder. These figures may be used to explore the behaviour of the HV system through studying the magnitude and location of the peak value among the group of points for the three quantities, $\gamma$, $\gamma/U^2$, and $\gamma/\beta$ respectively. The mean of the absolute turbulent stresses at a single point has been chosen as a criterion for the HV system and the point that has the maximum mean turbulent stress value among the group of 40 near-bed points was selected as that identifying the maximal stress contribution near the wall from the HV system. It is noted from Figure 3.1, that $\gamma$ values are small in experiments 1-15 relative to the two bottom rows (experiments 16-25). The significantly large values of $\gamma$ occur in experiments 24 and 25 of Table 2.1, and arise for Fr=1.934 and Fr=2.46, with $D = 0.04\ m$. This initial result is suggestive of the potential importance of both $\mathrm{Re}_D$ and Froude number for the flow dynamics. The $\gamma$ values are small in the first experimental results due to the low flow velocities, $\mathrm{Re}_D$, or Fr. The $\gamma$ values of experiments 6 to 8 shown in Table 3.1 related to the same experiments of Table 2.1 with constant Fr and increased $D$, show very clearly that $\gamma$ increases with $D$ and that the peak value is driven away from the cylinder as $D$ increases. While, for experiments 9, 10, and 11, $\gamma$ values have increased then decreased and the peak getting closer to the cylinder with decreasing $D$, although Fr is increasing. This is showing that the effect of $D$ dominates Fr. The difference in $\gamma$ values is quite obvious among the plots of Fig. 3.1, ranging from less than $0.06 \times 10^{-4} m^2/s^2$ to about $200 \times 10^{-4} m^2/s^2$ over experiments 1 to 25, respectively. The trend for the different values no longer exists when $\gamma$ values are normalised by the square of approaching bulk flow velocity $U^2$ as shown in Fig. 3.2, and this is due to the increased values of $U$ as the Fr increased. It is also noticed from Fig. 3.3 that the difference is at its minimal values when $\gamma$ is normalised by the summation of the absolute mean stresses of the 40 points, $\beta$, in other words it is the relative contribution of $\overline{|u'w'|}$ from 4500 values collected over 300 seconds at a single point to the summation of mean of the absolute stresses in the forty sites $\gamma/\beta$ and that is emphasising the role of relative $\gamma/\beta$ in each of the experiments. In the former case the difference between the different cases is reduced due to the direct correlation between the value of $\gamma$ and the $U$ as a direct measure for turbulence in each experiment. While in the latter the value of $\gamma$ at the peak point is very related to the other $\gamma$ values in the surrounding near-bed points. Coming back to Fig. 3.2, it can be seen that for low sub-critical flows, where $U$ is held constant, the values of $\gamma/U^2$ increase with increasing $D$. For example, this is clearly the case for experiments 6, 7 and 8. However, in the case of critical flow conditions (experiments 19, 20, and 21), there is no significant change in the value of $\gamma/U^2$ when $D$ is increased. This could be one of the characteristics of the HV system in critical flow conditions. For the first five experiments (Fr=0.015-0.05) the mean absolute values of the near-bed stresses are plotting a flat line at the lowest Fr then as the Fr increases, the curvature increases with a peak roughly in the half way from the cylinder to the point where a significant rise in the curve happens. When it comes to Fig. 3.3, then the differences between the different flow conditions is reduced in magnitude. However, the location of the peaks remains in the same position, regardless of the normalisation type adopted. The points underneath the HV system in one experiment are having very similar basic geometry in most of the experiments.

There is a small increase observed in the values for $\gamma$, $\gamma/U^2$, and $\gamma/\beta$ in Figures 3.1, 3.2 and 3.3, respectively, as one approaches the HV region. This suggests that the effect of the HV system is experienced further upstream than the region delimited in this study to some degree. However, the increase in these values is very small for the majority of

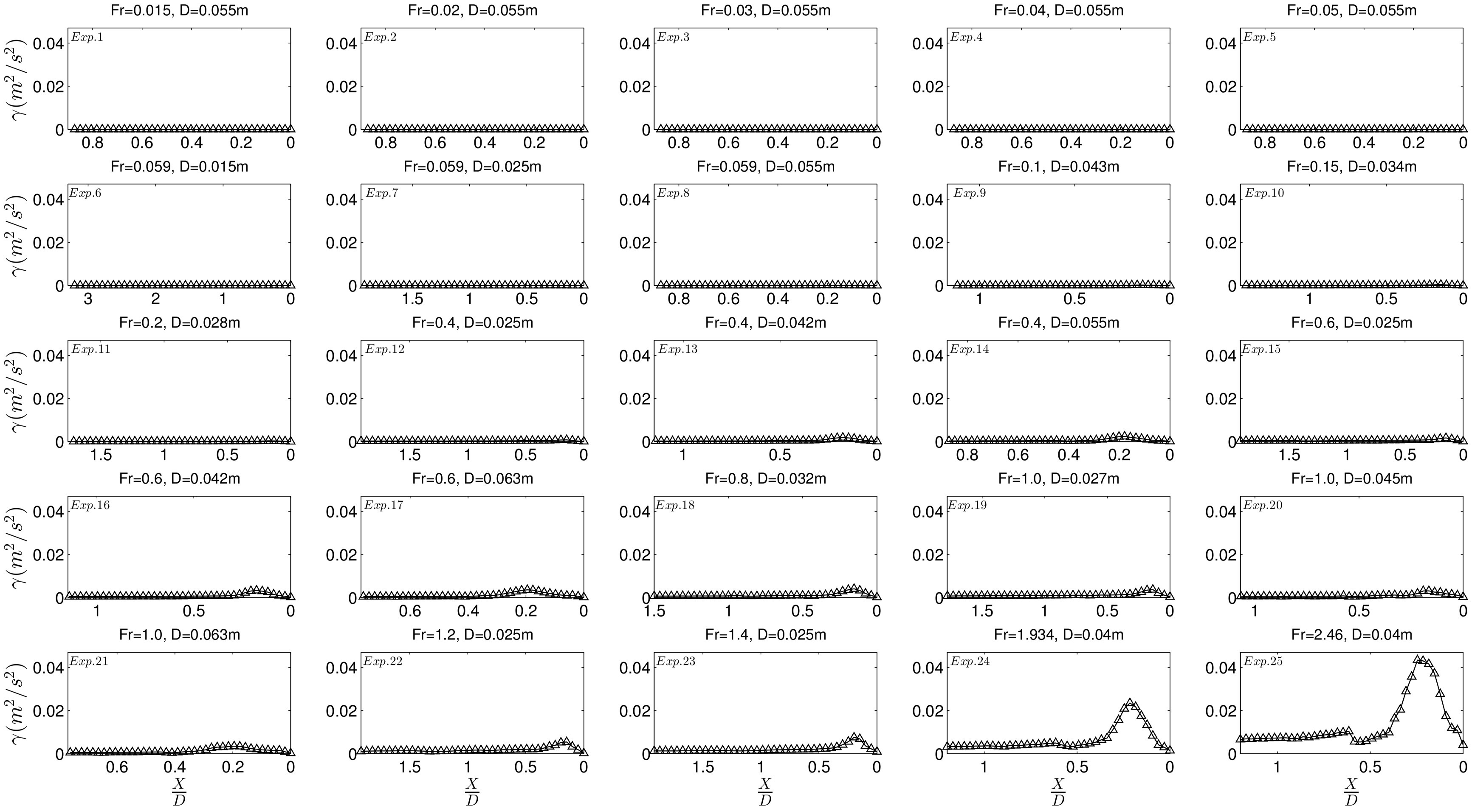

Figure 3.1: Mean of absolute velocity covariances $\gamma$. The abscissa indicates distance upstream from the upstream edge of the cylinder. Fr=0.015-2.46.

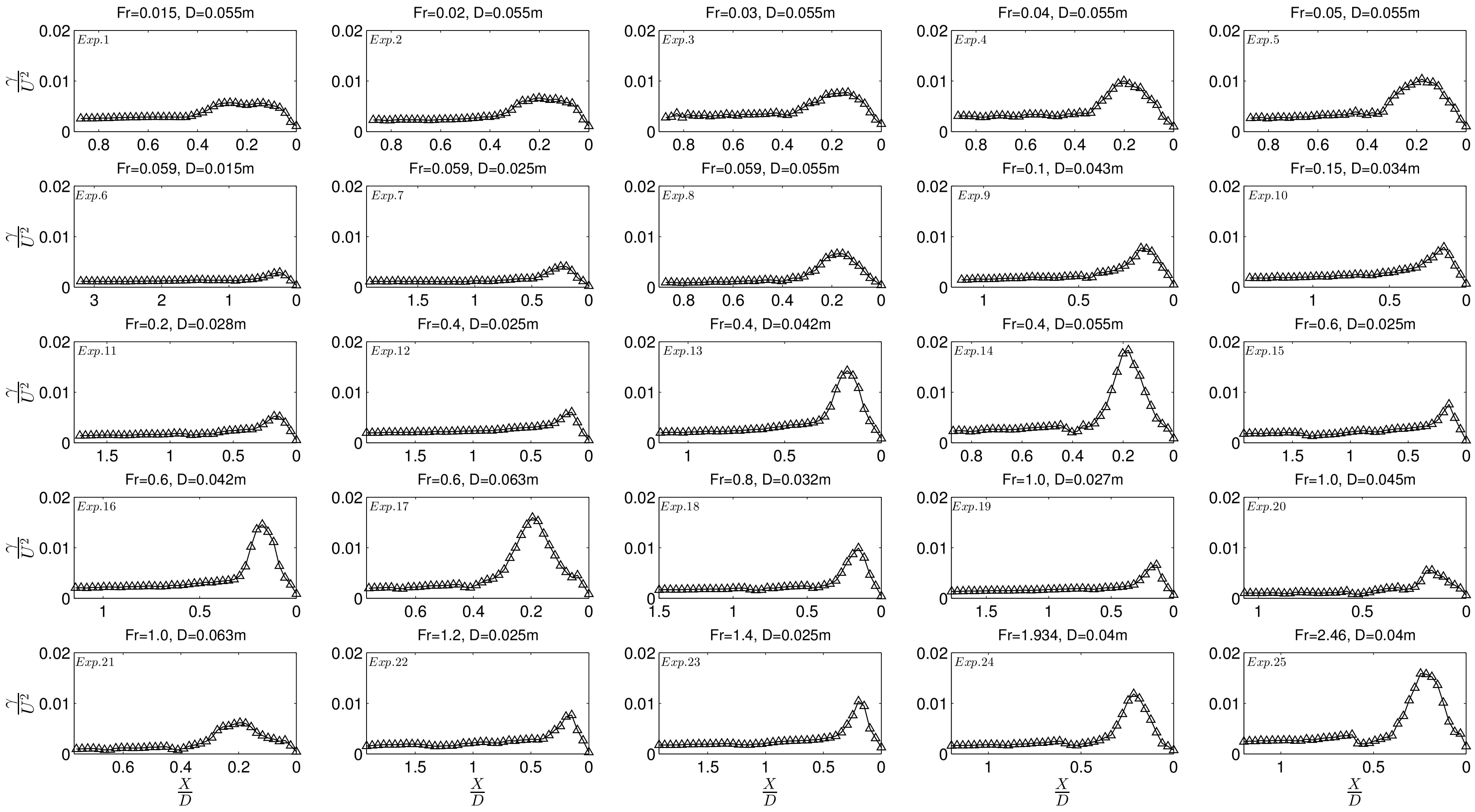

Figure 3.2: Mean of absolute velocity covariances normalized by the square of the approaching bulk flow velocity $\frac{\gamma}{U^2}$. The abscissa indicates distance upstream from the upstream edge of the cylinder. Fr=0.015-2.46.

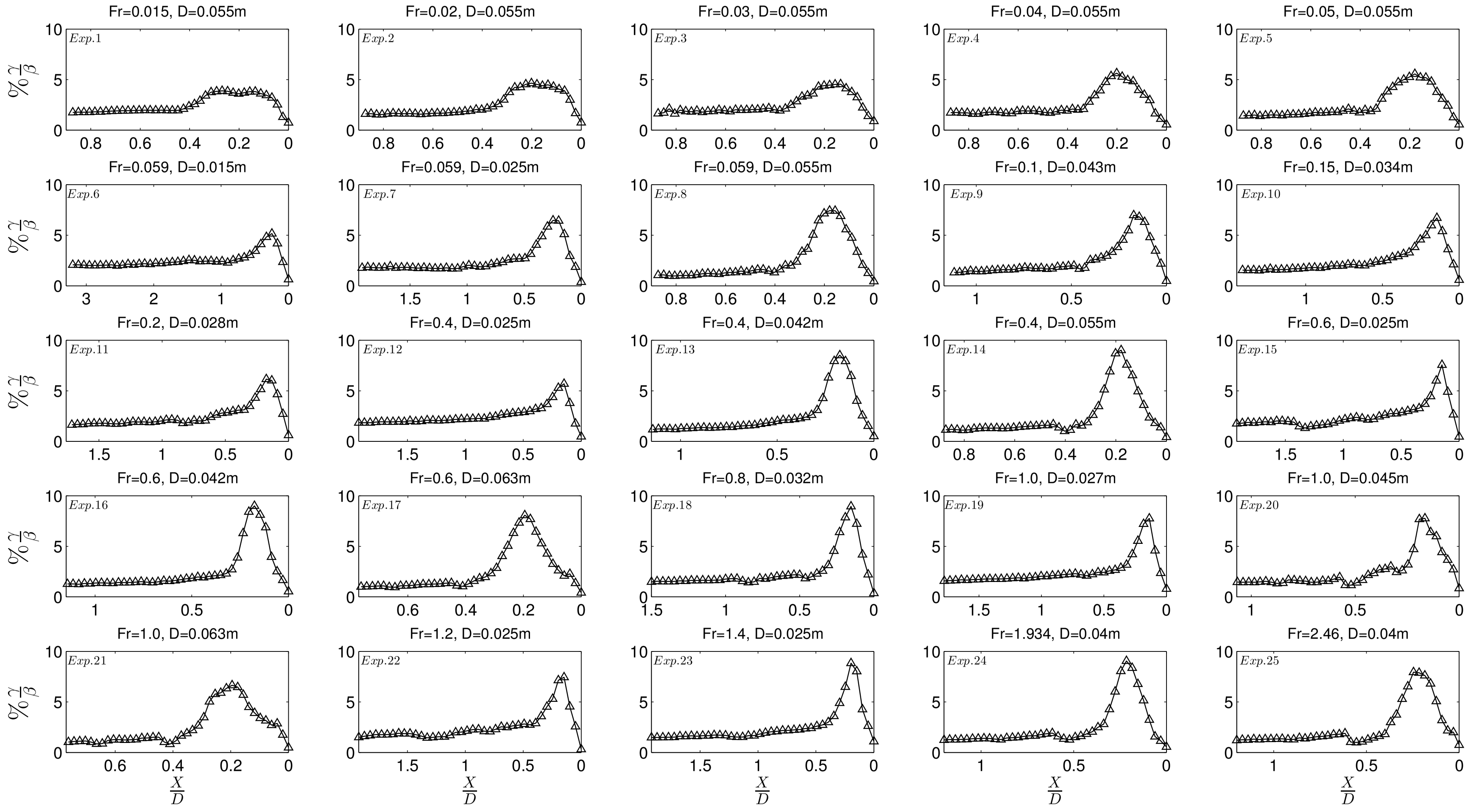

Figure 3.3: Mean of absolute velocity covariances normalized by the summation of the means of absolute velocity covariances over all forty positions $\frac{\gamma}{\beta}$. The abscissa indicates distance upstream from the upstream edge of the cylinder. Fr=0.015-2.46.

the 20 locations furthest from the cylinder, and this is particularly true for the first five experiments. Figures 3.2 and 3.3 show that the mean of these values is approximately 2-7 times lower than the peaks experienced in the HV region, highlighting the significance of the vortex system for near-wall stress generation (Devenport and Simpson, 1990; Sumer et al., 1997). The values in Table 3.1 were then used in the stepwise regression analysis to determine the controls on the HV system dynamics. The location of the peak values for $\gamma$, $\gamma/U^2$, and $\gamma/\beta$ is always the same. The three following subsections will consider the three groups of experiments mentioned above.

Two types of statistical analysis have been undertaken: a multivariate regression to determine which of the flow variables is controlling particular aspects of the HV system by separating the most significant flow parameters shown in Table 2.1 that affect the HV system from others through their control on the dependent variables of Table 3.1; and, a $K$-Means clustering of the individual frames of vorticity and comparison between these groups and the variables altered in particular experiments.

### 3.3.1 Sub-critical to Super-critical Froude Numbers (**Fr** $\in \{0.015 - 2.46\}$)

This section of the analyses includes data from 25 experiments that cover a wide range of Froude numbers. The results represent the very different conditions that affect the production of turbulent stresses by the HV system and that give an overview of the parameters that are most effective for controlling the stresses.

#### 3.3.1.1 Stepwise regression analysis of the turbulent stresses

The results of the stepwise regression analyses based on the data of Tables 2.1 and 3.1 are stated in Table 3.2, which shows that the only parameter which played a role in the prediction of the maximum stress location is $D$ when the distance is measured in $mm$ and $h$ and $\mathrm{Re}_D$ when the distance is normalised by $D$. In contrast, the peak values of the mean absolute stresses were controlled by Fr and $h$ for $\gamma$, $D$ and $h$ for $\gamma/U^2$, and $h$ and $\mathrm{Re}_h$ for $\gamma/\beta$. Hence, there would appear to be significant controls from both dimensional and dimensionless quantities. The bulk flow velocity, flow depth, and cylinder diameter appear to act separately or in combination through the Froude number, obstacle Reynolds number, or flow depth Reynolds number. The $R^2$ and $p$-values showed a significant effect of Fr in controlling the peak value of $\gamma$. It is noticed that the effect of Fr is removed when normalising by $U^2$ and $\beta$, where it is replaced with $D$ in the former and with $\mathrm{Re}_h$ in the latter. The plots in Fig. 3.4 show a significant effect of $D$ and Fr on the location and the magnitude of the peak stress, in which both of them are responding positively to the controlling parameters. This will be explored more in the next two sections to find out if it applies on the whole group of experiments or it applies more on one group of the experiments more than the other.

As explained in Chapter 2, the second mode from the POD analysis isolates the HV system. As it is apparent from Figure 3.5, the geometry of the HV system is more clearly distinguished as Fr and $D$ increase from very low values. For example, the system with a set of three well-defined vortices, with the central one rotating in an opposite sense to its neighbours emerges at $\mathrm{Fr} = 0.4$ for the $D = 0.055\ m$ cylinder, but it is not discerned at $\mathrm{Fr} = 1.0$ for the $D = 0.027\ m$ cylinder, and that is also clear from Table 3.3 when the mean enstrophy for the former case is 35282 $s^{-2}$ and for the latter is 26714 $s^{-2}$. Enstrophy ($\varepsilon$) is an important concept for turbulence in fluid dynamics, and it is used as a measure for the kinetic energy. The enstrophy can be described as the integral of the square of the vorticity ($\omega$):

$$\varepsilon(\omega) \equiv \frac{1}{2} \int_S \omega^2 \, dS \tag{3.1}$$

#### 3.3.1.2 The controlling parameter during instances when high turbulent stresses are exerted

The stepwise regression results showed an effect of different parameters including Fr. However, the HV system dependency was further explored depending on the moments of high stresses both in a single point under the HV system and from the maximum stresses within the whole field of flow. The first approach considered the maximum mean absolute stresses observed at a single point and its position for $\gamma/\beta$ as a criterion for this exploration.

Table 3.1: Dependent variables used in the stepwise regression for the turbulent stresses for experiments of Fr=0.015-2.46. The predictor variables are given in Table 2.1.

| Exp. No. | $x_{max}$ for $\gamma$, $\gamma/U^2$, and $(\gamma/\beta)$ $(mm)$ | $x_{max}/D$ for $\gamma$, $\gamma/U^2$, and $\gamma/\beta$ | $\gamma_{max}$ $(\times 10^{-4} m^2 s^{-2})$ | $(\gamma/U^2)_{max}$ | $(\gamma/\beta)_{max}$, (%) |
|---|---|---|---|---|---|
| 1 | 14.77 | 0.269 | 0.025 | 25.62 | 3.89 |
| 2 | 11.08 | 0.201 | 0.043 | 29.85 | 4.65 |
| 3 | 7.39 | 0.134 | 0.087 | 34.66 | 4.55 |
| 4 | 11.08 | 0.201 | 0.162 | 45.06 | 5.63 |
| 5 | 9.85 | 0.179 | 0.228 | 46.58 | 5.56 |
| 6 | 3.69 | 0.246 | 0.221 | 13.07 | 5.16 |
| 7 | 6.15 | 0.246 | 0.310 | 18.32 | 6.46 |
| 8 | 9.85 | 0.179 | 0.502 | 29.69 | 7.43 |
| 9 | 7.39 | 0.172 | 0.960 | 34.82 | 6.97 |
| 10 | 4.92 | 0.145 | 1.568 | 35.55 | 6.71 |
| 11 | 4.92 | 0.176 | 1.538 | 30.38 | 6.16 |
| 12 | 3.69 | 0.148 | 3.55 | 27.23 | 5.69 |
| 13 | 7.39 | 0.176 | 8.36 | 64.13 | 8.51 |
| 14 | 9.45 | 0.179 | 10.74 | 82.40 | 9.02 |
| 15 | 3.69 | 0.148 | 7.73 | 34.14 | 7.56 |
| 16 | 7.39 | 0.176 | 14.86 | 65.59 | 9.00 |
| 17 | 12.31 | 0.195 | 16.29 | 71.87 | 8.08 |
| 18 | 4.92 | 0.154 | 18.34 | 44.70 | 8.95 |
| 19 | 4.92 | 0.182 | 15.51 | 27.57 | 7.21 |
| 20 | 7.39 | 0.164 | 13.95 | 24.79 | 7.76 |
| 21 | 12.31 | 0.195 | 15.61 | 27.75 | 6.65 |
| 22 | 3.69 | 0.148 | 24.36 | 34.52 | 7.44 |
| 23 | 4.92 | 0.197 | 34.06 | 46.82 | 8.83 |
| 24 | 8.62 | 0.215 | 105.62 | 53.35 | 9.05 |
| 25 | 9.85 | 0.246 | 195.03 | 71.46 | 7.94 |

Table 3.2: The predictor variables contributing significantly to a stepwise regression equation for the selected response variables, together with their significance levels and the $R^2$ associated with the regression equation for turbulent stresses for experiments of Fr=0.015-2.46.

| Regression | $R^2$ | Pred. 1 | $p$-value | Pred. 2 | $p$-value |
|---|---|---|---|---|---|
| $x_{max}(\gamma, \gamma/U^2, \gamma/\beta)$ $(mm)$ | 0.833 | $D$ | $< 0.001$ | - | - |
| $x_{max}(\gamma, \gamma/U^2, \gamma/\beta)$ $(\frac{x_{max}}{D})$ | 0.678 | $h$ | $< 0.001$ | $\mathrm{Re}_D$ | $< 0.001$ |
| $\gamma_{max}$ | 0.846 | Fr | $< 0.001$ | $h$ | 0.0091 |
| $(\gamma/U^2)_{max}$ | 0.617 | $D$ | 0.0128 | $h$ | 0.0144 |
| $(\gamma/\beta)_{max}$ | 0.725 | $h$ | $< 0.001$ | $\mathrm{Re}_h$ | 0.0028 |

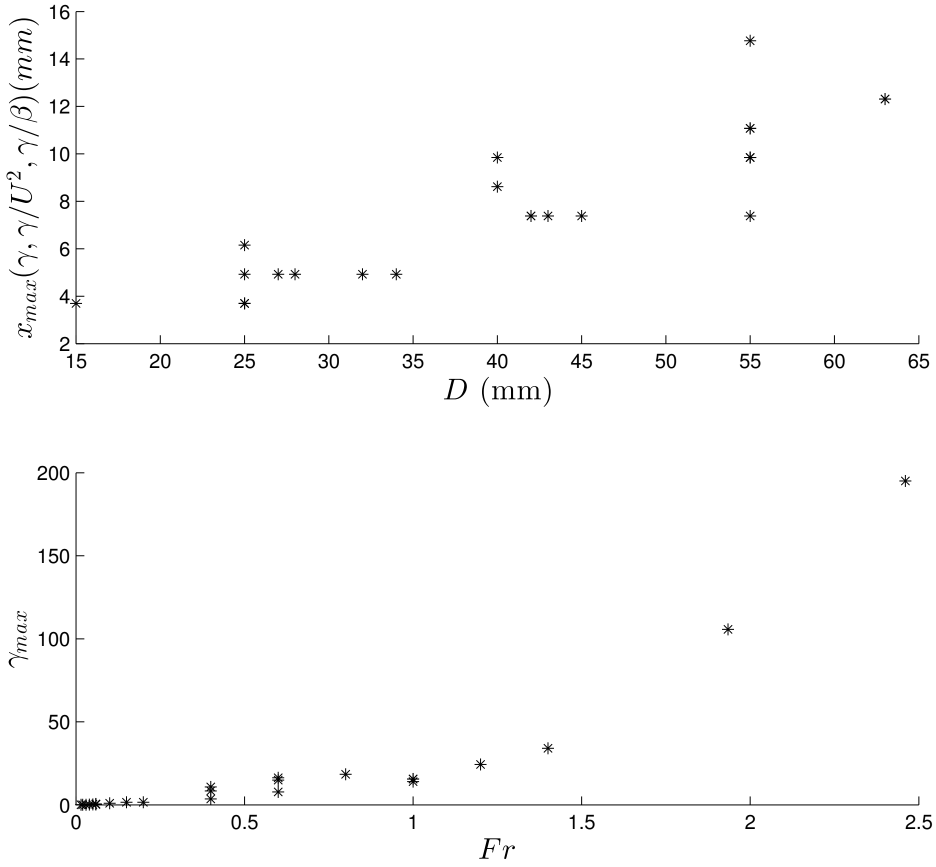

Figure 3.4: The relationship between the location and magnitude of the peak stresses with the cylinder diameter and Froude number in the top and bottom plots, respectively.

The hypothesis is that these high stresses represent the most effective instances that plays a major role shaping the HV system. The high stress state frames, which must dominate the values for $|u'w'|$ were separated using the following methodology:

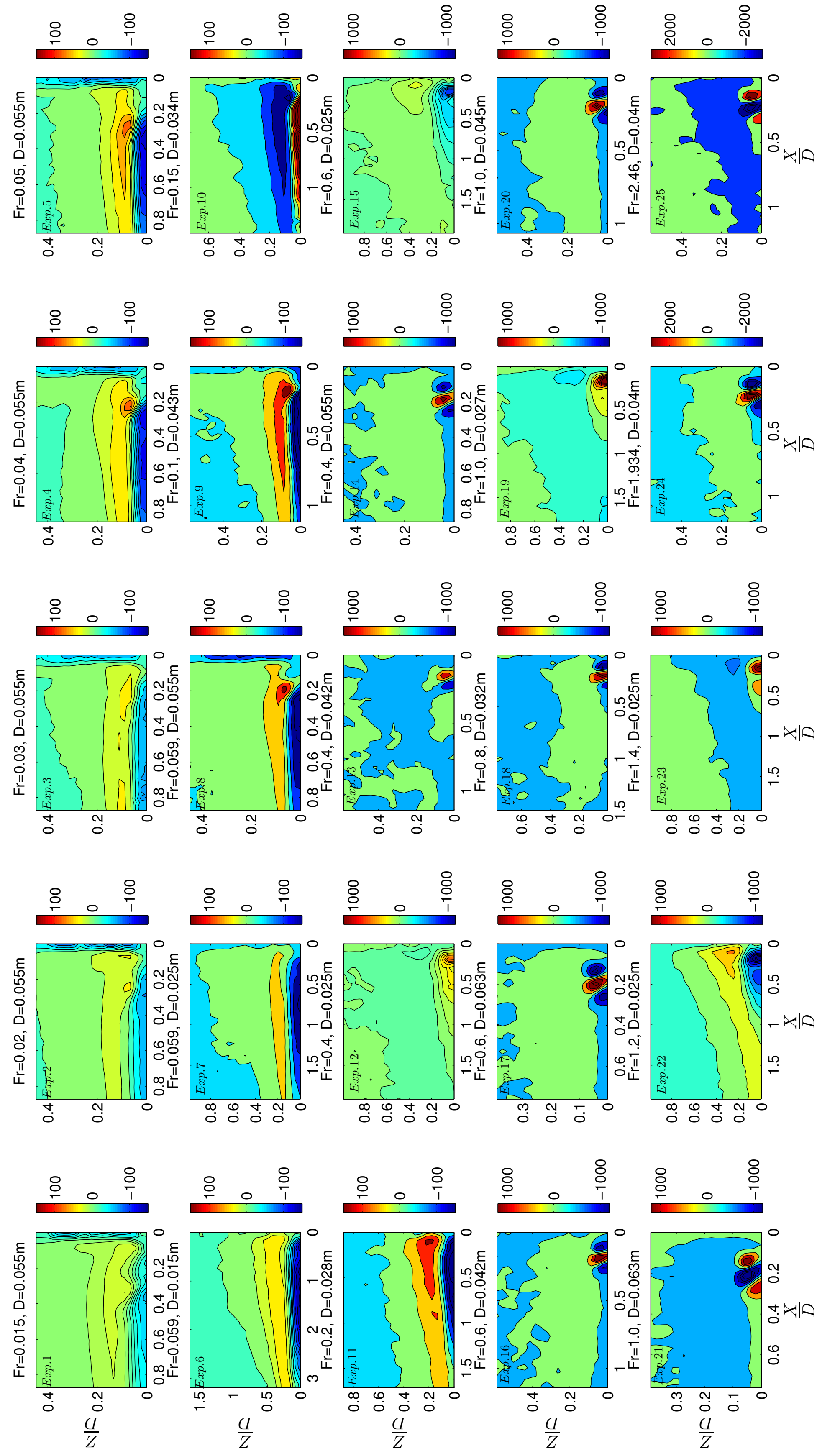

Figure 3.5: Mode 2 from the POD of the vorticity field (units of $s^{-1}$), showing the HV system for experiments 1 to 25 of Table 2.1.

Table 3.3: The parameters used to characterise POD mode 2 of the vorticity field for experiments of Fr=0.015-2.46.

| Exp. No. | Fr | $D$ | Mean Enstrophy $s^{-2}$ |
|---|---|---|---|
| 1 | 0.015 | 0.055 | 342 |
| 2 | 0.02 | 0.055 | 567 |
| 3 | 0.03 | 0.055 | 678 |
| 4 | 0.04 | 0.055 | 1493 |
| 5 | 0.05 | 0.055 | 1591 |
| 6 | 0.059 | 0.015 | 1514 |
| 7 | 0.059 | 0.025 | 1637 |
| 8 | 0.059 | 0.055 | 2935 |
| 9 | 0.10 | 0.043 | 4053 |
| 10 | 0.15 | 0.034 | 4951 |
| 11 | 0.20 | 0.028 | 3805 |
| 12 | 0.40 | 0.025 | 7558 |
| 13 | 0.40 | 0.042 | 15763 |
| 14 | 0.40 | 0.055 | 35282 |
| 15 | 0.60 | 0.025 | 12151 |
| 16 | 0.60 | 0.042 | 37224 |
| 17 | 0.60 | 0.063 | 66917 |
| 18 | 0.80 | 0.032 | 34660 |
| 19 | 1.00 | 0.027 | 26714 |
| 20 | 1.00 | 0.045 | 48957 |
| 21 | 1.00 | 0.063 | 94215 |
| 22 | 1.20 | 0.025 | 51315 |
| 23 | 1.40 | 0.025 | 52196 |
| 24 | 1.934 | 0.04 | 309440 |
| 25 | 2.46 | 0.04 | 583770 |

- A hole size, $H$ was introduced based on the time series statistics at the identified point that had the dominant contribution to $\gamma/\beta$ Bogard and Tiederman (1986); Keylock (2007);

- Large stress states at this location were then isolated using a selected hole size of $H > 2$. This value for $H$ was chosen based on the results of Sarkar and Dey (2010) who found that the extreme Reynolds shear stress contributions were identified with $H = 2$;

- Hence, for this identified position, the velocity time series was extracted, the standard deviations of the velocity components, $\sigma(\ldots)$ were calculated and a high stress state was defined as:

$$|u'w'|_Q = 1,2,3,4 > H\sigma(u)\sigma(w) \tag{3.2}$$

For each experiment, the number of points ($\phi$) for which $H > 2$ and their positions in time were identified. The frames corresponding to these times were extracted and the percentage of the total number of frames selected ranged from 4.98 to 6.82% over the twenty five experiments. The summation of the stress magnitudes at the peak stress locations for these frames contributed from 24.68 to 34.37% of the $\sum |u'w'|$ over all frames of each of the experiments.

The vorticity fields for these frames were then automatically classified into three groups ($k_1$, $k_2$, and $k_3$) using the $K$-Means classifier and the number of frames in each cluster ($C_{k_1}$, $C_{k_2}$ and $C_{k_3}$) was extracted. These results are shown in the second to fourth columns of Table 3.4 under the 'Single Point' identifier. It is clear from the results that experiments 1-11 may be grouped together with a clear first cluster dominance, experiments 12-23 form the second cluster and experiments 24 and 25, from the third cluster. Table 2.1 shows that the first group of experiments (1-11) have the lowest Fr ranging from 0.015 to 0.2, experiments 12-23 having Fr of 0.4 to 1.4, and experiments 24 and 25 having the highest Fr of 1.934 and 2.46 respectively.

To ensure the results were consistent, in addition to the clustering of the vorticity fields based on the single point hole size exceedance results, a whole frame approach was employed. All the pixels in a frame were extracted and the stress magnitudes $|u'w'|$ were normalised by the product of the global standard deviations for $u$ and $w$ for all $x$, $y$, $t$. Frames were then placed in descending rank order based on the frame median value for the normalised stress magnitudes. Then for each experiment the first $C_{k_1} + C_{k_2} + C_{k_3}$ frames were extracted so that the total number of frames analysed for each experiment using the single point and whole frame approaches was identical. Again three groups were selected for the $K$-Means classification and the number of frames corresponding to each cluster over the twenty five experiments is shown in columns 5 to 7 of Table 3.4 under the 'Whole Frame' heading. Results are very similar to the single point case, with experiments 1-11 belonging to one group, followed by experiments 12-23, and experiments 24-25 to the other two groups respectively. Hence, the differences between the single point and whole frame approaches are minor. Thus, the Froude number not only affects the near-bed stresses exerted by the HV system, but also the stresses produced by the whole HV system.

Table 3.4: The number of frames from each experiment allocated to the three clusters found from the $K$-Means analysis ($C_{k_1}$, $C_{k_2}$ and $C_{k_3}$). The three groups of results represent frames chosen using a single point near the bed on the one hand, and using the whole frame points on the other hand for the case of turbulent stresses for experiments of Fr=0.015-2.46.

| | Single Point | | | Whole Frame | | |
|---|---|---|---|---|---|---|
| Experiment | $C_{k_1}$ | $C_{k_2}$ | $C_{k_3}$ | $C_{k_1}$ | $C_{k_2}$ | $C_{k_3}$ |
| 1 | 288 | 0 | 0 | 288 | 0 | 0 |
| 2 | 287 | 0 | 0 | 287 | 0 | 0 |
| 3 | 224 | 0 | 0 | 224 | 0 | 0 |
| 4 | 241 | 0 | 0 | 241 | 0 | 0 |
| 5 | 229 | 0 | 0 | 229 | 0 | 0 |
| 6 | 307 | 0 | 0 | 307 | 0 | 0 |
| 7 | 282 | 0 | 0 | 282 | 0 | 0 |
| 8 | 281 | 0 | 0 | 281 | 0 | 0 |
| 9 | 249 | 0 | 0 | 249 | 0 | 0 |
| 10 | 238 | 2 | 0 | 236 | 4 | 0 |
| 11 | 231 | 2 | 0 | 233 | 0 | 0 |
| 12 | 16 | 248 | 0 | 20 | 244 | 0 |
| 13 | 1 | 244 | 0 | 6 | 239 | 0 |
| 14 | 17 | 257 | 0 | 27 | 247 | 0 |
| 15 | 0 | 248 | 0 | 0 | 248 | 0 |
| 16 | 0 | 240 | 0 | 0 | 240 | 0 |
| 17 | 0 | 271 | 0 | 0 | 271 | 0 |
| 18 | 1 | 258 | 0 | 0 | 259 | 0 |
| 19 | 0 | 264 | 0 | 0 | 264 | 0 |
| 20 | 0 | 247 | 0 | 0 | 247 | 0 |
| 21 | 0 | 280 | 0 | 0 | 280 | 0 |
| 22 | 0 | 254 | 0 | 0 | 254 | 0 |
| 23 | 0 | 234 | 0 | 0 | 232 | 0 |
| 24 | 0 | 41 | 231 | 0 | 28 | 244 |
| 25 | 0 | 0 | 301 | 0 | 0 | 301 |

The plots shown in Figure 3.6, show from top to bottom the centroid frames for clusters $K_1$, $K_2$ and $K_3$, respectively. The results from the single point analysis are shown in the left-hand panel, while those from the whole frame analysis appear on the right. The HV system is defined more clearly in terms of both vorticity magnitude and vortex size for all three clusters for the single point analysis. Hence,

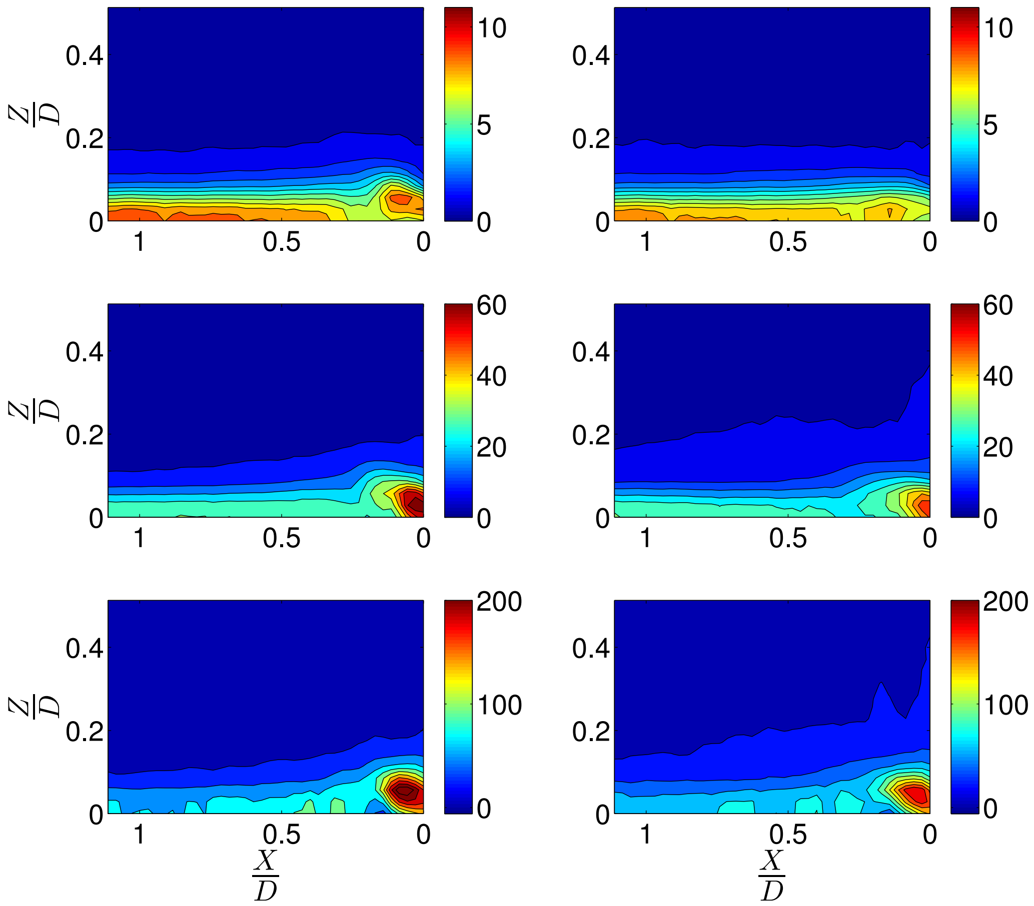

Figure 3.6: The centroids of the clusters extracted from the vorticity fields $\omega$ $(s^{-1})$ over the twenty five experiments for turbulent stresses from experiments of Fr=0.015-2.46. Results on the left are for the single point analysis while those on the right are for the whole frame method. Centroid of cluster 1 is shown at the top and of cluster 3 at the bottom in each case. The origin for the horizontal axis is the upstream edge of the cylinder.

the near-bed stresses are able to capture the most energetic vorticity fields better than the stresses in the whole field. It is also clear that as the momentum flux increases, the vorticity increases. Hence, the points near the wall are more relevant for extracting a coherent HV structure than consideration of the whole frame.

### 3.3.2 Lower Sub-critical Froude Numbers (Fr $\in \{0.015-0.2\}$)

This part of the study is to find out if the flow conditions for low Froude numbers have a different control on the dynamics of the HV system upstream of the circular cylinder when analysed separately from the whole group of experiments studied in Section 3.3.1. Experiments 1-11 shown in Table 2.1 are used in this part of the study and cover a range of very low Froude numbers, up to Fr=0.2.

#### 3.3.2.1 Stepwise regression analysis of the turbulent stresses

The stepwise regression analyses results are stated in Table 3.5 which shows that $D$ is the parameter which played the most significant role in the prediction of the maximum stress location when the distance is measured in $mm$ and $h$ as the distance is normalised by $D$, while the peak values were controlled by Fr for $\gamma$, $h$ and $D$ for $\gamma/U^2$, and $\mathrm{Re}_D$ and $\mathrm{Re}_h$ for $\gamma/\beta$. Further inspection of Table 3.5 shows that the control variables are less effective at explaining the location of the peak stresses than the peak magnitudes ($R^2 = 0.761$, and 0.652 rather than $R^2 = 0.937$, 0.903, and 0.872), where $R^2$ is the coefficient of determination. This contrast is greater than what seen in Table 3.2 where the $R^2$ values are similar for location and magnitude analyses.

This analysis of the low Froude numbers case also highlights similar primary control parameters on the HV system to that found for all of the experiments, apart from $(\gamma/\beta)_{max}$, where $\mathrm{Re}_D$ is controlling the system for a low Froude number instead of $h$. This result has interesting implications: dimensional results for the location of peak stresses are controlled by $D$ and normalisation by $D$ leads to a height control, implying that momentum flux into the HV region is crucial for the spatial extent of the system when one normalises by diameter. Conversely, the peaks value for $\gamma$, whether dimensional or normalised by incoming magnitude, is controlled by $h$ for

Table 3.5: The predictor variables contributing significantly to a stepwise regression equation for the selected response variables, together with their significance levels and the $R^2$ associated with the regression equation for the turbulent stresses from experiments of Fr=0.015-0.2.

| Regression | $R^2$ | Pred. 1 | $p$-value | Pred. 2 | $p$-value |
|---|---|---|---|---|---|
| $x_{max}(\gamma, \gamma/U^2, \gamma/\beta)$ $(mm)$ | 0.761 | $D$ | 0.0016 | - | - |
| $x_{max}(\gamma, \gamma/U^2, \gamma/\beta)$ $(\frac{x_{max}}{D})$ | 0.652 | $h$ | 0.0206 | - | - |
| $\gamma_{max}$ | 0.937 | Fr | $< 0.001$ | - | - |
| $(\gamma/U^2)_{max}$ | 0.903 | $h$ | $< 0.001$ | $D$ | 0.0016 |
| $(\gamma/\beta)_{max}$ | 0.872 | $\mathrm{Re}_D$ | 0.0018 | $\mathrm{Re}_h$ | 0.308 |

Fr, which is closely related to $h$. When normalising by $\beta$, the total stress exerted at all positions, in the low Froude number case, a diameter-based control ($\mathrm{Re}_D$) has been identified. However, this effect is not seen when all experiments are considered en masse (Table 3.2). Hence, higher Froude numbers appear to lose any effect of diameter at controlling peak stress values. In the low Froude number case, these effects are secondary and indirect, only discernible when normalising over $\beta$.

#### 3.3.2.2 The controlling parameter during instances when high turbulent stresses are exerted

This section finds the control parameters for the stresses from a consideration of the high stress state frames. More details about the methodology can be found in paragraphs 2 and 3 of Section 3.3.1.2. The percentage of the selected total number of frames ranged from 4.98 to 6.82% over the eleven experiments. The summation of the stress magnitude exceedance at the peak stress locations of the single points contributed from 27.33 to 34.13% of the $\sum|u'w'|$ for each of the different experiment. The results of the classification are shown in the second to fourth columns of Table 3.6 under the 'Single Point' identifier. The results are showing that experiments 1, 2, 3, 4, 5 and 8 be grouped together with a clear first cluster dominance. However, experiment 8 has no significant dominance of $C_{k_1}$ over $C_{k_2}$. For the same experiments, Fig. 3.3 shows that the values of $\gamma/\beta$ for the 10-20 points with hollow symbols closest to the cylinder are increasing dramatically. That is because the HV system is further extended to the upstream of the cylinder, due to the fact that these experiments have the biggest cylinder diameter.

Another method named the whole frame approach was employed to confirm the consistency of the results of clustering of the vorticity fields based on the single point hole size exceedance results. More details about the whole frame approach can be found in paragraph 5 in Section 3.3.1.2. Again two groups were selected for the $K$-Means classification, and the number of frames corresponding to each cluster over the eleven experiments is shown in columns 5 to 7 of Table 3.6 under the 'Whole Frame' heading. These results identify experiments 1, 2, 3, 4, 5 and 8 as belonging to one group. The results are not very different to those for the single point approaches. However, it is only slightly biased towards $C_{k_2}$. The results from experiments 1-5 and 8 in Table 3.6, show that the cylinder diameter affects the whole HV system in a similar way as it does the near-bed conditions only.

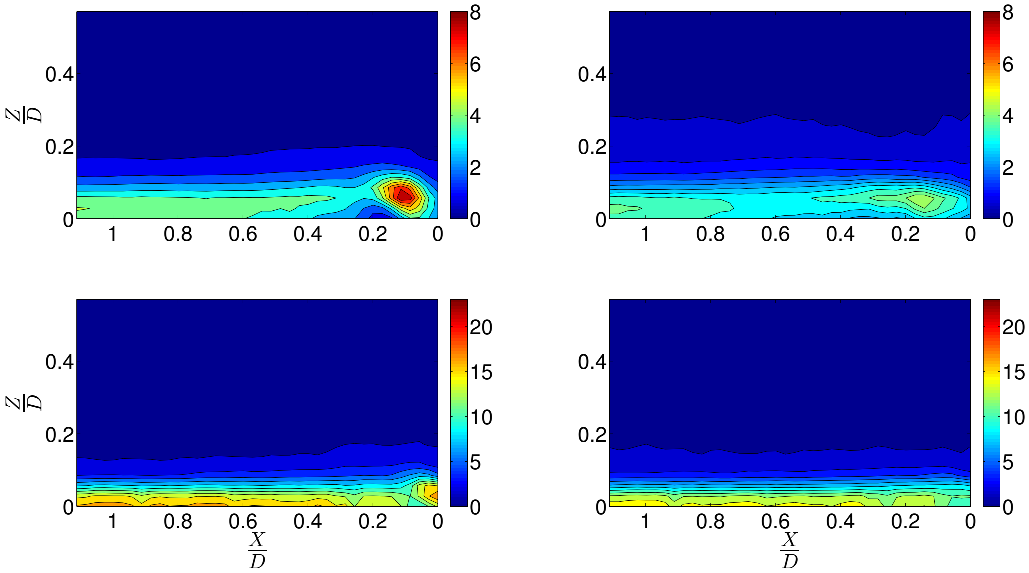

Figure 3.7: The centroids of the clusters extracted from the vorticity fields $\omega$ $(s^{-1})$ over the first eleven experiments. Results on the left are for the single point analysis while those on the right are for the whole frame method. Centroid of cluster 1 is shown at the top and of cluster 2 at the bottom in each case. The origin for the horizontal axis is the upstream edge of the cylinder. The plots are for turbulent stresses from experiments of Fr=0.015-0.2.

The four centroids for clusters $K_1$ and $K_2$ are shown in Figure 3.7 where the right-hand part shows the two centroids that belongs to the whole frame analysis. Therefore, experiments 1-5, and 8 are identified mainly with the flow field seen in the top right, which has a more spatially extensive HV system in the vertical plane and the HV system is more defined. Cluster 2 field predominantly reflects the results for experiments 6, 7, 9, 10 and 11. In these cases, diameters are smaller and the HV system, although of a similar longitudinal extent, is less intensive and is confined to a narrower vertical extent. However, the centroids of the two approaches are looking different, when the HV system is better defined in the left hand side panels of Figure 3.7 than in the right side, although they have very similar clustering results in Table 3.6 and this reflects that they have similar physical interpretation. They do not look similar because of the identical vorticity scale, in both of the identical clusters, prevents the lower magnitude vorticity to manifest itself, as the single point

Table 3.6: The number of frames from each experiment allocated to the two clusters found from the $K$-Means analysis ($C_{k_1}$ and $C_{k_2}$), as well as the classifier used to define cluster membership for each experiment $(C_{k_1} - C_{k_2})/(C_{k_1} + C_{k_2})$. The two groups of results represent frames chosen using a single point near the bed on the one hand, and using the whole frame points on the other. Results with a strong positive value for $(C_{k_1} - C_{k_2})/(C_{k_1} + C_{k_2})$ are shown in bold, the results are for the turbulent stresses from experiments of Fr=0.015-0.2.

| | Single Point | | | Whole Frame | | |
|---|---|---|---|---|---|---|
| Experiment | $C_{k_1}$ | $C_{k_2}$ | $\frac{C_{k_1}-C_{k_2}}{C_{k_1}+C_{k_2}}$ | $C_{k_1}$ | $C_{k_2}$ | $\frac{C_{k_1}-C_{k_2}}{C_{k_1}+C_{k_2}}$ |
| 1 | 288 | 0 | **+1.0** | 288 | 0 | **+1.0** |
| 2 | 287 | 0 | **+1.0** | 287 | 0 | **+1.0** |
| 3 | 224 | 0 | **+1.0** | 224 | 0 | **+1.0** |
| 4 | 241 | 0 | **+1.0** | 241 | 0 | **+1.0** |
| 5 | 229 | 0 | **+1.0** | 229 | 0 | **+1.0** |
| 6 | 128 | 179 | -0.17 | 79 | 228 | -0.49 |
| 7 | 125 | 157 | -0.11 | 101 | 181 | -0.28 |
| 8 | 237 | 44 | **+0.69** | 206 | 75 | **+0.47** |
| 9 | 2 | 247 | -0.98 | 0 | 249 | -1.0 |
| 10 | 0 | 240 | -1.0 | 0 | 240 | -1.0 |
| 11 | 0 | 233 | -1.0 | 0 | 233 | -1.0 |

approach is better in capturing the high vorticity events.

It is shown in Fig. 3.8, from the second mode from the POD of the vorticity fields, that the geometry of the HV system is getting more distinguishable when both Fr and $D$ increase. Hence, for experiments 1-5 with increasing Fr and constant $D$, the HV system became more defined and from Table 3.3 the enstrophy values increased from 342 to 1591 $s^{-2}$ for the same experiments. The case is also similar for experiments 6, 7, and 8 when the cylinder diameter has increased from 0.015 $m$ to 0.055 $m$ while Fr remained constant at 0.059. However, in the last group of experiments (experiments 9 to 11) the effect of diameter is dominant as the HV system became less recognised as $D$ decreased, while the Fr increased. Figure 3.8 explains how a clear recognition of the HV system couldn't be achieved with very low Fr. For instance, the cases when Fr=0.015, $D = 0.055$ $m$, and Fr=0.02, $D = 0.055$ $m$, did not yield a clear HV system and these two cases had the lowest enstrophy values.

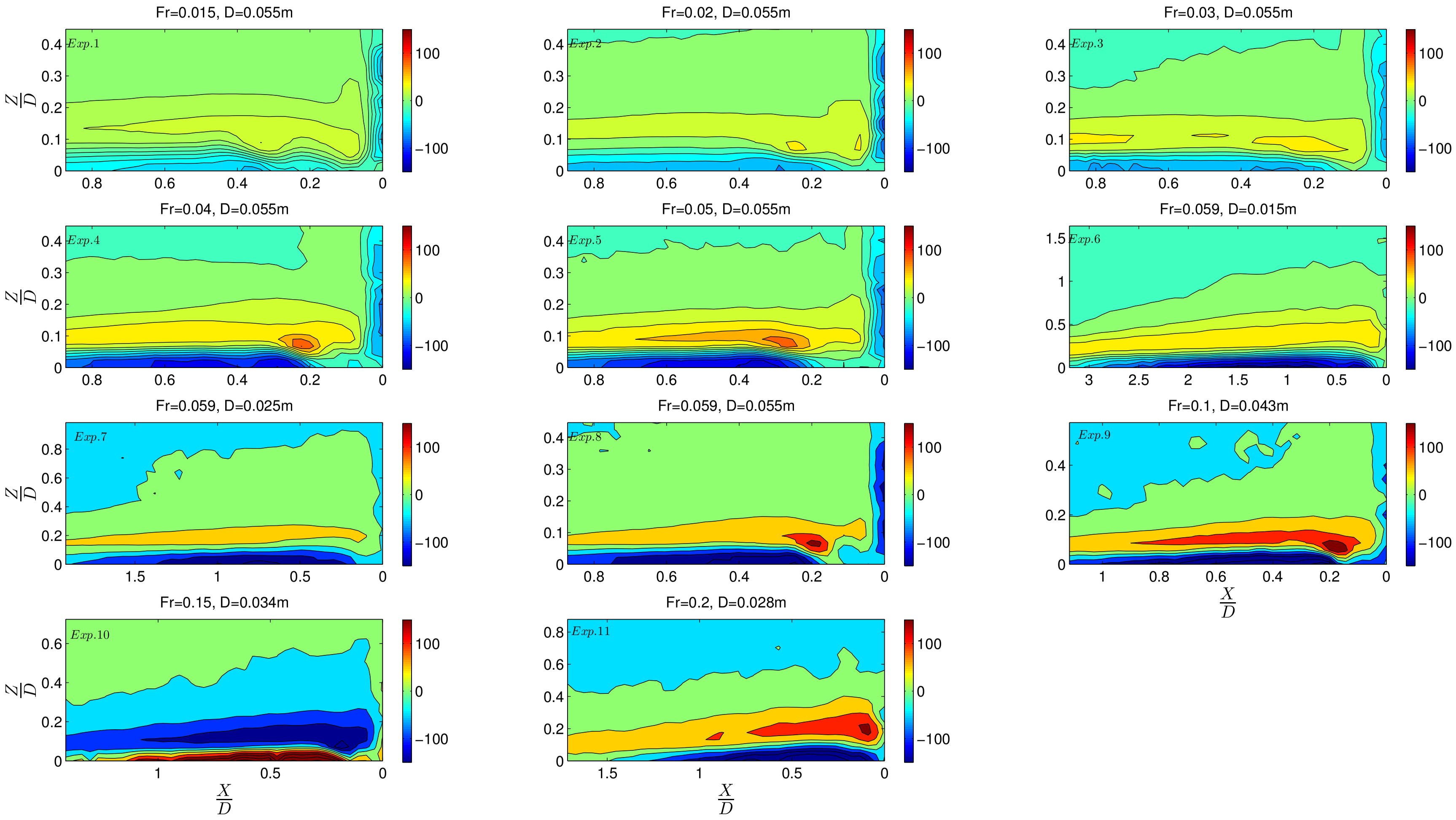

Figure 3.8: Mode 2 from the POD of the vorticity field (units of $s^{-1}$), showing the HV system for experiments 1 to 11 of Table 2.1.

### 3.3.3 Upper Sub-critical to Super-critical Froude Numbers (Fr $\in \{0.6 - 2.46\}$)

In this section, the other part of the wide range of Froude numbers experiments has been analysed to studying the effect of upper sub-critical to super-critical flow conditions (Fr=0.6-2.46) on the dynamics of the HV system upstream of the circular cylinder. Once more, two types of analysis have been undertaken to separate which parameter is the most effective: stepwise regression and $K$-Means classification of the high stress cases.

#### 3.3.3.1 Stepwise regression analysis of the turbulent stresses

The conditional analysis in this section has been undertaken on experiments 15-25 shown in Table 3.1. The results of the stepwise regression analyses are shown in Table 3.7. The cylinder diameter and Fr are controlling the location of the peak value of the three quantities $\gamma$, $\gamma/U^2$ and $\gamma/\beta$ when the distance from the cylinder edge is measured in $mm$ while Re$_D$ is the only controller for the peak location if the distance is normalised by cylinder diameter. The approaching bulk flow velocity was the only parameter that controlled the value of $\gamma$, and there was no significant control when $\gamma_{max}$ was normalised by $U^2$ or $\beta$. These limited controls of the parameters on the response variables underpin the results from Sections 3.3.1.1 and 3.3.2.1 which show a share of most of the control variables. Therefore, the results from further analyses are needed to gain a greater understanding of the controlling parameters or more experiments needed in between of Fr=0.6 and 2.46.

Table 3.7: The predictor variables contributing significantly to a stepwise regression equation for the selected response variables, together with their significance levels and the $R^2$ associated with the regression equation for turbulent stresses. The results are for the case of experiments of Fr=0.6-2.46.

| Regression | $R^2$ | Pred. 1 | $p$-value | Pred. 2 | $p$-value |
|---|---|---|---|---|---|
| $x_{max}(\gamma, \gamma/U^2, \gamma/\beta)$ $(mm)$ | 0.977 | $D$ | $< 0.001$ | Fr | $< 0.001$ |
| $x_{max}(\gamma, \gamma/U^2, \gamma/\beta)$ $(\frac{x_{max}}{D})$ | 0.770 | Re$_D$ | 0.0013 | - | - |
| $\gamma_{max}$ | 0.886 | $U$ | $< 0.001$ | - | - |
| $(\gamma/U^2)_{max}$ | - | - | - | - | - |
| $(\gamma/\beta)_{max}$ | - | - | - | - | - |

#### 3.3.3.2 The controlling parameters during instances when high turbulent stresses are exerted

In this section, the aim is to find out which parameters have a dominant control on the dependent variables used to represent the HV system and if the results vary depending on if a single point is studied or the whole vorticity field. The dependence of the stresses was further explored by a consideration of the high stress state frames. More details about the methodology can be found in paragraphs 2 and 3 in Section 3.3.1.2. The total number of selected frames ranged from 5.20 to 6.69% over the eleven experiments. The summation of the stress magnitude exceedances at the peak stress location of the single point contributed from 24.68 to 34.37% of the $\sum |u'w'|$ for each of the different experiments.

Using the $K$-Means classifier, two groups of the vorticity fields for the selected frames were classified automatically into two clusters ($K_1$ and $K_2$), and the number of frames in each cluster ($C_{k_1}$ and $C_{k_2}$) was extracted using cross tabulation method. These results are shown in the second to fourth columns of Table 3.8 under the 'Single Point' identifier. The results are showing that the experiments are divided into two groups according to Fr, where experiments 15-23 grouped in one group and experiments 24, and 25 in another group of highest Froude numbers.

The clustering of the vorticity fields based on the single point hole size exceedance results was complemented by a whole frame approach. The method is explained in the fifth paragraph of Section 3.3.1.2. Again two groups were selected for the $K$-Means classification and the number of frames corresponding to each cluster over the eleven experiments is shown in columns 5 to 7 of Table 3.8 under the 'Whole Frame' heading. Also, these results identify experiments 15-23 as belonging to one group and experiments 24 and 25 belong to another group. Table 2.1 shows that this group of experiments share the smallest Fr. These results ensure that the single point and whole frame approaches are very similar in terms of their grouping of the frames.

The centroids for clusters $K_1$ and $K_2$ are shown in Figure 3.9 where the left-hand part shows the two centroids that belongs to the single point analysis. Experiments

Table 3.8: The number of frames from each experiment allocated to the two clusters found from the $K$-Means analysis ($C_{k_1}$ and $C_{k_2}$), as well as the classifier used to define cluster membership for each experiment $(C_{k_1} - C_{k_2})/(C_{k_1} + C_{k_2})$. The two groups of results represent frames chosen using a single point near the bed on the one hand, and using the whole frame points on the other. Results with a strong positive value for $(C_{k_1} - C_{k_2})/(C_{k_1} + C_{k_2})$ are shown in bold. The results are for the case of experiments of Fr=0.6-2.46.

| | Single Point | | | Whole Frame | | |
|---|---|---|---|---|---|---|
| Experiment | $C_{k_1}$ | $C_{k_2}$ | $\frac{C_{k_1}-C_{k_2}}{C_{k_1}+C_{k_2}}$ | $C_{k_1}$ | $C_{k_2}$ | $\frac{C_{k_1}-C_{k_2}}{C_{k_1}+C_{k_2}}$ |
| 15 | 248 | 0 | **+1.0** | 248 | 0 | **+1.0** |
| 16 | 240 | 0 | **+1.0** | 240 | 0 | **+1.0** |
| 17 | 271 | 0 | **+1.0** | 271 | 0 | **+1.0** |
| 18 | 259 | 0 | **+1.0** | 259 | 0 | **+1.0** |
| 19 | 265 | 0 | **+1.0** | 265 | 0 | **+1.0** |
| 20 | 246 | 0 | **+1.0** | 246 | 0 | **+1.0** |
| 21 | 280 | 0 | **+1.0** | 280 | 0 | **+1.0** |
| 22 | 254 | 0 | **+1.0** | 254 | 0 | **+1.0** |
| 23 | 234 | 0 | **+1.0** | 234 | 0 | **+1.0** |
| 24 | 39 | 233 | -0.71 | 41 | 231 | -0.70 |
| 25 | 0 | 301 | -1.0 | 0 | 301 | -1.0 |

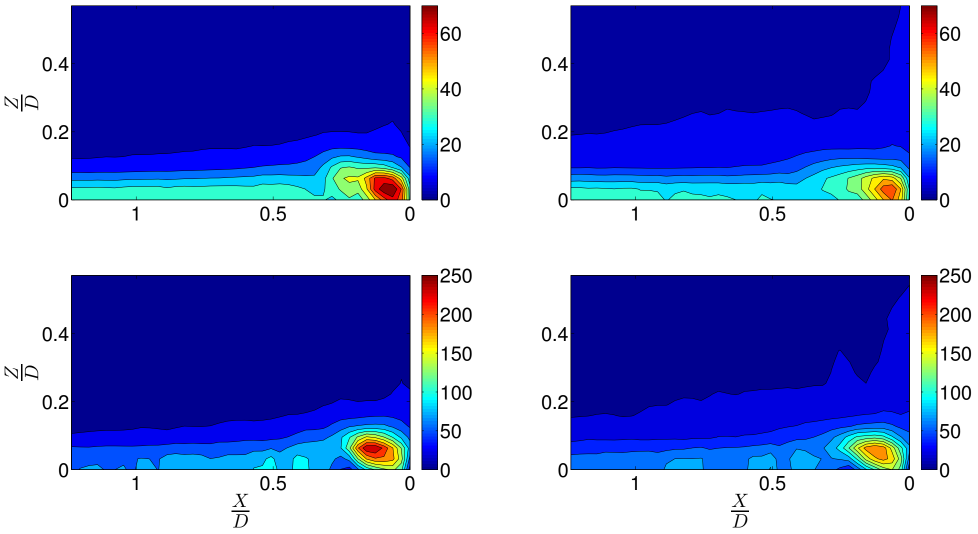

Figure 3.9: The centroids of the clusters extracted from the vorticity fields $\omega$ $(s^{-1})$ over the eleven experiments. Results on the left are for the single point analysis while those on the right are for the whole frame method. Centroid of cluster 1 is shown at the top and of cluster 2 at the bottom in each case. The origin for the horizontal axis is the upstream edge of the cylinder. The results are for the case of experiments of Fr=0.6-2.46.

15-23 are identified mainly with the flow field seen in the top left, which has one main vortex elongated in the upstream direction relative to the more compact vortex seen in cluster 2. In both cases, the vortex close to the cylinder is well defined, bigger in size and with higher vorticity magnitude, while any secondary structure is smaller in size and with a much reduced vorticity. The cluster 2 centroid reflects the results for experiments 24 and 25; there are also two vortices with different sizes and intensities. Results based on the single point approach exhibit little difference from the whole frame approach, although the centroids have a reduced vorticity intensity for both of the clusters.

## 3.4 Turbulent Stresses in front of the Cylinder Disaggregated by Quadrants

In this section, there is examination of the stress distribution in greater detail by partitioning the stresses by quadrants. The same points used in Section 3.3 are used in these analyses, and the peak stress for each experiment (which always occurred in quadrant 2) was used to summarise the measured turbulent stresses. The basic data underpinning the analysis in the section is shown in Table 3.9.

A parameter denoted as $\alpha$ is calculated from equation 2.6 and normalised by three quantities, the square of the approaching bulk flow velocity $U^2$, summation of the mean absolute stresses over all 40 positions $\beta$ which is calculated from equation 2.7, and the mean of absolute stresses at a given position $\gamma$ which is calculated from equation 2.8. The results are shown in Figs. 3.10, 3.11, and 3.12 respectively. These three quantities are calculated from 40 points near-bed and upstream of the cylinder. The abscissa in each panel is the distance from the upstream edge of the cylinder. Figure 3.10 shows the response of turbulence production to the HV system while, Figure 3.11 shows the relative contribution of $|u'w'|$ at each position to the summation of the mean absolute values of all of the 40 sites $\alpha/\beta$ and it is noted that there is a clear difference in the four curves (each representing a quadrant) in the 25 plots as one moves towards the cylinder. This change is clearly a consequence of the HV system (Devenport and Simpson, 1990; Sumer et al., 1997). However, the nature of these patterns varies for the different conditions of the experiments. Increases in the turbulent stresses are related to the cylinder diameter and constrained to the non-dimensional distance of ($X/D \leq 0.45$). It is also noted from Figures 3.10 and 3.11, how the magnitude of the two quantities is increasing with both the diameter and Fr and the peak value for $\alpha/\beta$ is always between 1-2.6% in all of the cases.

Fig. 3.12 illustrates the contribution of turbulent stresses of each quadrant relative to the total stresses in the same position that the contribution of the quadrants is approximately equal in the region upstream to the HV formations, for ($X/D > 0.5$), for the cases of very lower part of sub-critical flow conditions (Fr=0.015-0.05, $D = 0.055\ m$), this is something interesting to be explored more as part of future research. For the rest of the cases and for the same extension from the cylinder, the contribution from quadrants 2 and 4 shown in red and blue respectively, is always dominant.

From looking at the experiments of low Fr, it is noticed from the plots that represent them in Figures 3.10 and 3.11, that there is a slight increase in $\alpha/U^2$ and $\alpha/\beta$ respectively can be seen when moving from the furthest point towards the cylinder and up to a point when the increase is more recognised and that is located at $X/D \cong 0.45$, that is because of the further effect of cylinder diameter on the turbulent stresses. This trend indicates the upstream extent of the HV system where its effect is actually starts from those referred locations.

For the same experiments of (Fr=0.015-0.05) shown in Figure 3.10, the contribution from the four quadrants is approximately similar for the majority of these points except for the same indicated locations and cases closest to the cylinder ($X/D < 0.45$) where the contribution is greatest from quadrant 2 followed by quadrant 4 and then for quadrants 1 and 3. The mean values of the points upstream to the HV system ($X/D > 0.45$) are approximately 1-4 times lower than the peaks experienced in the HV region. For all of the experiments the peak of the absolute stress is coming from quadrant 2 except for the three lowest Froude numbers Fr=0.015, 0.02, and 0.03 sharing a diameter $D = 0.055\ m$ where the stresses are from quadrant 3. However, quadrant 2 peak mean absolute stresses value and its location were the primary dependent variables used in the stepwise regression analysis (Table 3.9). The peak locations are identical for $\alpha/U^2$ and $\alpha/\beta$, but different form $\alpha/\gamma$.

Table 3.9: Dependent variables used in the stepwise regression. The predictor variables are given in Table 2.1. The results are for the case of turbulent stresses distributed by quadrants for experiments of Fr=0.015-2.46.

| Exp. No. | $x_{max}(\alpha/U^2$ and $\alpha/\beta)$ $(mm)$ | $x_{max}(\alpha/U^2$ and $\alpha/\beta)$ $(\frac{x_{max}}{D})$ | $(\alpha/U^2)_{max}$ | $(\alpha/\beta)_{max}$ (%) | $x_{max}(\alpha/\gamma)$ $(mm)$ | $x_{max}(\alpha/\gamma)$ $(\frac{x_{max}}{D})$ | $(\alpha/\gamma)_{max}$ (%) | Quadrant cross-over for $\alpha/\gamma$ $(mm)$ | Quadrant cross-over for $\alpha/\gamma$ $(\frac{X}{D})$ |
|---|---|---|---|---|---|---|---|---|---|
| 1 | 17.23 | 0.313 | 8.34 | 1.27 | 19.69 | 0.358 | 37.87 | 6.15 | 0.112 |
| 2 | 12.31 | 0.224 | 9.64 | 1.50 | 19.69 | 0.358 | 36.38 | 6.15 | 0.112 |
| 3 | 9.85 | 0.179 | 11.71 | 1.54 | 14.77 | 0.269 | 35.39 | 7.39 | 0.134 |
| 4 | 12.31 | 0.224 | 16.36 | 2.05 | 13.54 | 0.246 | 42.24 | 8.62 | 0.157 |
| 5 | 9.85 | 0.179 | 18.59 | 2.22 | 17.23 | 0.313 | 41.69 | 8.62 | 0.157 |
| 6 | 3.69 | 0.246 | 4.62 | 1.82 | 11.08 | 0.739 | 37.42 | 1.23 | 0.082 |
| 7 | 6.15 | 0.246 | 6.55 | 2.31 | 8.62 | 0.345 | 41.41 | 2.46 | 0.099 |
| 8 | 11.08 | 0.201 | 13.30 | 3.33 | 12.31 | 0.224 | 49.28 | 7.39 | 0.134 |
| 9 | 7.39 | 0.172 | 13.05 | 2.61 | 11.08 | 0.258 | 45.65 | 6.15 | 0.143 |
| 10 | 7.39 | 0.217 | 10.79 | 2.04 | 8.62 | 0.253 | 44.25 | 4.92 | 0.145 |
| 11 | 6.15 | 0.220 | 10.75 | 2.18 | 7.39 | 0.264 | 42.91 | 3.69 | 0.132 |
| 12 | 4.92 | 0.197 | 8.66 | 1.81 | 6.15 | 0.246 | 40.74 | 1.23 | 0.049 |
| 13 | 8.62 | 0.205 | 26.71 | 3.55 | 9.45 | 0.234 | 54.05 | 3.69 | 0.088 |
| 14 | 11.08 | 0.201 | 34.36 | 3.76 | 13.54 | 0.246 | 54.01 | 4.92 | 0.089 |
| 15 | 4.92 | 0.197 | 9.09 | 2.01 | 6.15 | 0.246 | 44.27 | 3.69 | 0.148 |
| 16 | 8.62 | 0.205 | 28.26 | 3.77 | 9.85 | 0.234 | 55.79 | 4.92 | 0.117 |
| 17 | 14.77 | 0.234 | 29.08 | 3.26 | 16.00 | 0.254 | 54.99 | 4.92 | 0.078 |
| 18 | 7.39 | 0.231 | 15.80 | 3.16 | 8.62 | 0.269 | 49.60 | 3.69 | 0.115 |
| 19 | 6.15 | 0.228 | 10.01 | 2.62 | 6.15 | 0.228 | 47.25 | 3.69 | 0.137 |
| 20 | 8.62 | 0.192 | 8.64 | 2.71 | 11.08 | 0.246 | 52.42 | 3.69 | 0.082 |
| 21 | 16.00 | 0.254 | 13.47 | 3.23 | 16.00 | 0.254 | 55.90 | 4.92 | 0.078 |
| 22 | 7.39 | 0.295 | 10.32 | 2.22 | 7.39 | 0.295 | 49.12 | 2.46 | 0.099 |
| 23 | 4.92 | 0.197 | 15.20 | 2.87 | 7.39 | 0.295 | 48.88 | 2.46 | 0.099 |
| 24 | 9.85 | 0.246 | 20.13 | 3.42 | 12.31 | 0.308 | 53.66 | 3.69 | 0.092 |
| 25 | 11.08 | 0.277 | 27.68 | 3.07 | 12.31 | 0.308 | 53.53 | 3.69 | 0.092 |

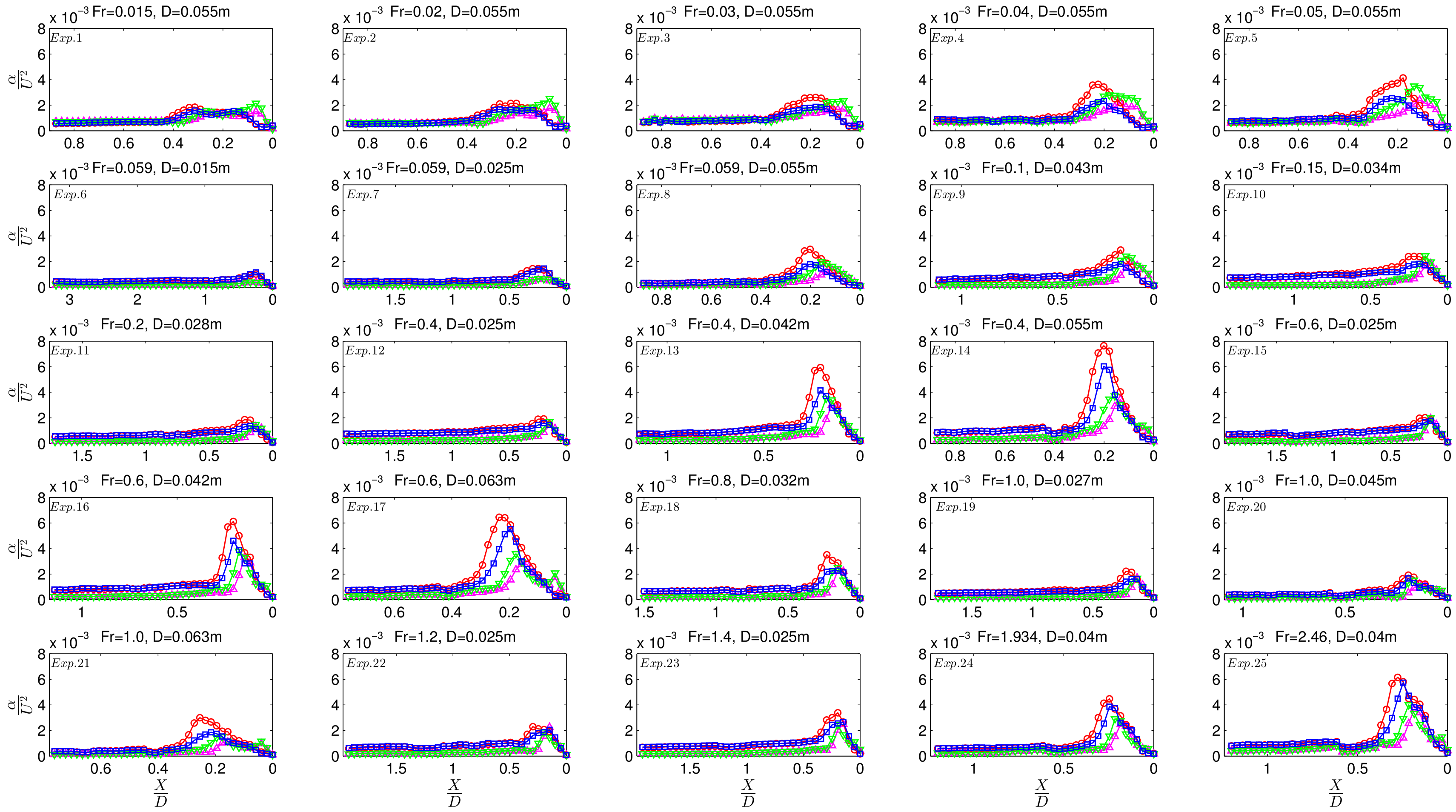

Figure 3.10: Mean of absolute contributions of turbulent stresses of each quadrant normalised by the square of the approaching bulk flow velocity $\frac{\alpha}{U^2}$. The abscissa indicates distance upstream from the upstream edge of the cylinder. As given in Table 2.3, $\triangle$, $\bigcirc$, $\bigtriangledown$, and $\square$ indicate the results for quadrants 1 to 4, respectively. The results are for the case of turbulent stresses distributed by quadrants for experiments of Fr=0.015-2.46.

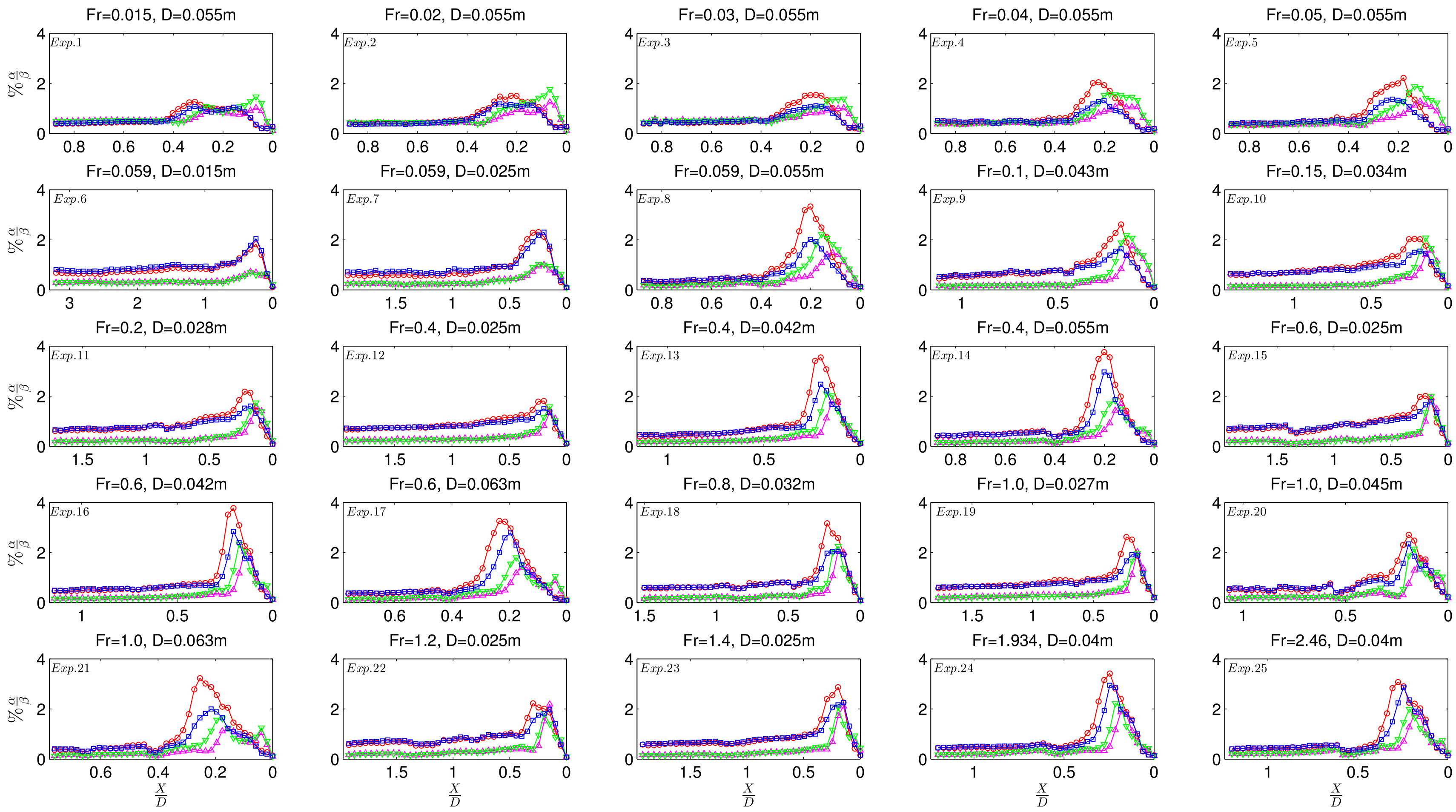

Figure 3.11: Mean of absolute contributions of turbulent stresses of each quadrant normalised by the summation means of absolute covariances over all forty positions, $\frac{\alpha}{\beta}$. The abscissa indicates distance upstream from the upstream edge of the cylinder. As given in Table 2.3, △, ○, ▽, and □ indicate the results for quadrants 1 to 4, respectively. Fr=0.015-2.46.

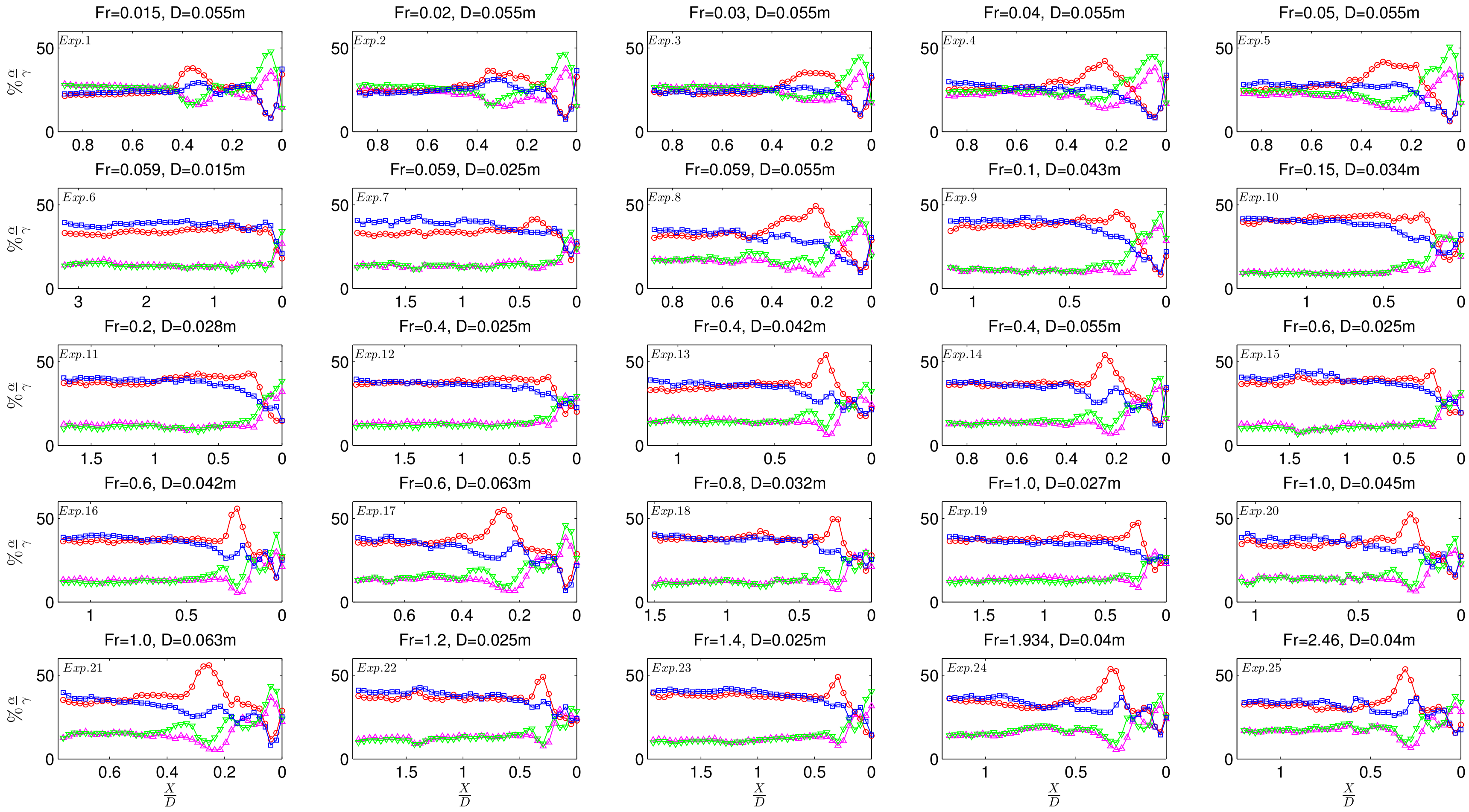

Figure 3.12: Mean of absolute contributions of turbulent stresses of each quadrant normalised by the summation of means of absolute covariance of each position, $\frac{\alpha}{\gamma}$. The abscissa indicates distance upstream from the upstream edge of the cylinder. As given in Table 2.3, △, ○, ▽, and □ indicate the results for quadrants 1 to 4, respectively. Fr=0.015-2.46.

From the furthest point under the HV system to approximately $X/D \geqslant 0.2$ quadrant 2 and quadrant 4 contribute the most to the stresses in the HV system, while for approximately $X/D = 0.05 - 0.2$ from the cylinder, this pattern is found to be reversed with greater stresses exerted by quadrant 1 and quadrant 3. This result is clearer in Fig. 3.12 indicating that of the order of 70% of the total turbulent stresses is from these quadrants in this region. The distance to this crossover position in both *mm* and $X/D$ for $\alpha/\gamma$ were also employed in the regression analysis. For the case of high Fr that shown in plots of experiments 15-25 of Figure 3.10, the behaviour of the points is not very different from the previous experiments apart from the lowest values of $\alpha/U^2$ of the four quadrants outside of the area of the HV activity, in which it is for locations at $X/D \geqslant 0.4$. The difference between the mean values for the positions of slightly affected boundary layer and the peak values of the same experiment varies significantly. For instance, the difference is about a double in experiment 15, while it is 7 times in experiment 17. Hence it is an expression for the relative importance of the stresses exerted by the HV system due to the different flow conditions. Also, it is shown from figure 3.12 that the difference in the contribution of the 4 quadrants is the smallest at the highest Froude number cases (Fr=1.934 and 2.46) among the same group of high Fr experiments.

The peak of the mean absolute stresses value of quadrant 2 and its location were used as the primary dependent variables in the stepwise regression analysis, and they are shown is Table 3.9.

### 3.4.1 Sub-critical to Super-critical Froude Numbers (Fr $\in \{0.015 - 2.46\}$)

In this section, the effect of control variables on the HV system in different flow conditions is investigated. There are twenty five experiments used in these analyses. This investigation commences by choosing the peak point out of the 40 locations to represent the whole set of points near the bed. The stress effect is partitioned into four quadrants and the magnitude of quadrant-based turbulent stresses, and location of the peak point of the quadrant that contributes the most to the stresses, will be used as criteria to normalise the response at the other points. This was quadrant 2 in all cases.

#### 3.4.1.1 Stepwise regression analysis of the turbulent stresses

The stepwise regression results of Table 3.10 show the diameter, $D$, controls the prediction of the quadrant 2 for maximum mean of the absolute stresses location for both $\alpha/U^2$ and $\alpha/\beta$ when the distance from the cylinder edge is in $mm$. Therefore it is an important factor in prediction of the location of the maximum stresses exerted by the HV system. However, no control parameter is shown to be significant when the distance is normalised by cylinder diameter, and that is the direct effect of distance normlisation by $D$. Staying with the same dependent variables, the peak value of $\alpha/U^2$ was controlled by $h$ and $D$, while the peak value of $\alpha/\beta$ was controlled by $\mathrm{Re}_D$. Hence, the two variables are responding to different control parameters when peak magnitudes are investigated, even though the location of the peak is controlled by the same variable. Cylinder diameter and flow depth swapped the leading role in governing the quadrant 2 peak location for $\alpha/\gamma$ with $D$ dominant when the distance taken in $mm$ and $h$ leading when the distance was normalised by $D$. $\mathrm{Re}_D$ was important for controlling the peak value of $\alpha/\gamma$.

The last dependent parameter in this table is the location of the cross-over between the quadrants exerting maximal stresses, both in $mm$ and $X/D$. This parameter have been chosen to study the phenomenon of the change of the quadrants pattern for the points close to the cylinder edge, which may be considered a direct consequence of the action of the HV system. Cylinder diameter and $\mathrm{Re}_D$ govern the location when it is measured in $mm$, while the $\mathrm{Re}_D$ is the unique control as the distance is in $X/D$. Hence, there is clear evidence for the physical relevance of non-dimensionalisation of distances by $D$. The multiple existence of $\mathrm{Re}_D$ as a control parameter is consistent with the literature, where $\mathrm{Re}_D$ is often used to scale these types of experiments (Baker, 1979, 1980; Dargahi, 1989; Baker, 1991; Simpson, 2001). Figure 3.13, shows the cases where the $R^2$ values are of the highest, and in all of the three cases represented by the three plots, cylinder diameter is the most significant parameter that affects the location and magnitude of the peak stresses, as well as the quadrants cross-over for $(\alpha/\gamma)$.

Table 3.10: The predictor variables contributing significantly to a stepwise regression equation for the selected response variables, together with their significance levels and the $R^2$ associated with the regression equation for turbulent stresses distributed by quadrants. The results are for experiments of Fr=0.015-2.46.

| Regression | $R^2$ | Pred. 1 | $p$-value | Pred. 2 | $p$-value |
|---|---|---|---|---|---|
| $x_{max}$ $(\alpha/U^2$ and $\alpha/\beta)$ $(mm)$ | 0.828 | $D$ | $< 0.001$ | - | - |
| $x_{max}(\alpha/U^2$ and $\alpha/\beta)$ $(\frac{x_{max}}{D})$ | - | - | - | - | - |
| $(\alpha/U^2)_{max}$ | 0.641 | $h$ | 0.0045 | $D$ | 0.0083 |
| $(\alpha/\beta)_{max}$ | 0.607 | $\mathrm{Re}_D$ | 0.0017 | - | - |
| $x_{max}(\alpha/\gamma)$ $(mm)$ | 0.822 | $D$ | $< 0.001$ | $h$ | 0.0059 |
| $x_{max}(\alpha/\gamma)$ $(\frac{x_{max}}{D})$ | 0.632 | $h$ | 0.0029 | $D$ | 0.0288 |
| $(\alpha/\gamma)_{max}$ | 0.694 | $\mathrm{Re}_D$ | $< 0.001$ | - | - |
| Quadrant cross-over for $\alpha/\gamma$ $(mm)$ | 0.829 | $D$ | $< 0.001$ | $\mathrm{Re}_D$ | 0.0059 |
| Quadrant cross-over for $\alpha/\gamma$ $(\frac{X}{D})$ | 0.554 | $\mathrm{Re}_D$ | 0.0267 | - | - |

#### 3.4.1.2 The controlling parameter during instances when high turbulent stresses are exerted

In light of the results from the stepwise regression that showed a significant effect of flow depth and cylinder diameter Reynolds number on the magnitude of the predictor parameters, the HV system dependency was further explored. The maximum observed value and position for $\alpha/\beta$ at a single point for the dominant quadrant (quadrant 2), have been chosen as a criterion for this exploration. The high stress state frames, which must dominate the quadrant-dependent values for $|u'w'|$ were separated using the same methodology introduced in Section 3.3.1.2. The frames corresponding to these instances were extracted and the percentage of the overall number of frames selected ranged from 4.84 to 7.02% over the twenty five experiments. The summation of the stress magnitudes at the peak mean stresses locations for these frames contributed from 27.08 to 40.93% of $\sum |u'w'|$ over all frames in each different experiment.

Using the $K$-Means classifier, three groups ($k_1$, $k_2$, and $k_3$) of the vorticity fields were automatically classified and the number of frames in each cluster ($C_{k_1}$, $C_{k_2}$ and $C_{k_3}$) was extracted. The second to forth columns of Table 3.11 shown in the results for the 'Single Point' identifier. The grouping of the results is clear for experiments

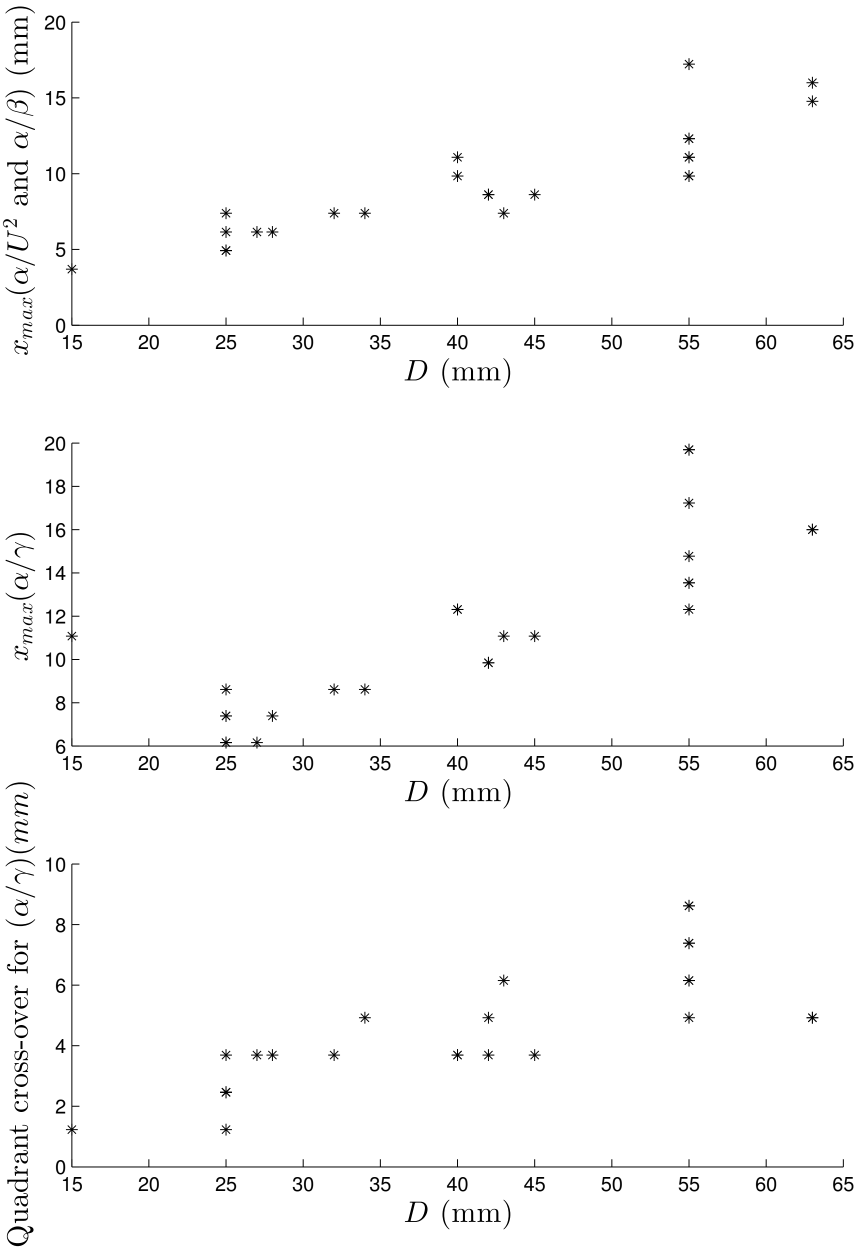

Figure 3.13: The relationships between the location of the peak stresses with the cylinder diameter.

1-11 with a clear first cluster dominance, experiments 12-23 were also clustered together in the second cluster and experiments 24 and 25 in the third cluster. Table 2.1 showed that the first experiments 1-11 have the lowest Fr, ranging from 0.015 to 0.2, experiments 12-23 having Fr of 0.4 to 1.4, and experiments 24 and 25 having the highest Fr of 1.936 and 2.46. To ensure the consistency of the results, a whole frame approach has been employed in addition to the clustering of the vorticity fields based on the single point hole size exceedance results.

The methodology is explained in paragraph 5 of Section 3.3.1.2. This time again three groups were selected for the $K$-Means classification and the number of frames corresponding to each cluster over the twenty five experiments is shown in columns 5 to 7 of Table 3.11 under the 'Whole Frame' heading. Results are very similar to the single point case, with experiments 1-11 belonging to one group, followed by experiments 12-23, and experiments 24-25 to the other two groups. Hence, the differences between the single point and whole frame approaches are minor. Thus, the Froude number not only affects the near-bed stresses exerted by the HV system, but also the stresses produced by the whole HV system.

The left-hand side part of Figure 3.14 shows the centroids for clusters $K_1$, $K_2$ and $K_3$ for the single point analysis from top to bottom respectively where the HV system is better defined in one case better than the other, more details are in Section 3.3.1.2. Therefore, experiments 1-11 are identified with the flow field seen in the top left, which has a clear vortex developed that is spatially extensive despite the relatively low peak vorticities relative to those seen for the other cluster centroids.

The cluster 2 centroid reflects the results for experiments 12-23 shown in the middle left hand side plot with higher magnitude of vorticity, the HV system is better defined with a higher magnitude although its spatial extent is less than what is seen in cluster 1. The vorticity magnitude is even higher in the third cluster where enstrophy is the greatest. The spatial extent of this system also increases again and the primary vortex is angled away from the wall due to the presence of an underlying secondary structure. Again results based on the single point define the HV in a better way than in the case of whole frame showing the significance of near-bed peak over frame-mean stresses. However, for cluster 3 from the whole-frame analysis, the existence of a set of vortices extending up to $X/D = 0.7$ from the cylinder can be discriminated. There is some evidence for their existence in the single-point analysis but they are less distinct. The extended spatial extent of the HV system in this case explains the variation in the stresses by quadrant seen for

Table 3.11: The number of frames from each experiment allocated to the three clusters found from the $K$-Means analysis ($C_{k_1}$ $C_{k_2}$ and $C_{k_3}$). The three groups of results represent frames chosen using a single point near the bed on the one hand, and using the whole frame points on the other. The results are for the case of turbulent stresses distributed by quadrants for experiments of Fr=0.015-2.46.

| | Single Point | | | Whole Frame | | |
|---|---|---|---|---|---|---|
| Experiment | $C_{k_1}$ | $C_{k_2}$ | $C_{k_3}$ | $C_{k_1}$ | $C_{k_2}$ | $C_{k_3}$ |
| 1 | 304 | 0 | 0 | 304 | 0 | 0 |
| 2 | 279 | 0 | 0 | 279 | 0 | 0 |
| 3 | 249 | 0 | 0 | 249 | 0 | 0 |
| 4 | 238 | 0 | 0 | 238 | 0 | 0 |
| 5 | 229 | 0 | 0 | 229 | 0 | 0 |
| 6 | 307 | 0 | 0 | 307 | 0 | 0 |
| 7 | 280 | 0 | 0 | 280 | 0 | 0 |
| 8 | 257 | 0 | 0 | 257 | 0 | 0 |
| 9 | 249 | 0 | 0 | 249 | 0 | 0 |
| 10 | 266 | 2 | 0 | 265 | 0 | 0 |
| 11 | 256 | 0 | 0 | 256 | 0 | 0 |
| 12 | 20 | 235 | 0 | 21 | 234 | 0 |
| 13 | 6 | 288 | 0 | 10 | 284 | 0 |
| 14 | 39 | 260 | 0 | 33 | 266 | 0 |
| 15 | 0 | 260 | 0 | 1 | 259 | 0 |
| 16 | 0 | 218 | 0 | 0 | 218 | 0 |
| 17 | 1 | 291 | 0 | 0 | 292 | 0 |
| 18 | 0 | 268 | 0 | 0 | 268 | 0 |
| 19 | 0 | 201 | 0 | 0 | 201 | 0 |
| 20 | 0 | 270 | 0 | 0 | 270 | 0 |
| 21 | 1 | 311 | 0 | 0 | 312 | 0 |
| 22 | 0 | 316 | 0 | 0 | 316 | 0 |
| 23 | 0 | 234 | 0 | 0 | 232 | 0 |
| 24 | 0 | 57 | 252 | 0 | 27 | 282 |
| 25 | 0 | 1 | 308 | 0 | 0 | 309 |

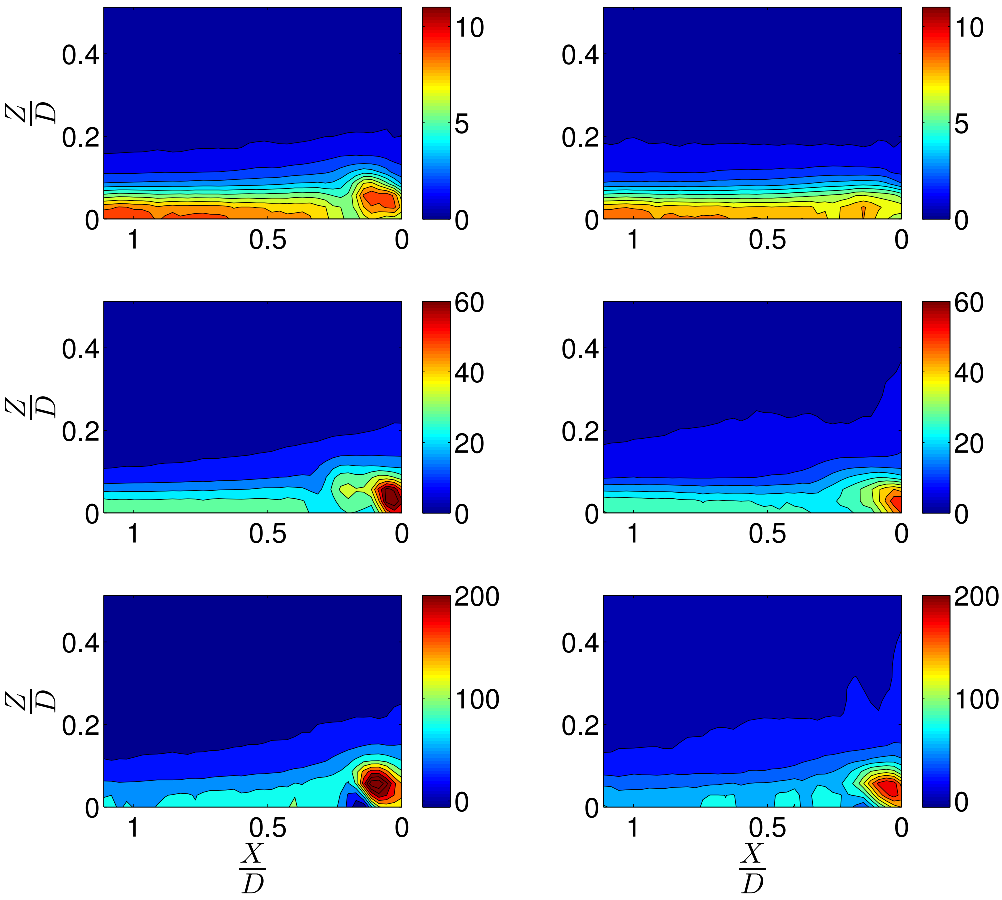

Figure 3.14: The centroids of the clusters extracted from the vorticity fields $\omega$ $(s^{-1})$ over the twenty five experiments. Results on the left are for the single point analysis while those on the right are for the whole frame method. Centroid of cluster 1 is shown at the top and of cluster 3 at the bottom in each case. The origin for the horizontal axis is the upstream edge of the cylinder. The results are for the case of turbulent stresses distributed by quadrants for experiments of Fr=0.015-2.46.

$X/D > 0.5$ in Fig. 3.12.

### 3.4.2 Lower Sub-critical Froude Numbers (Fr $\in \{0.015-0.2\}$)

These different flow conditions of low Froude numbers might change how different parameters control the dynamics of HV system upstream of the circular cylinder. Hence, the analyses in this part are applied on variables related to experiments 1-11 in Table 2.1. The eleven lowest values in the group of the experiments used in the analysis are selected to explore the effect of the controlling parameters on the characteristics of HV system in a range of lower sub-critical flow conditions, some measures are used to explore the HV system characteristics as in the following sections.

#### 3.4.2.1 Stepwise regression analysis of the turbulent stresses

It is shown from the results of stepwise regression analysis of Table 3.12 that a control of $D$ on the prediction of the location of quadrant 2 maximum mean stresses for both $\alpha/U^2$ and $\alpha/\beta$ when the distance from the cylinder edge is in $mm$. At the same time, the peak location of $\alpha/\gamma$ was controlled by $U$. The cylinder diameter effect and approaching flow depth appear to control the peak value of $\alpha/U^2$ and the location of quadrants cross-over for measurements of distances both in $mm$ and $X/D$. $\mathrm{Re}_D$ effect is shown in governing the peak values for $\alpha/\beta$ and $\alpha/\gamma$. The latter parameter prediction is consistent with what is in the literature when $\mathrm{Re}_D$ is often used to scale these types of experiments. Now, when comparing these results with the results from the whole range of flow conditions shown in Table 3.10, it is noticed that $D$ and $h$ control of the peak location of $\alpha/\gamma$ in $mm$ is replaced with $U$ and this is probably due to the effect of gentle bulk flow velocity and consequently the gentle part of turbulence that keeps the balance between the contribution of the different quadrants in a local measures. The other significant difference is when the $\mathrm{Re}_D$ control of quadrant cross-over for $\alpha/\gamma$ $(\frac{X}{D})$ is replaced with $h$ and $D$, and this is anticipated to the effect of the adverse pressure in the region just upstream of the edge of the cylinder where the incoming flow hits the cylinder and comes down and then reflects back from the cylinder generating the circulation responsible for the vortex formation.

#### 3.4.2.2 The controlling parameter during instances when high turbulent stresses are exerted

The frames corresponding to the high stress state times were extracted and the percentage of the number of frames selected ranged from 5.09 to 6.82% over the total number of frames in each of the eleven experiments. The summation of the stress magnitudes at the peak stresses locations for these frames contributed from 27.64

Table 3.12: The predictor variables contributing significantly to a stepwise regression equation for the selected response variables, together with their significance levels and the $R^2$ associated with the regression equation for turbulent stresses distributed by quadrants. The results are for experiments of Fr=0.015-0.2.

| Regression | $R^2$ | Pred. 1 | $p$-value | Pred. 2 | $p$-value |
|---|---|---|---|---|---|
| $x_{max}(\alpha/U^2$ and $\alpha/\beta)$ $(mm)$ | 0.772 | $D$ | 0.0012 | - | - |
| $x_{max}(\alpha/U^2$ and $\alpha/\beta)$ $(\frac{x_{max}}{D})$ | - | - | - | - | - |
| $(\alpha/U^2)_{max}$ | 0.778 | $D$ | 0.017 | $h$ | 0.024 |
| $(\alpha/\beta)_{max}$ | 0.685 | Re$_D$ | 0.01 | - | - |
| $x_{max}(\alpha/\gamma)$ $(mm)$ | 0.818 | $U$ | $< 0.001$ | - | - |
| $x_{max}(\alpha/\gamma)$ $(\frac{x_{max}}{D})$ | - | - | - | - | - |
| $(\alpha/\gamma)_{max}$ | 0.791 | Re$_D$ | $< 0.001$ | - | - |
| Quadrant cross-over for $\alpha/\gamma$ $(mm)$ | 0.940 | $D$ | $< 0.001$ | $h$ | 0.028 |
| Quadrant cross-over for $\alpha/\gamma$ $(\frac{X}{D})$ | 0.941 | $h$ | $< 0.001$ | $D$ | $< 0.001$ |

to 34.13% of the $\sum |u'w'|$ for each different experiment.

Two groups of the vorticity fields for the selected frames were classified automatically into ($K_1$ and $K_2$) using the $K$-Means classifier and the number of frames in each cluster ($C_{k_1}$ and $C_{k_2}$) was extracted using cross tabulation method. Results are shown for both single point and whole frame analyses as in Table 3.13. The results show that experiments 1, 2, 3, 4, 5 and 8 may be grouped together with a clear first cluster dominance in both single point and whole frame cases. Figure 3.10 shows that the values of $\alpha/U^2$ for these experiments are the highest among low Fr experiments. That is because the bigger the cylinder diameter is, the more turbulence is created in front of it and consequently the turbulent stresses of $\alpha$ are grater in the experiments that share the biggest cylinder diameter.

Figure 3.15 shows the two cluster's centroids for the single point and whole frame analyses. The centroid of cluster 1 has better defined HV system. The cluster 2 centroid reflects the results for experiments 6, 7, 9, 10 and 11. In these latter cases, diameters are smaller and the HV system is not defined and the region close to the bed is less extended in the vertical plane. The HV is slightly better defined in the centroids of $K_2$ of single point approach field, bottom left, than in $K_2$ of whole frame approach, bottom right. From this section it is learnt that having less number of experiments resulted in less number of clusters, as in Figs. 3.15 and 3.14, respectively. Also, it is noticed that the single point approach remained

Table 3.13: The number of frames from each experiment allocated to the two clusters found from the $K$-Means analysis ($C_{k_1}$ and $C_{k_2}$), as well as the classifier used to define cluster membership for each experiment $(C_{k_1} - C_{k_2})/(C_{k_1} + C_{k_2})$. The two groups of results represent frames chosen using a single point near the bed on the one hand, and using the whole frame points on the other. Results with a strong positive value for $(C_{k_1} - C_{k_2})/(C_{k_1} + C_{k_2})$ are shown in bold. The results are for the case of turbulent stresses distributed by quadrants for experiments of Fr=0.015-0.2.

| | Single Point | | | Whole Frame | | |
|---|---|---|---|---|---|---|
| Experiment | $C_{k_1}$ | $C_{k_2}$ | $\frac{C_{k_1}-C_{k_2}}{C_{k_1}+C_{k_2}}$ | $C_{k_1}$ | $C_{k_2}$ | $\frac{C_{k_1}-C_{k_2}}{C_{k_1}+C_{k_2}}$ |
| 1 | 304 | 0 | **+1.0** | 304 | 0 | **+1.0** |
| 2 | 279 | 0 | **+1.0** | 279 | 0 | **+1.0** |
| 3 | 249 | 0 | **+1.0** | 249 | 0 | **+1.0** |
| 4 | 238 | 0 | **+1.0** | 238 | 0 | **+1.0** |
| 5 | 229 | 0 | **+1.0** | 229 | 0 | **+1.0** |
| 6 | 103 | 204 | -0.33 | 81 | 226 | -0.47 |
| 7 | 70 | 210 | -0.50 | 105 | 175 | -0.25 |
| 8 | 203 | 54 | **+0.58** | 191 | 66 | **+0.49** |
| 9 | 1 | 248 | -0.99 | 0 | 249 | -1.0 |
| 10 | 0 | 268 | -1.0 | 0 | 268 | -1.0 |
| 11 | 0 | 256 | -1.0 | 0 | 256 | -1.0 |

better in capturing the more significant moments of turbulence that leads to higher magnitude of vorticity regardless of the flow conditions.

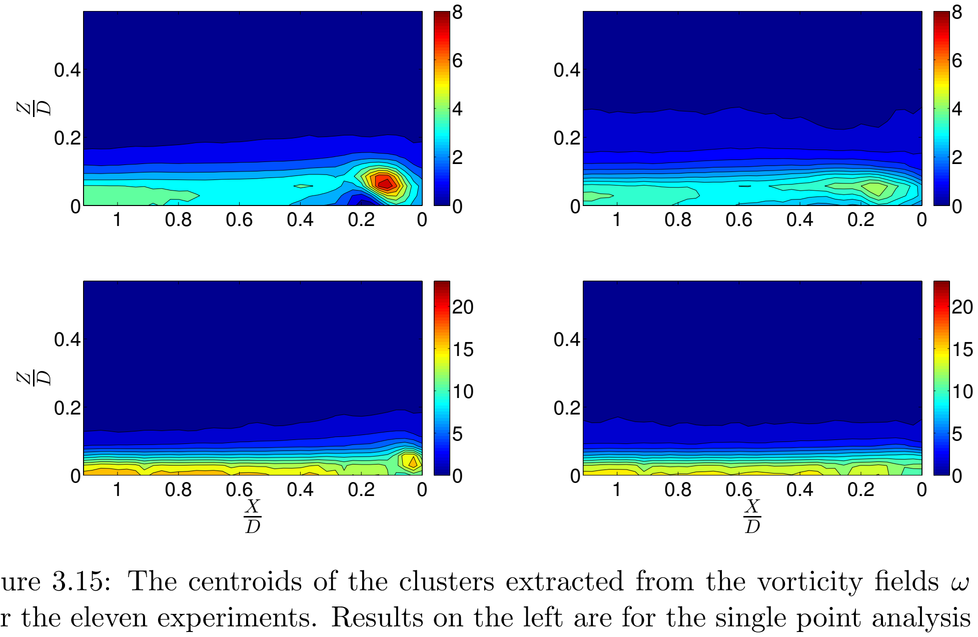

Figure 3.15: The centroids of the clusters extracted from the vorticity fields $\omega$ $(s^{-1})$ over the eleven experiments. Results on the left are for the single point analysis while those on the right are for the whole frame method. Centroid of cluster 1 is shown at the top and of cluster 2 at the bottom in each case. The origin for the horizontal axis is the upstream edge of the cylinder. The results are for the case of turbulent stresses distributed by quadrants for experiments of Fr=0.015-0.2.

### 3.4.3 Upper Sub-critical to Supper-critical Froude Numbers (Fr $\in \{0.6 - 2.46\}$)

The other part of the wide range of Froude numbers experiments is selected for this section to studying the effect of the case of upper sub-critical to supper-critical flow conditions (Fr=0.6-2.46) on the dynamics of the HV system upstream of the circular cylinder which might have different response to the control parameters than in the case of including whole range of flow conditions. The two following subsections are for the conducted analyses.

#### 3.4.3.1 Stepwise regression analysis of the turbulent stresses

It is shown from the results of the stepwise regression in Table 3.14 how the location of quadrant 2 maximum stress measured for the cylinder edge in $mm$ for $\alpha/U^2$ and $\alpha/\beta$ is controlled by the cylinder diameter, while no control is shown when the distance is normalised by $D$ and that is an evidence for the significant effect of normalisation by $D$. Also, the effect of the normalisation of the abscissa by $D$ is clear, not only in this case, but also when the peak location for $\alpha/\gamma$ is controlled by $D$ and Fr together before normalisation and with only the control of Fr hence after. While, the peak value of $\alpha/U^2$ and $\alpha/\beta$ is not controlled by any parameter. $\alpha/\gamma$ is only driven by $D$. For the quadrant cross-over location for $\alpha/\gamma$, $D$ and $h$ were the controlling variables in both cases, before and after normalisation and it is back to effect of $D$ in both cases for experiments 22-25 of Table 3.9. From these results it is noticed that most of the predictor variables are controlled by different parameters when testing the response with wider range of flow conditions. There is no control parameter shown for both the peak of $\alpha/U^2$ and $\alpha/\beta$, and that is due to the relatively high turbulence production for the experiments in this group. The high turbulence created a more chaotic values of $\alpha$ in which the normalisation by neither $U^2$ nor $\beta$ helped to make it more predictable or controlled by any parameter. This raise the issue for the need of more experiments to find out if it ends up with any controlling parameters. The other interesting difference is when the effect of Fr is obvious to control the location of the peak for $\alpha/\gamma$ and that came along with hypothesis that predicted an effect of Fr on the dynamics of the HV system.

Trying to explore qualitatively the effect of the flow parameters on the HV system, mode 2 of the vorticity field was plotted in Fig. 3.16. It has been found that there are vortices well recognised in experiments 16, 17, 20, and 21. From Table 2.1 these experiments share the largest cylinder diameters of 0.042 $m$, 0.063 $m$, 0.045 $m$ and 0.063 m respectively. The highest vorticity level was found in experiment 24 and 25 of Fr=1.934, and Fr=2.46 with $D = 0.04$ $m$, and that could be attributed to the relatively high velocity of the flow at 1.407 and 1.652 $m$ $\mathrm{s}^{-1}$ respectively. Also, there is an evidence for the significant higher turbulence production for these two experiments from their value of enstrophy shown in Table 3.3.

Table 3.14: The predictor variables contributing significantly to a stepwise regression equation for the selected response variables, together with their significance levels and the $R^2$ associated with the regression equation for turbulent stresses distributed by quadrants. The results are for experiments of Fr=0.6-2.46.

| Regression | $R^2$ | Pred. 1 | $p$-value | Pred. 2 | $p$-value |
|---|---|---|---|---|---|
| $x_{max}$ ($\alpha/U^2$ and $\alpha/\beta$) ($mm$) | 0.907 | $D$ | $< 0.001$ | - | - |
| $x_{max}$ ($\alpha/U^2$ and $\alpha/\beta$) ($\frac{x_{max}}{D}$) | - | - | - | - | - |
| $(\alpha/U^2)_{max}$ | - | - | - | - | - |
| $(\alpha/\beta)_{max}$ | - | - | - | - | - |
| $x_{max}(\alpha/\gamma)$ ($mm$) | 0.980 | $D$ | $< 0.001$ | Fr | 0.001 |
| $x_{max}(\alpha/\gamma)$ ($\frac{x_{max}}{D}$) | 0.739 | Fr | 0.0028 | - | - |
| $(\alpha/\gamma)_{max}$ | 0.765 | $D$ | 0.0015 | - | - |
| Quadrant cross-over for $\alpha/\gamma$ ($mm$) | 0.861 | $D$ | 0.0021 | $h$ | 0.0149 |
| Quadrant cross-over for $\alpha/\gamma$ ($\frac{X}{D}$) | 0.814 | $D$ | 0.0012 | $h$ | 0.0132 |

#### 3.4.3.2 The controlling parameter during instances when high turbulent stresses are exerted

The frames corresponding the high stress state instances were extracted and the percentage of the total number of the selected frames ranged from 4.84 to 7.02% over the eleven experiments. The summation of the stress magnitudes at the peak stress locations for these frames contributed from 27.08 to 40.93% of the $\sum |u'w'|$ for each different experiment.

Two clusters were extracted from the high stress state frames and the results in Table 3.15 show that the experiments are divided into two groups according to the

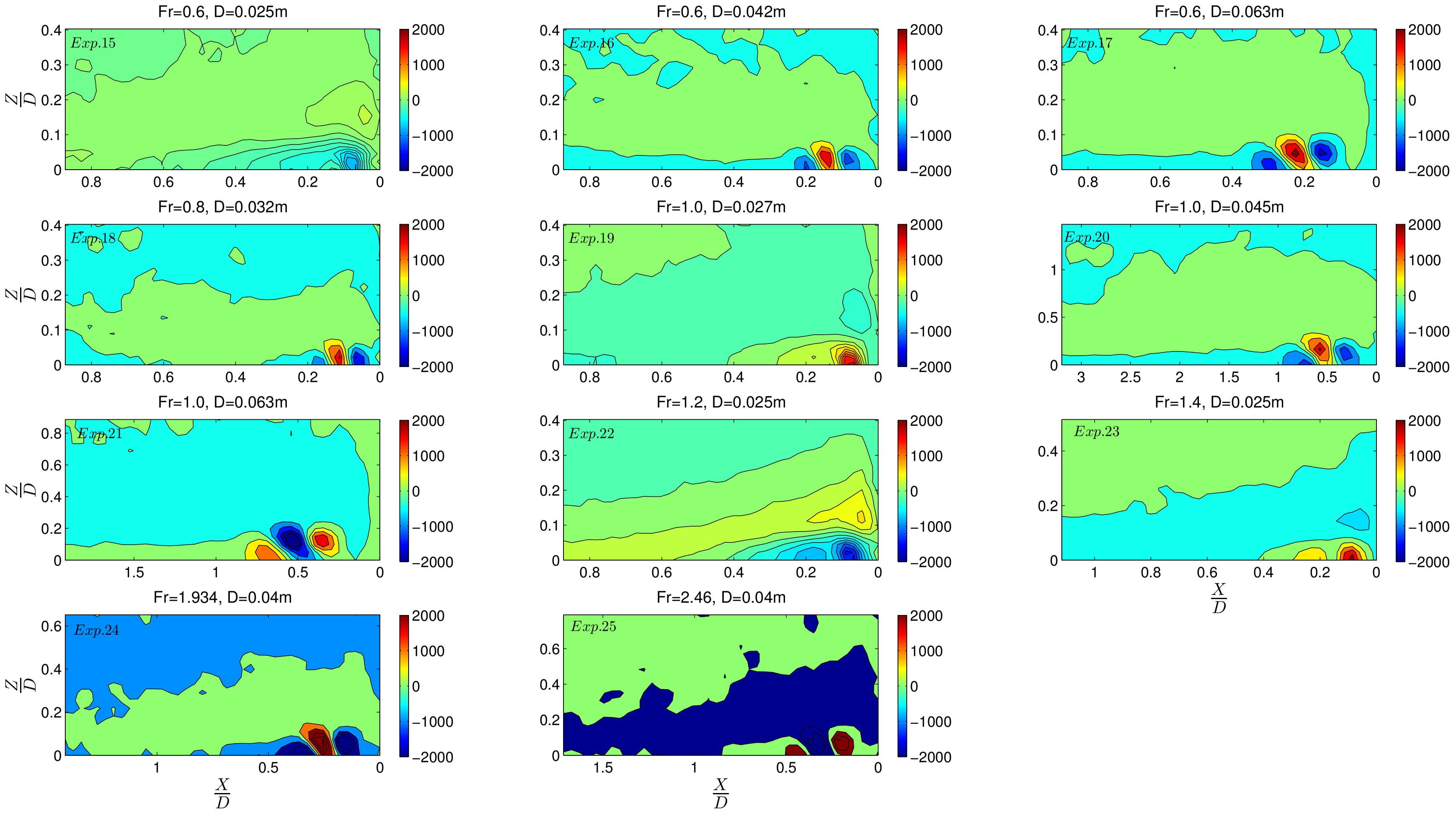

Figure 3.16: Mode 2 from the POD of the vorticity field (units of $s^{-1}$), showing the HV system for experiments 15 to 25 of Table 2.1.

Fr values, where experiments 15-23 grouped in one group with the lowest Fr and experiments 24, and 25 in another group of highest Fr. Froude number changed from 1.4 to 1.936 when a sharp change of the clustering happened, anticipating that more experiments are needed to cover this gap to predict more accurately what is the threshold for the change to occur.

These results show that the single point and whole frame approaches are mainly very similar in terms of grouping the frames into two groups. To find the effect of clustering the frames from a high Fr experiments as a separate group, where the frames mainly clustered into two groups, from comparing these results with the results from clustering the frames in experiments 1-25 in Table 3.11, and it has been found that they are mainly grouped into two groups rather than three and that indicate the independence of the high Fr experiments from the rest of the experiments under the $K$-Means clustering method. This is probably because the direct influence of Fr that affect the geometry of the HV system to a big extend.

Table 3.15: The number of frames from each experiment allocated to the two clusters found from the $K$-Means analysis ($C_{k_1}$ and $C_{k_2}$), as well as the classifier used to define cluster membership for each experiment $(C_{k_1} - C_{k_2})/(C_{k_1} + C_{k_2})$. The two groups of results represent frames chosen using a single point near the bed on the one hand, and using the whole frame points on the other. Results with a strong positive value for $(C_{k_1} - C_{k_2})/(C_{k_1} + C_{k_2})$ are shown in bold. The results are for the case of turbulent stresses distributed by quadrants for experiments of Fr=0.6-2.46.

| | Single Point | | | Whole Frame | | |
|---|---|---|---|---|---|---|
| Experiment | $C_{k_1}$ | $C_{k_2}$ | $\frac{C_{k_1}-C_{k_2}}{C_{k_1}+C_{k_2}}$ | $C_{k_1}$ | $C_{k_2}$ | $\frac{C_{k_1}-C_{k_2}}{C_{k_1}+C_{k_2}}$ |
| 15 | 260 | 0 | **+1.0** | 260 | 0 | **+1.0** |
| 16 | 218 | 0 | **+1.0** | 218 | 0 | **+1.0** |
| 17 | 292 | 0 | **+1.0** | 292 | 0 | **+1.0** |
| 18 | 268 | 0 | **+1.0** | 268 | 0 | **+1.0** |
| 19 | 201 | 0 | **+1.0** | 201 | 0 | **+1.0** |
| 20 | 270 | 0 | **+1.0** | 270 | 0 | **+1.0** |
| 21 | 312 | 0 | **+1.0** | 312 | 0 | **+1.0** |
| 22 | 316 | 0 | **+1.0** | 316 | 0 | **+1.0** |
| 23 | 234 | 0 | **+1.0** | 234 | 0 | **+1.0** |
| 24 | 62 | 247 | -0.60 | 44 | 265 | -0.72 |
| 25 | 0 | 309 | -1.0 | 0 | 309 | -1.0 |

Figure 3.17 shows the centroids for the extracted clusters, and looking at the left-hand side of the figure, the centroid of cluster 1 has two vortices with higher magnitude of vorticity for the closer to the cylinder. In the second cluster, also two

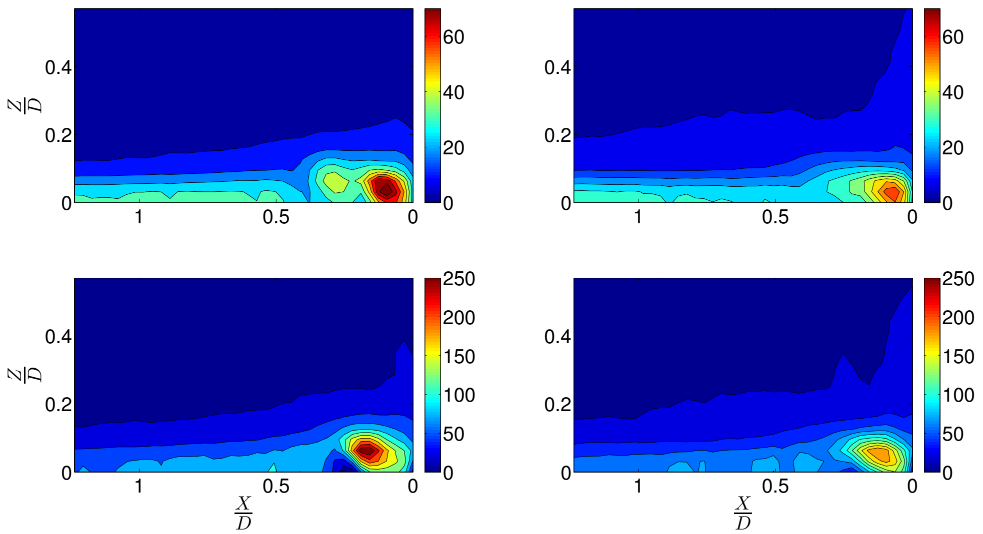

Figure 3.17: The centroids of the clusters extracted from the vorticity fields $\omega$ $(s^{-1})$ over the eleven experiments. Results on the left are for the single point analysis while those on the right are for the whole frame method. Centroid of cluster 1 is shown at the top and of cluster 2 at the bottom in each case. The origin for the horizontal axis is the upstream edge of the cylinder. The results are for the case of turbulent stresses distributed by quadrants for experiments of Fr=0.6-2.46.

vortices are defined, however, the second vortex from the cylinder edge is located under the bigger vortex located near the cylinder. To understand the geometry of the HV system it is needed to compare the clustering centroids of the high stress state frames for a group of high Fr with the whole group of experiments. For a fair comparison, centroids 1 and 2 from Figure 3.17 are compared with centroids 2 and 3 of Figure 3.14 respectively. It is shown from the two figures that the centroids are similar and this confirm that there is a physical interpretation which leads to the clustering of particular frames together in each time.

## 3.5 Summation of Turbulent Stresses of Quadrants 1, 3, and 4 in front of the Cylinder

This section was undertaken to determine controls on the behaviour of the other quadrants (1, 3, and 4) that are non-dominant in terms of peak stress exerted. The procedures are similar to Section 3.3 apart from that the effect of quadrant 2 is not taken into account. This time the peak stress for each experiment was calculated from the measured turbulent stresses in quadrants 1, 3, and 4. The basic data underpinning the analysis of this section is shown in Table 3.16. Figures 3.18, 3.19, and 3.20 show the values of $\eta$, $\eta/U^2$, and $\zeta$ respectively. The location and magnitude of each of which used to test the dynamics of the HV system upstream of the cylinder.

### 3.5.1 The Analysis of Sub-critical to Super-critical Froude Numbers

### (Fr $\in \{0.015 - 2.46\}$)

This section includes data from the 25 experiments of this chapter. Table 3.17 shows the results of the stepwise regression analyses based on the data of Tables 2.1 and 3.16 and they show that two parameters are in control of the location of the maximum means of the absolute stresses when the distance is measured in $mm$. These parameters are $D$ and $\mathrm{Re}_D$. These results are similar to the equivalent cases in Sections 3.3 and 3.4, which is a confirmation about the robustness of the results. From the results of the magnitude of the controlling parameters, there is a clear effect of $h$ on the three quantities, $\eta$, $\eta/U^2$, and $\eta/\zeta$. This effect of $h$ is either direct or indirect through the other parameters, Fr and $\mathrm{Re}_h$. These results are very similar to the ones in Section 3.3 and that gives indication that maybe the effect of quadrant 2 is not important for the prediction of the magnitude of stresses for near-bed locations under the HV system. The two plots in Fig. 3.21 show the effect of Fr and $h$ on the magnitude of the peak stresses. Hence, the trend of change for Fr with $\eta$ is positive, while the trend is negative for the relationship between $\eta/\zeta$, and that is because of the change of $h$ from being in the denominator with Fr to the numerator. In Sections 3.3 and 3.4, analyses the geometry of the HV system using $K$-Means clustering algorithm were adopted. The patterns found in those sections were same as those for quadrants 1, 3, and 4 and are not replicated here.

Table 3.16: Dependent variables used in the stepwise regression of the ($Q_1$+$Q_3$+$Q_4$) turbulent stresses for experiments of Fr=0.015-2.46. The predictor variables are given in Table 2.1.

| Exp. No. | $x_{max}$ for $\eta$, $\eta/U^2$, and $(\eta/\zeta)$ $(mm)$ | $x_{max}/D$ for $\eta$, $\eta/U^2$, and $\eta/\zeta$ | $\eta_{max}$ $(\times 10^{-4} m^2 s^{-2})$ | $(\eta/U^2)_{max}$ | $(\eta/\zeta)_{max}$ (%) |
|---|---|---|---|---|---|
| 1 | 3.69 | 0.067 | 0.0181 | 18.84 | 3.82 |
| 2 | 3.69 | 0.067 | 0.0318 | 22.05 | 4.70 |
| 3 | 7.39 | 0.134 | 0.0613 | 24.53 | 4.39 |
| 4 | 11.08 | 0.201 | 0.1067 | 29.65 | 5.19 |
| 5 | 7.39 | 0.134 | 0.1577 | 32.18 | 5.47 |
| 6 | 3.69 | 0.246 | 0.1429 | 8.46 | 5.05 |
| 7 | 4.92 | 0.197 | 0.2066 | 12.22 | 6.54 |
| 8 | 8.62 | 0.157 | 0.3332 | 19.72 | 7.54 |
| 9 | 6.15 | 0.143 | 0.6769 | 24.55 | 7.55 |
| 10 | 4.92 | 0.145 | 1.1542 | 26.17 | 7.93 |
| 11 | 3.69 | 0.132 | 1.1542 | 17.72 | 7.26 |
| 12 | 3.69 | 0.148 | 2.6649 | 20.45 | 6.71 |
| 13 | 6.15 | 0.147 | 5.3922 | 41.38 | 8.60 |
| 14 | 9.85 | 0.179 | 6.5085 | 49.94 | 8.72 |
| 15 | 3.69 | 0.148 | 5.8431 | 25.79 | 8.92 |
| 16 | 7.39 | 0.176 | 9.7619 | 43.08 | 9.35 |
| 17 | 11.08 | 0.176 | 10.6804 | 47.14 | 8.39 |
| 18 | 4.92 | 0.154 | 13.0726 | 31.82 | 10.02 |
| 19 | 3.69 | 0.137 | 12.6618 | 22.51 | 9.23 |
| 20 | 7.39 | 0.164 | 9.4970 | 16.88 | 8.03 |
| 21 | 11.08 | 0.176 | 10.2748 | 18.27 | 7.07 |
| 22 | 3.69 | 0.145 | 18.2619 | 25.88 | 8.59 |
| 23 | 4.92 | 0.197 | 23.0062 | 31.62 | 9.30 |
| 24 | 8.62 | 0.215 | 72.7998 | 36.77 | 9.60 |
| 25 | 8.62 | 0.215 | 138.3686 | 50.70 | 8.51 |

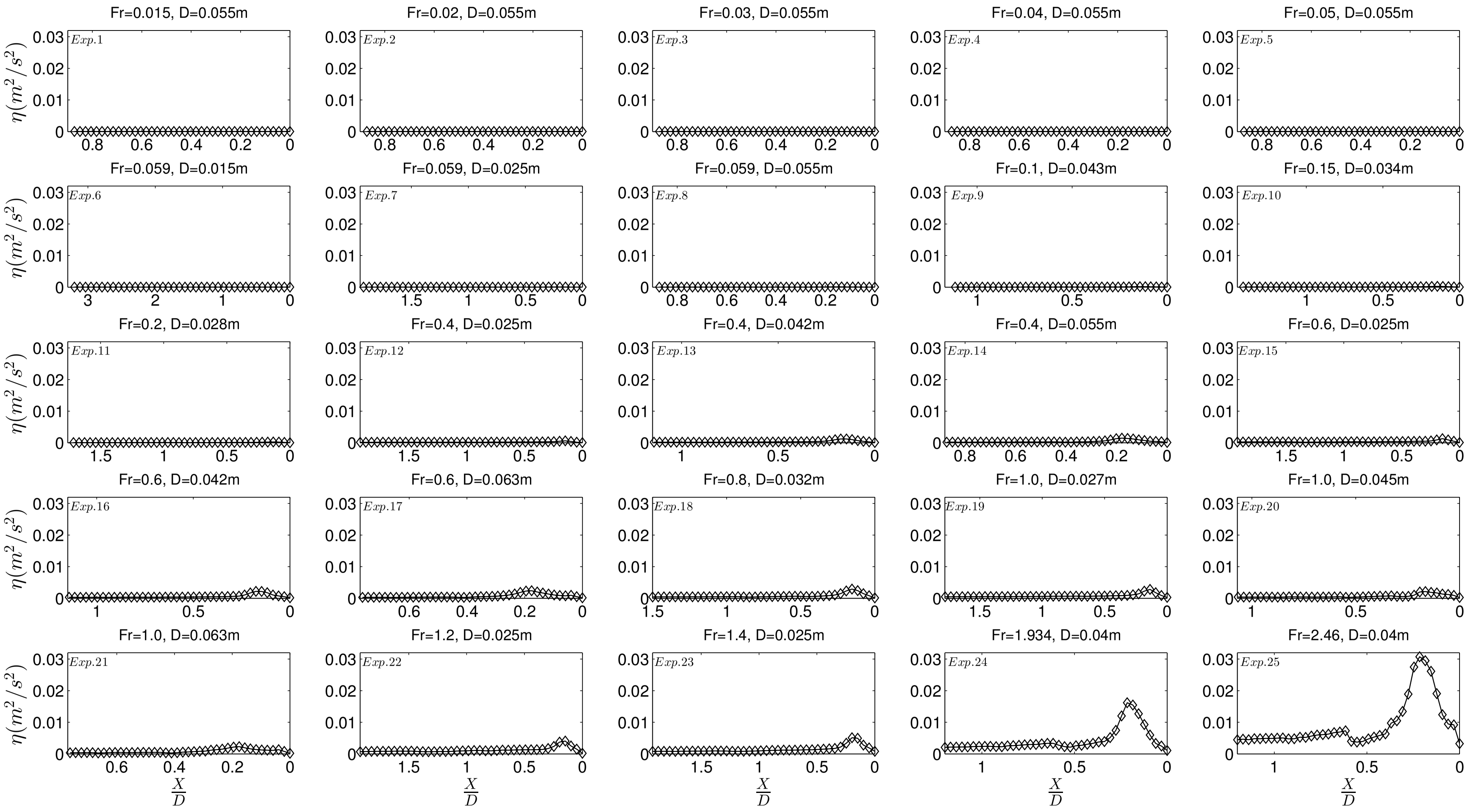

Figure 3.18: Mean of absolute velocity covariances for the summation of ($Q_1$, $Q_3$, and $Q_4$) $\eta$. The abscissa indicates distance upstream from the upstream edge of the cylinder. Fr=0.015-2.46.

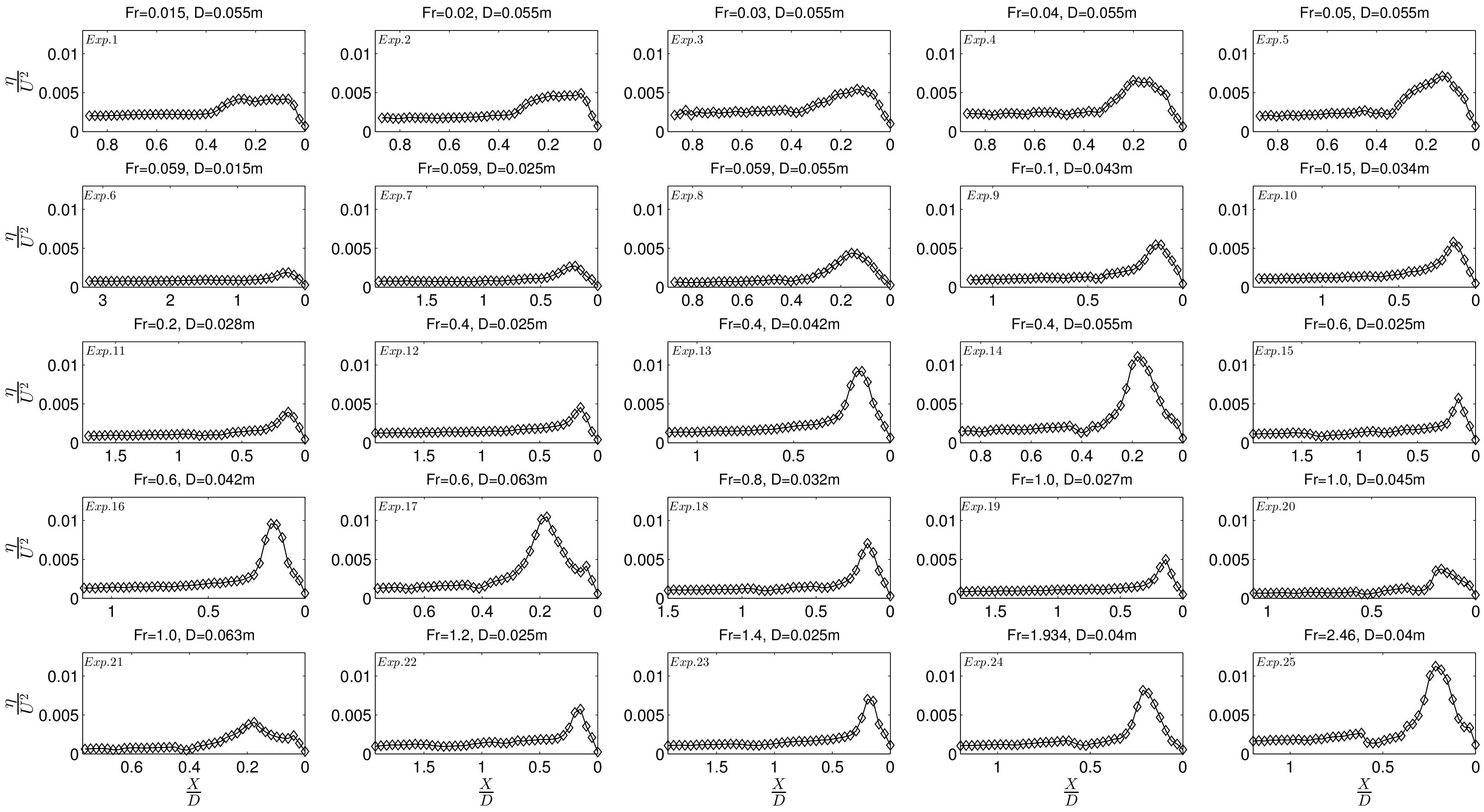

Figure 3.19: Mean of absolute velocity covariances normalized by the square of the approaching bulk flow velocity $\frac{\eta}{U^2}$. The abscissa indicates distance upstream from the upstream edge of the cylinder. Fr=0.015-2.46.

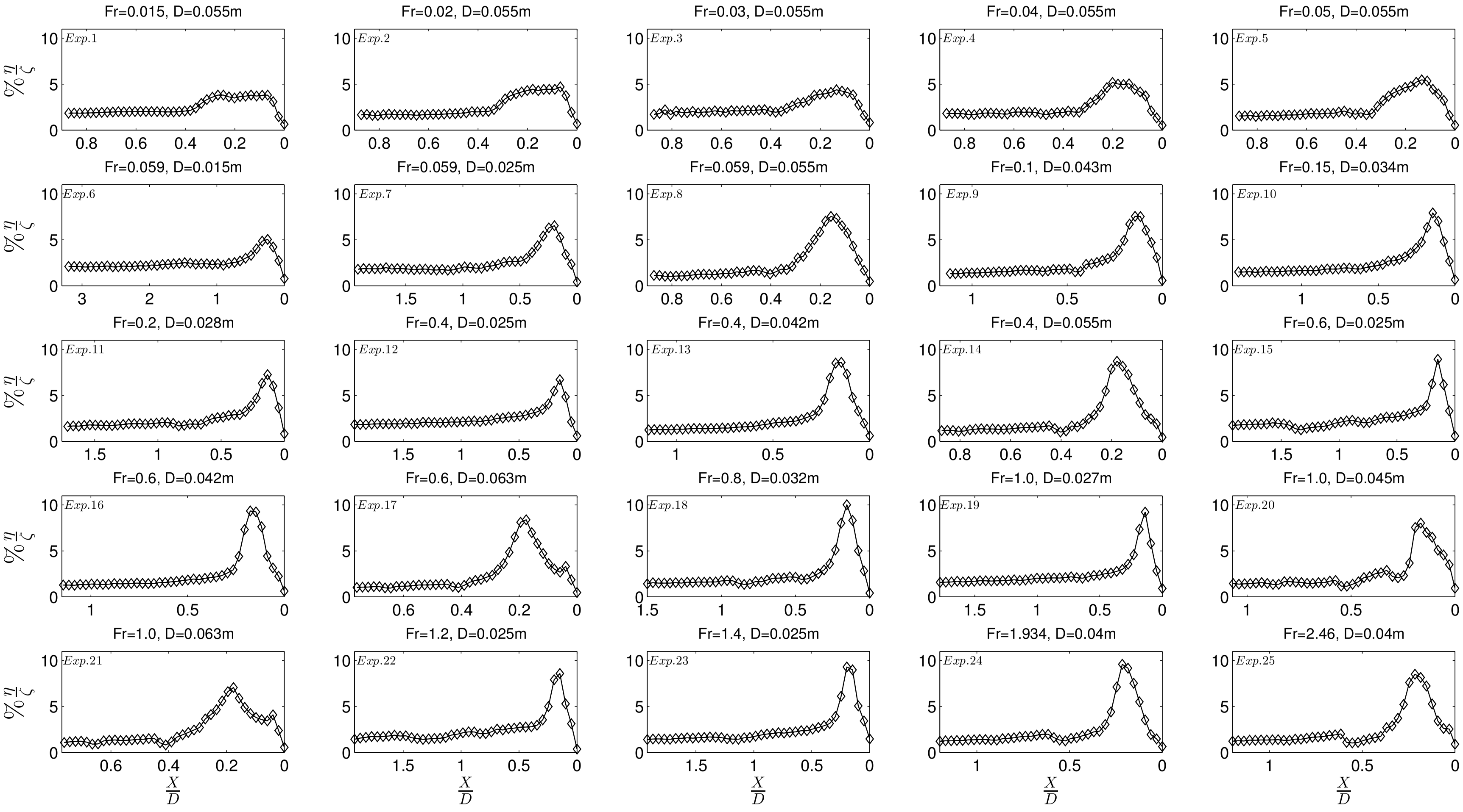

Figure 3.20: Mean of absolute velocity covariances normalized by the summation of the means of absolute velocity covariances over all forty positions $\frac{\eta}{\zeta}$. The abscissa indicates distance upstream from the upstream edge of the cylinder. Fr=0.015-2.46.

Table 3.17: The predictor variables contributing significantly to a stepwise regression equation for the selected response variables, together with their significance levels and the $R^2$ associated with the regression equation for the summation of turbulent stresses of quadrants 1, 3, and 4 for experiments of Fr=0.015-2.46.

| Regression | $R^2$ | Pred. 1 | $p$-value | Pred. 2 | $p$-value |
|---|---|---|---|---|---|
| $x_{max}(\eta, \eta/U^2, \eta/\zeta)$ $(mm)$ | 0.758 | $D$ | $< 0.001$ | Re$_D$ | 0.0039 |
| $x_{max}(\eta, \eta/U^2, \eta/\zeta)$ $(\frac{x_{max}}{D})$ | 0.617 | $Q$ | 0.0011 | - | - |
| $\eta_{max}$ | 0.846 | Fr | $< 0.001$ | $h$ | 0.0086 |
| $(\eta/U^2)_{max}$ | 0.650 | $h$ | $< 0.001$ | $D$ | 0.0314 |
| $(\eta/\zeta)_{max}$ | 0.835 | $h$ | $< 0.001$ | Re$_h$ | $< 0.001$ |

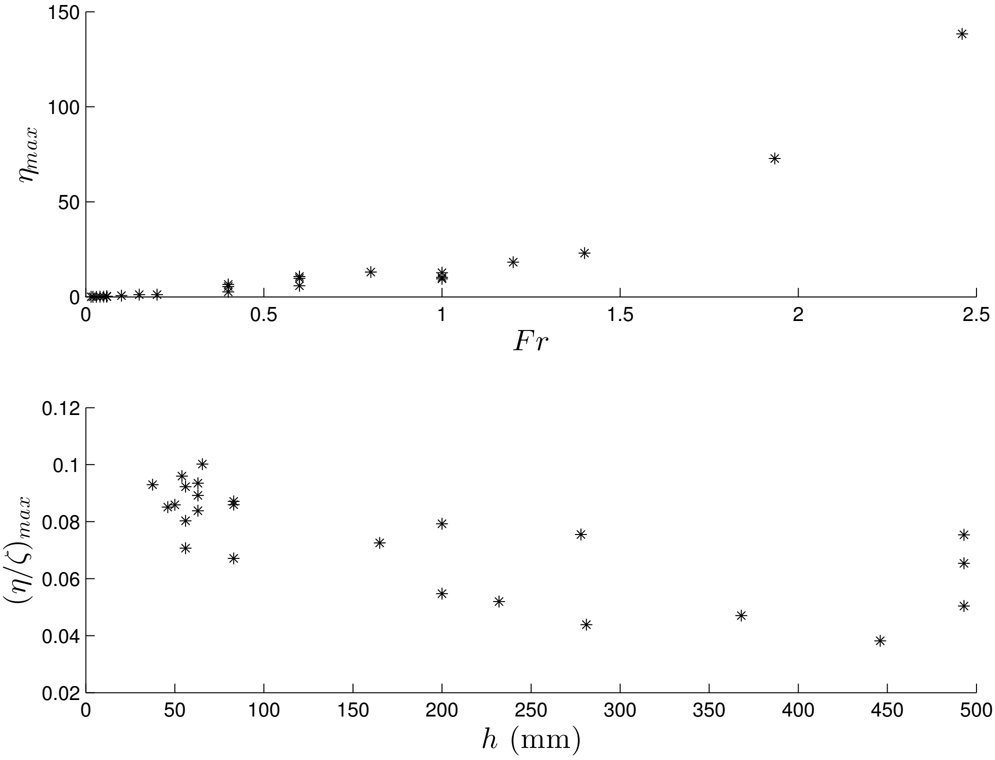

Figure 3.21: The relationship between the peak stresses magnitude with the Froude number and flow depth for the top and bottom plots, respectively.

### 3.5.2 The Analysis of Lower Sub-critical Froude Numbers (Fr $\in \{0.015 - 0.2\}$)

These analyses have been done to find the effect of the controlling parameters of the stresses of quadrants 1,3, and 4 on the HV dynamics for 11 experiments from the lower part of Fr values included in this study. The stepwise results in Table 3.18 revealed no control on the location of the peaks, and this is the first time the cylinder diameter is absent as a control on peak location. Obviously the removal of quadrant 2 from the stresses caused to this result. Froude number stands out as a main controlling parameter of the variable $\eta$ as in Section 3.5.1 but this time as a sole parameter. At the same time, parameters $h$ and $D$ for $\eta/U^2$ remained the same. For $\eta/\zeta$ both Reynolds numbers are controlling its magnitude, and that is very consistent with the results for $\gamma/\beta$ of the equivalent section shown in Table 3.5.

Table 3.18: The predictor variables contributing significantly to a stepwise regression equation for the selected response variables, together with their significance levels and the $R^2$ associated with the regression equation for the summation of turbulent stresses of quadrants 1, 3, and 4 for experiments of Fr=0.015-0.2.

| Regression | $R^2$ | Pred. 1 | $p$-value | Pred. 2 | $p$-value |
|---|---|---|---|---|---|
| $x_{max}(\eta, \eta/U^2, \eta/\zeta)$ $(mm)$ | - | - | - | - | - |
| $x_{max}(\eta, \eta/U^2, \eta/\zeta)$ $(\frac{x_{max}}{D})$ | - | - | - | - | - |
| $\eta_{max}$ | 0.942 | Fr | $< 0.001$ | - | - |
| $(\eta/U^2)_{max}$ | 0.894 | $h$ | 0.0010 | $D$ | 0.0012 |
| $(\eta/\zeta)_{max}$ | 0.945 | Re$_D$ | $< 0.001$ | Re$_h$ | 0.0130 |

### 3.5.3 The Analysis of Upper Sub-critical to Supper-critical Froude Numbers (Fr $\in \{0.6 - 2.46\}$)

Table 3.19 shows the variables that control the location and magnitude of the predictor variables of a group of 11 experiments of the upper end of our 25 experiments. The cylinder diameter and Froude number are having a combined control on the location of peak values of $\eta$, $\eta/U^2$, and $\eta/\zeta$ when the distances are in $mm$. The results of the controlling parameters for this case are consistent with the results of Section 3.3.3.1 when the effect of quadrant 2 was considered. The effect of $U$ was removed when $\eta$ was normalised by $U^2$. The only difference is that $D$ effect existed when $\eta$ normalised by $\zeta$ and that is attributed to the effect of the normalisation by the summation of the stresses in all the near-bed 40 points included in the calculations.

## 3.6 Discussion

This research has been done in a different way from the previous research that studied the HV behaviour (Baker, 1979, 1980; Dargahi, 1989; Sahin et al., 2007). It

Table 3.19: The predictor variables contributing significantly to a stepwise regression equation for the selected response variables, together with their significance levels and the $R^2$ associated with the regression equation for the summation of turbulent stresses of quadrants 1, 3, and 4 for experiments of Fr=0.6-2.46.

| Regression | $R^2$ | Pred. 1 | $p$-value | Pred. 2 | $p$-value |
|---|---|---|---|---|---|
| $x_{max}(\eta, \eta/U^2, \eta/\zeta)$ $(mm)$ | 0.975 | $D$ | $< 0.001$ | Fr | 0.0015 |
| $x_{max}(\eta, \eta/U^2, \eta/\zeta)$ $(\frac{x_{max}}{D})$ | 0.716 | Re$_D$ | 0.0050 | - | - |
| $\eta_{max}$ | 0.885 | $U$ | $< 0.001$ | - | - |
| $(\eta/U^2)_{max}$ | - | - | - | - | - |
| $(\eta/\zeta)_{max}$ | 0.626 | $D$ | 0.0363 | - | - |

included different experiments with a wide range of flow conditions that focused on separating the effect of the controlling parameters shown in Table 1.1. The three different criteria used in choosing the peak stress values provide a refined view of how near-bed stresses are manifest. There were very consistent results of the parameters that control the geometry of the HV system for the three criteria in Sections, 3.3.1.2, 3.4.1.2, and 3.5.1, although the results were not shown in the latter section to avoid replication. In addition, the results were also consistent when the whole group of experiments were divided in the analyses into low sub-critical and super-critical groups. For the dynamics of the HV, there was also a good match of the results across the three different approaches, especially for the parameter that control the location of the peak stresses, and that is because of its relevance to the geometry of the HV system that showed a very good agreement among the different approaches. The controls of the magnitude of the peaks showed similarity. These similarities were obvious between Sections 3.3.1.1, and 3.5.1, and for Sections 3.3.2.1, 3.5.2, and between Sections 3.3.3.1, and 3.5.3, these similarities are showing the importance of quadrant 2 as a criterion in selection of the peak stress values.

# Chapter 4

# Results: HV Behaviour for Sub-critical Froude Numbers

Given the results for the 25 experiments in Chapter 3, a refined experimental design was adopted in an attempt to establish the controls on the HV system in a clearer fashion for sub-critical Froude numbers for nine experiments. As with Chapter 3, the three peak values of the mean of absolute stresses, quadrant-based analyses, and the summation of quadrants 1, 3, and 4 were undertaken.

The structure of this chapter consists of two main sections. A brief introduction is given in Section 4.1, and the results are presented in Section 4.2. Analysis follows the framework established in Chapter 3.

## 4.1 Introduction

The flow conditions for the experiments in this chapter were mainly driven by the Froude numbers used in many previous studies conducted to study the flow upstream of the cylinders, e.g. Roulund et al. (2005), Paik et al. (2010), and Escauriaza and Sotiropoulos (2011). These Froude numbers are in the lower part of the sub-critical regime.

As before, a set of forty points ($Ns$=40) were chosen near-bed under the system and just upstream to the HV. All of the points were at the same elevation from the bed and just at 1.23 $mm$ from the bed that enabled the study of the wall turbulent stresses. For each of the approaches, a stepwise regression method was used to find out the flow parameters that control selected criteria of the HV system. Later on, a hole size have been defined to separate the most effective vorticity fields among the total number captured in each experiment based on the maximum value of the mean absolute turbulent stresses of a single point. This single point representation was deemed to represent the near wall stresses well, but the full frames were also analysed. Finally, a $K$-Means technique was used to cluster the properties of the frames in a given experiment.

## 4.2 Selected Flow Conditions with Sub-critical Froude Numbers (Fr=0.2, 0.35, and 0.5)

These experiments were designed in such a way to explore in much more details the flow conditions of the HV system for sub-critical Froude numbers. The dynamics and geometry of the HV system were the characteristics studied through the near-bed turbulent stresses in the region upstream to the cylinder. Table 2.2, which listed the characteristics of these experiments is reproduced here for convenience. See Section 2.3.2 for further information concerning the experimental design.

### 4.2.1 Turbulent Stresses in front of the Cylinder

In this section the value of the turbulent stress contribution is considered for the analysis, where the mean of the absolute turbulent stresses at each point was chosen as a criterion for the HV system and the point that attained the maximum value was selected to represent the whole group of 40 points near the wall upstream of the cylinder. The results of the velocity covariance from near-wall locations for the turbulent stresses are shown in Figs. 4.1, 4.2 and 4.3. The abscissa for the forty points shown, is the distance from the upstream edge of the cylinder. Figure 4.1 shows that magnitude of $\gamma$ increased for all of the three groups of experiments in top, middle, and bottom rows of plots when the Froude number increased. However, the location of the peak relative to the cylinder's edge is shown to be driven by cylinder diameter within each group, for experiments of similar Fr represented by the plots in columns.

For column 1, it is shown that the peak point moved towards the cylinder's edge when cylinder diameter decreased from 0.06 $m$ to 0.045 $m$, and then it moved away when the diameter increased to $D = 0.07\ m$. In case of column 2, the peak moved towards the cylinder when the diameter decreased from 0.06 $m$ to 0.04 $m$. The trend is similar in column 3 when $D$ decreased from 0.06 $m$ to 0.028 $m$. These results indicate a clear correlation with $D$. Also, it is shown for group 1 and 2 of the experiments, shown in table 4.1, represented by top and middle rows of plots, shown in Fig. 4.1 that the peak location of $\gamma$ is moving away from the cylinder as Fr increased from 0.2 to 0.5, knowing that in these two cases, the diameter of each group is constant. The three experiments in the bottom line are not following the same trend of the other groups and that could be attributed to the decrease in cylinder diameter. Figure 4.2 shows $\gamma$ normalised by the square of the approaching bulk flow velocity $U^2$, and Fig. 4.3 is showing the relative contribution of $|u'w'|$ to the summation of all 40 sites $\gamma/\beta$.

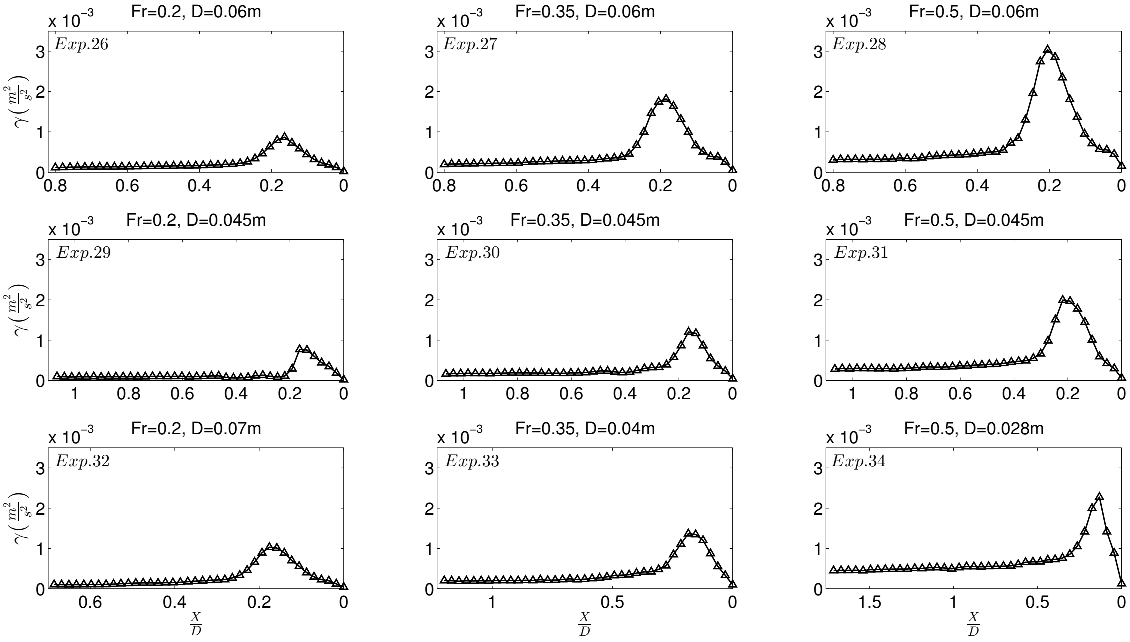

Figure 4.1: Mean of absolute velocity covariances $\gamma$. The abscissa indicates distance upstream from the upstream edge of the cylinder. Fr=0.2-0.5.

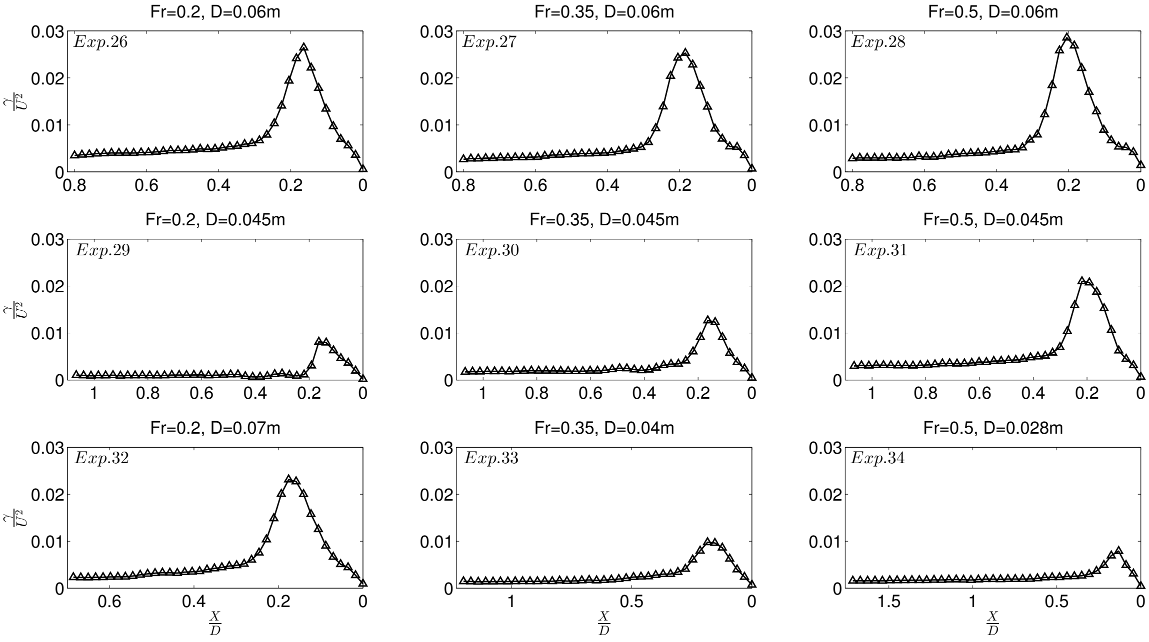

Figure 4.2: Mean of absolute velocity covariances normalized by the square of the approaching bulk flow velocity $\frac{\gamma}{U^2}$. The abscissa indicates distance upstream from the upstream edge of the cylinder. Fr=0.2-0.5.

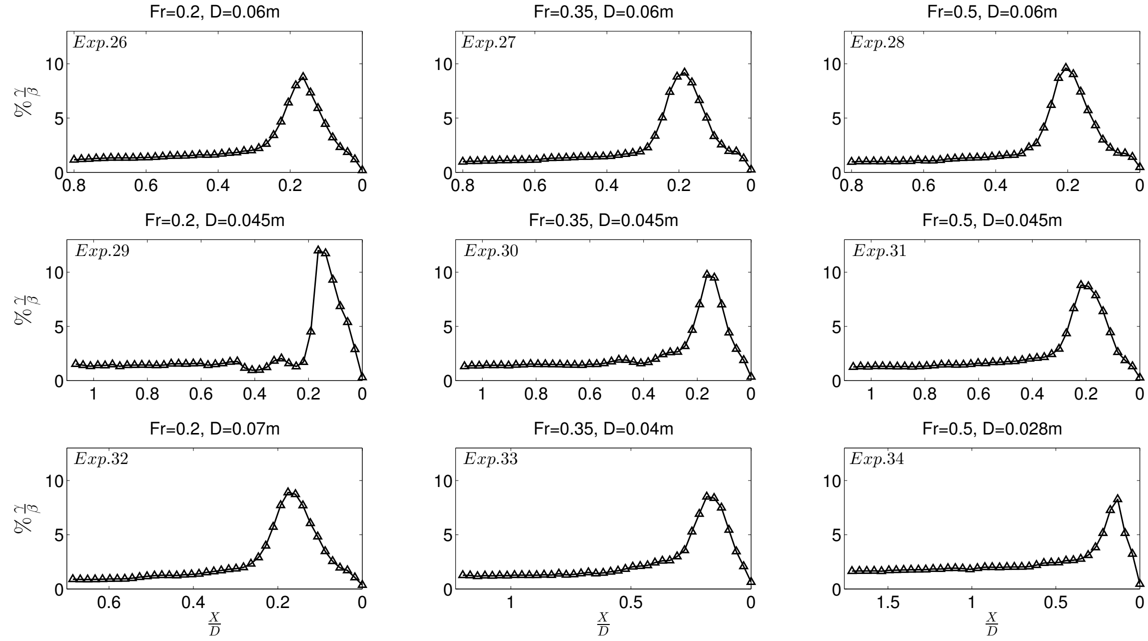

Figure 4.3: Mean of absolute velocity covariances normalized by the summation of the means of absolute velocity covariances over all forty positions $\frac{\gamma}{\beta}$. The abscissa indicates distance upstream from the upstream edge of the cylinder. Fr=0.2-0.5.

There is small increase in $\gamma$, $\gamma/U^2$, and $\gamma/\beta$ in Figures 4.1, 4.2 and 4.3 respectively for the upstream control locations when moving from the furthest point towards the cylinder up to the point where a significant change in elevation happens and that is due to the further upstream effect of the HV system. However, the difference between the values is very small for the majority of these points when related to one experiment. Figures 4.1, 4.2 and 4.3 show that the mean of these values is approximately 2-7 times lower than the peaks experienced in the HV region, demonstrating the significance of the vortex system for near-wall stresses generation (Devenport and Simpson, 1990). The peak of the mean absolute stresses and its location were the primary dependent variables used in the stepwise regression analysis (Table 4.1). The location of the peak is identical for $\gamma$, $\gamma/U^2$, and $\gamma/\beta$. The following section presents the results of the analysis.

Table 4.1: Dependent variables used in the stepwise regression for the turbulent stresses. The predictor variables are given in Table 2.2.

| Exp. No. | $x_{max}$ for $\gamma$, $\gamma/U^2$, and $(\gamma/\beta)$ $(mm)$ | $x_{max}/D$ for $\gamma$, $\gamma/U^2$, and $\%(\gamma/\beta)$ | $\gamma_{max}$ $(\times 10^{-4} m^2 s^{-2})$ | $(\gamma/U^2)_{max}$ | $\gamma/\beta_{max}$ (%) |
|---|---|---|---|---|---|
| 26 | 9.9 | 0.164 | 3.90 | 119.05 | 8.77 |
| 27 | 11.1 | 0.185 | 8.17 | 113.75 | 9.18 |
| 28 | 12.3 | 0.205 | 13.67 | 128.63 | 9.61 |
| 29 | 7.4 | 0.164 | 3.47 | 36.58 | 11.99 |
| 30 | 7.4 | 0.164 | 5.41 | 57.03 | 9.76 |
| 31 | 9.9 | 0.219 | 8.97 | 94.56 | 8.80 |
| 32 | 12.3 | 0.176 | 4.64 | 100.18 | 8.90 |
| 33 | 7.4 | 0.185 | 6.15 | 43.97 | 8.50 |
| 34 | 3.7 | 0.132 | 10.24 | 35.51 | 8.27 |

#### 4.2.1.1 Stepwise regression analysis of the turbulent stresses

The stepwise regression analysis results are stated in Table 4.2. They show both $D$ and Fr played a role in the prediction of the maximum mean absolute stresses location, measured in millimetres, shown in Figures 4.1, 4.2 and 4.3, with no control parameter when the distance $X$ was normalised by cylinder diameter, $\frac{X}{D}$. The peak values of $\gamma$ were controlled by a combination of Fr and $D$, while $\gamma/U^2$ is controlled by $\mathrm{Re}_h$ and $D$. For both of these cases the effect of the bulk momentum $(U \cdot h)$ has been found when Fr is replaced by $\mathrm{Re}_h$. Hence, $\mathrm{Re}_h$, is a significant control on near-wall structure. No variable is shown to control $\gamma/\beta$.

Tables 2.2, 4.1 and 4.2 show how Fr and $D$ control the location of the mean absolute peak stresses, however the effect of $D$ is much more than that of Fr and that is shown from the magnitude of $p$-value. This is because $D$ is constant for the experiments in group 1 and then again for group 2, so that the increasing distance that the peak mean absolute stresses is located from the cylinder highlights the Froude number control as one moves towards the upper end of sub-critical, the HV system moves upstream. However, the degree of variation in each of groups 1 and 2 is less than that between the groups because of the dominant effect of $D$, which is clearly seen in group 3. Hence, the Froude number effect is secondary to the diameter's control upon lateral momentum flux into the region, which acts to displace the HV system away from the cylinder. This is confirmed in the regression analysis and it is shown in Fig. 4.4, that shows the second mode from the POD of the vorticity fields for the same group of nine experiments and highlights that the basic geometry of the HV system is similar for the different experiments (except experiment 34 where the relatively small $D$ makes the whole system very small to be seen clearly). From this, we know that the effect of $D$ and Fr is the thing that cause of displacement when additional momentum is pumped into the region, more than altering the vortex system topology.

It is shown in this section of results that the overall control parameters are not matching with any of the results of the three groups of analyses shown in Tables 3.2, 3.5, and 3.7 in Chapter 3. Although, $D$ is a shared control parameter among all cases which showed always a significant effect on controlling the location of the maximum mean of stresses when distances measured in $mm$. This is shown in the top plot of Fig. 4.5 with a very clear relationship between the cylinder diameter and the location of the peak stress. These results recognise the cylinder diameter as a main parameter that controls the point that it has the maximum bed turbulent stresses, hence the expected location of the maximum depth of scour hole upstream of the cylinder. Regarding the stresses magnitude control, there is a clear effect of Fr in controlling the value of $\gamma$ between the analyses of this section, shown in bottom plot of Fig. 4.5 and the ones in Tables 3.2 and 3.5. With these findings, Fr control on the turbulent stresses is found to be more effective for the lower part of sub-critical flow conditions. However, there is a presence of high Froude numbers with the group of the experiments of Table 3.2, yet the effect is still dominated by the experiments with Fr $\leq 0.5$.

Table 4.2: The predictor variables contributing significantly to a stepwise regression equation for the selected response variables, together with their significance levels and the $R^2$ associated with the regression equation for the total turbulent stresses.

| Regression | $R^2$ | Pred. 1 | $p$-value | Pred. 2 | $p$-value |
|---|---|---|---|---|---|
| $x_{max}(\gamma, \gamma/U^2, \gamma/\beta)$ $(mm)$ | 0.943 | $D$ | $< 0.001$ | Fr | 0.0335 |
| $x_{max}(\gamma, \gamma/U^2, \gamma/\beta)$ $(\frac{x_{max}}{D})$ | - | - | – | - | - |
| $\gamma_{max}$ | 0.964 | Fr | 0.0021 | $D$ | 0.0061 |
| $(\gamma/U^2)_{max}$ | 0.886 | Re$_h$ | 0.0278 | D | 0.0434 |
| $(\gamma/\beta)_{max}$ | - | - | - | - | - |

#### 4.2.1.2 The controlling parameter during instances when high turbulent stresses are exerted

The dependence of cylinder diameter for the turbulent stresses was further explored from a consideration of the high stress state frames. More details can be found in paragraphs 2 and 3 in Section 3.3.1.2.

The number of exceedance ($\phi$) for which $H > 2$ and their positions in time were identified for each experiment. These instances were used to extract the frames corresponding to them in time. The percentage of the total number of frames selected ranged from 4.91 to 6.87% over the nine experiments. The summation of the stress magnitudes exceedance at the peak stress locations of the single points contributed from 27.47 to 33.78% of the $\sum |u'w'|$ over all frames of each of the different experiment.

The number of frames in each cluster ($C_{k_1}$ and $C_{k_2}$) was extracted using the $K$-Means classifier and the results are shown in the second to fourth columns of Table 4.3 under the 'Single Point' identifier. It is clear from the results that experiments 26, 27, 28, 31 and 32 may be grouped together with a clear first cluster dominance, although experiment 31 is not strongly belong to the group. Again from the whole frame approach, details of this method are in paragraph 5 of Section 3.3.1.2, two

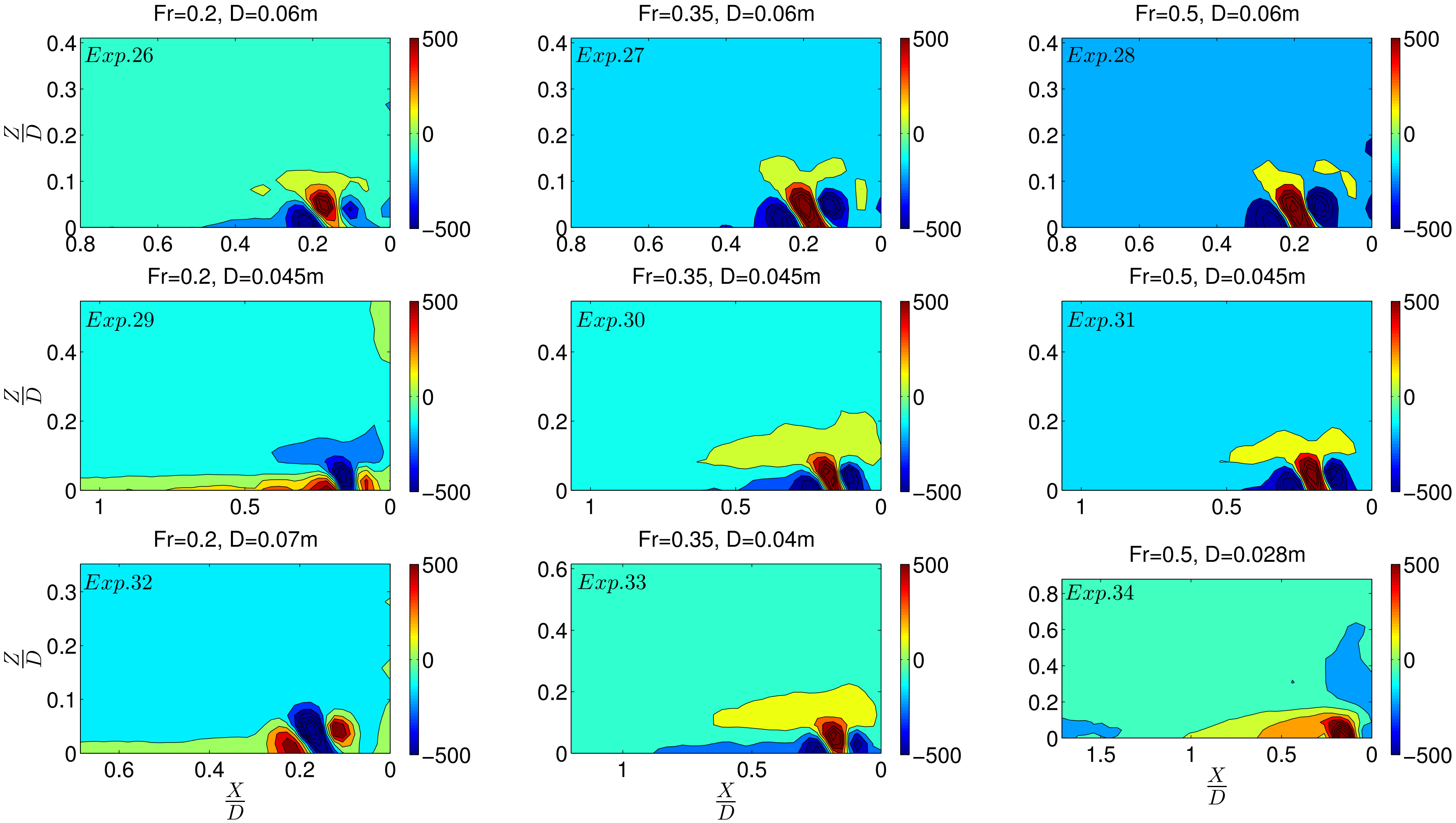

Figure 4.4: Mode 2 from the POD of the vorticity field (units of $s^{-1}$), showing the HV system for the 9 experiments shown in Table 2.2.

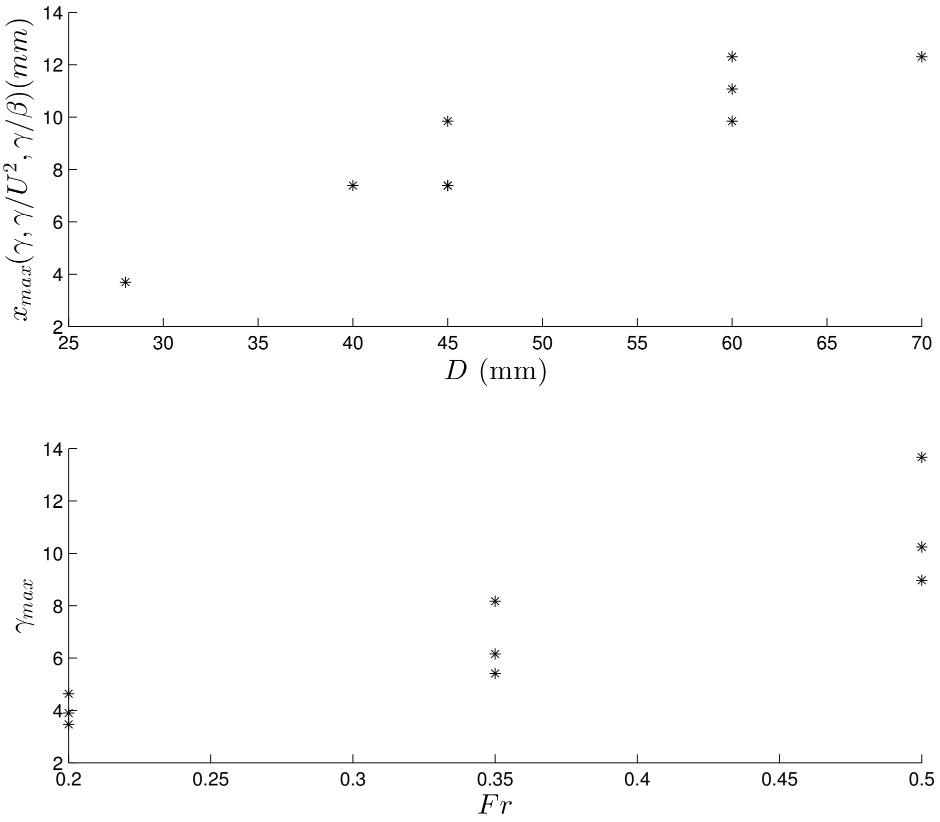

Figure 4.5: The relationship between the peak stress location with the cylinder diameter is shown in the top plot and the relationship between the magnitude of the peak stress and the Froude number is shown in bottom plot.

clear groups were also extracted from the $K$-Means classification of the whole frame fields. The number of frames corresponding to each cluster over the nine experiments is shown in columns 5 to 7 of Table 4.3 under the 'Whole Frame' heading. These results identify experiments 26, 27, 28, and 32 as belonging to one group. Table 2.2 shows that this group of experiments share the biggest cylinder diameters. Hence, although the differences between the single point and whole frame approaches are minor for experiements 26, 27, 28, and 32, it would seem that the cylinder diameter affects the whole HV system to a greater extent than it does the near-bed conditions only. It is the first case that we noticed the dominance of whole frame approach over the single point effect and this attributed to the greater spatial extend of the vortices in the vorticity field that affected by the cylinder diameter.

The right-hand part of Figure 4.6 shows the centroids for clusters $K_1$ and $K_2$ for

Table 4.3: The number of frames from each experiment allocated to the two clusters found from the $K$-Means analysis ($C_{k_1}$ and $C_{k_2}$), as well as the classifier used to define cluster membership for each experiment $(C_{k_1} - C_{k_2})/(C_{k_1} + C_{k_2})$. The two groups of results represent frames chosen using a single point near the bed on the one hand, and using the whole frame points on the other. Results with a strong positive value for $(C_{k_1} - C_{k_2})/(C_{k_1} + C_{k_2})$ are shown in bold.

| | Single Point | | | Whole Frame | | |
|---|---|---|---|---|---|---|
| Experiment | $C_{k_1}$ | $C_{k_2}$ | $\frac{C_{k_1}-C_{k_2}}{C_{k_1}+C_{k_2}}$ | $C_{k_1}$ | $C_{k_2}$ | $\frac{C_{k_1}-C_{k_2}}{C_{k_1}+C_{k_2}}$ |
| 26 | 225 | 84 | **+0.47** | 291 | 18 | **+0.88** |
| 27 | 226 | 58 | **+0.59** | 241 | 43 | **+0.70** |
| 28 | 227 | 62 | **+0.57** | 270 | 19 | **+0.87** |
| 29 | 3 | 239 | -0.98 | 23 | 219 | -0.81 |
| 30 | 36 | 224 | -0.72 | 108 | 152 | -0.17 |
| 31 | 183 | 108 | **+0.26** | 128 | 163 | -0.12 |
| 32 | 261 | 29 | **+0.80** | 274 | 16 | **+0.89** |
| 33 | 22 | 265 | -0.85 | 15 | 272 | -0.90 |
| 34 | 0 | 221 | -1.0 | 1 | 220 | -0.99 |

the whole frame analysis. Therefore, experiments 26, 27, 28 and 32 are identified predominantly with the flow field seen in the top right, which has a more spatially extensive HV system in both the vertical and horizontal plane. The cluster 2 centroid predominantly reflects the results for experiments 29, 30, 31, 33 and 34. In these cases, diameters are smaller and the HV system is more intensive closer to the cylinder and is confined to a narrower vertical extent. Results based on the single point approach exhibit little difference, with a secondary vortex in the top left, showing the general correspondence between near-bed peak stresses and frame-mean peak stress states. From the comparison between these results and the results of the three groups in Chapter 3 in Sections 3.3.1.2, 3.3.2.2, and 3.3.3.2, we found another case of frame clustering based on the cylinder diameter and that is the case when Fr ranged from 0.015-0.2. It is concluded that the cylinder diameter is an important parameter that shapes the geometry of the HV system for the flow conditions that have Fr $\leq 0.5$.

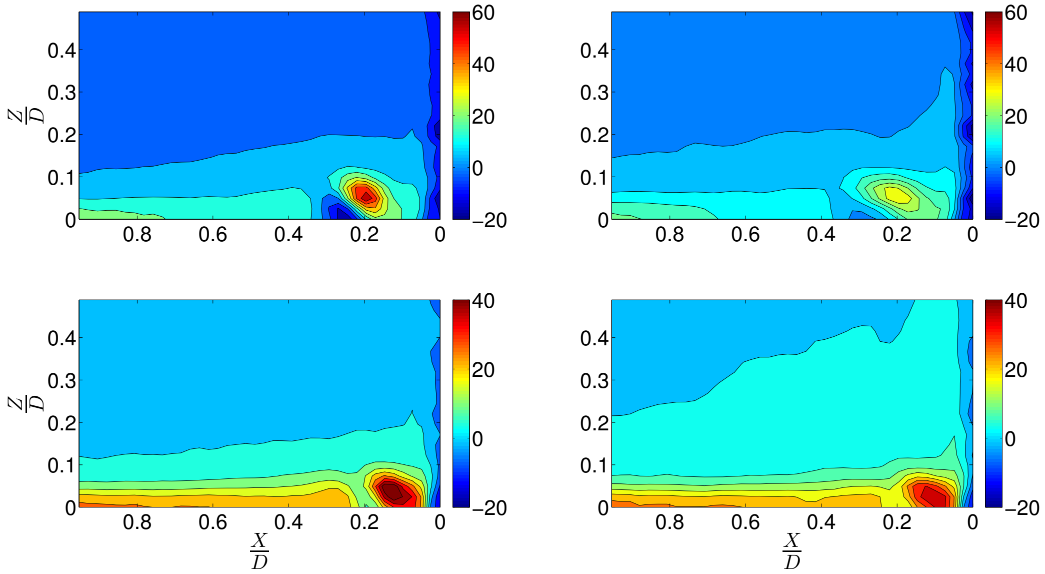

Figure 4.6: The centroids of the clusters extracted from the vorticity fields $\omega$ ($s^{-1}$) over the nine experiments. Results on the left are for the single point analysis while those on the right are for the whole frame method. Centroid of cluster 1 is shown at the top and the centroid of cluster 2 at the bottom in each case. The origin for the horizontal axis is the upstream edge of the cylinder.

### 4.2.2 Turbulent Stresses Contributions in front of the Cylinder Distributed by Quadrants

In this section, the turbulent stresses were separated due to their contribution to different quadrants and, as with the analysis in Chapter 3, quadrant 2 generated the peak stress magnitude and contributed the most to the total stress magnitude. Hence, it was selected as the focus for study. The results for the partitioning of the velocity covariance from the near-wall locations across the four quadrants are shown in Figs. 4.7, 4.8 and 4.9. For all the points with hollow symbols, which are those under and upstream of the HV system, the abscissa is the distance from the upstream edge of the cylinder. Figure 4.7 shows $\alpha$ normalized by the square of the approaching bulk flow velocity $U^2$. Hence, it illustrates the effect of the HV system on turbulence production. The other figures show the relative contribution of $|u'w'|$ as a contribution to all forty sites ($\alpha/\beta$, Fig. 4.8) and for each quadrant on a site-by-site basis ($\alpha/\gamma$, Fig. 4.9).

That there is a small increase in $\alpha/U^2$ in Fig. 4.7 and $\alpha/\beta$ in Fig. 4.8 for the

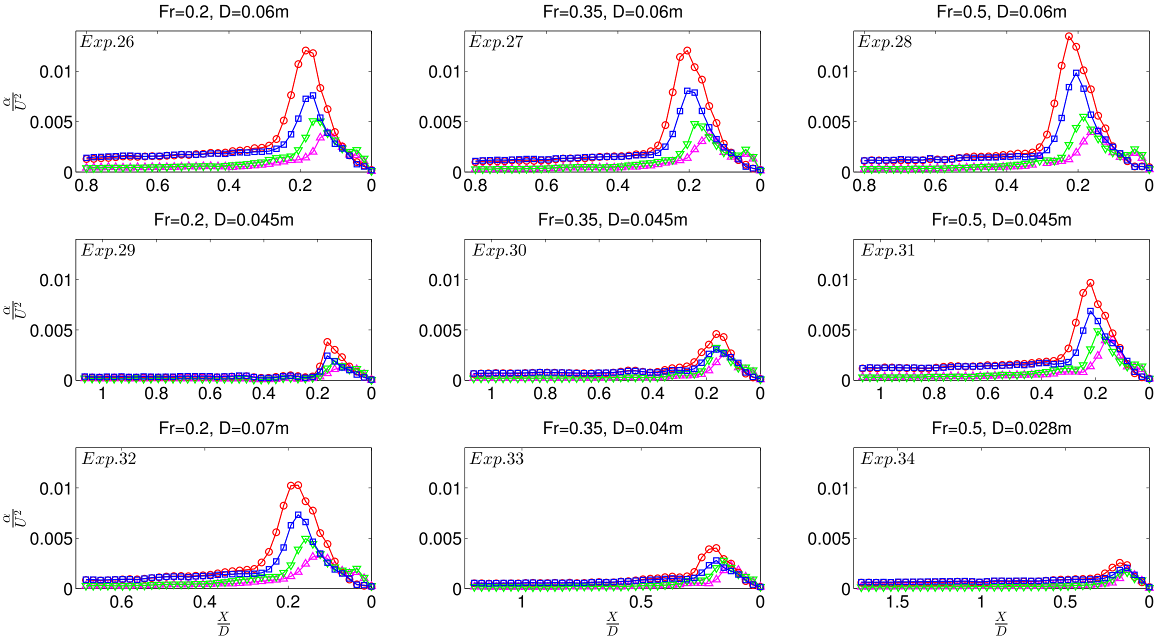

Figure 4.7: Mean of absolute contributions of turbulent stresses of each quadrant normalised by the square of the approaching bulk flow velocity $\frac{\alpha}{U^2}$. The abscissa indicates distance upstream from the upstream edge of the cylinder. As given in Table 2.3, △, ○, ▽, and □ indicate the results for quadrants 1 to 4, respectively. The results are for the case of turbulent stresses distributed by quadrants for experiments of Fr=0.2-0.5.

upstream control locations up to $X/D$=0.45 closer to the cylinder indicates the upstream extent of the effect of the HV system. However, the values are approximately constant for the majority of these points, with similar contributions from quadrants 1 and 3 ($\alpha/U^2 \sim 0.002$, and then for quadrants 2 and 4 ($\alpha/U^2 \sim 0.007$). These values are approximately 2-7 times lower than the peaks experienced in the HV region, highlighting the significance of the vortex system for near-wall stress generation. Note also the spatial structure in the peaks for the maximal contributions from each quadrant, with a consistent order of $Q_1$, $Q_3$, $Q_4$, and then $Q_2$ as one moves away from the cylinder. The quadrant peak absolute stress (which is always for $Q_2$) and its location were the primary dependent variables used in the stepwise regression analysis (Table 4.4). The location of the peak is identical for $\alpha/U^2$ and $\alpha/\beta$, but differs for $\alpha/\gamma$.

While $Q_2$ and $Q_4$ contribute the most to the stresses in the HV system, for approximately $X/D \lesssim 0.1$ closest to the cylinder, this pattern is found to be reversed with

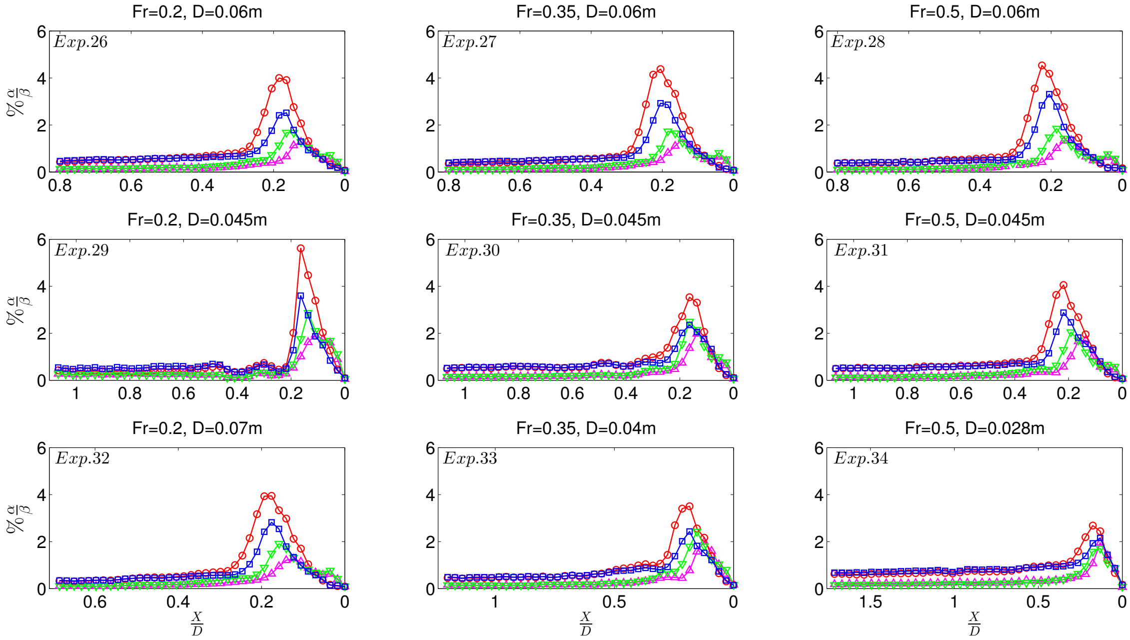

Figure 4.8: Mean of absolute contributions of turbulent stresses of each quadrant normalised by the summation of the means of absolute covariances over all forty positions, $\frac{\alpha}{\beta}$. The abscissa indicates distance upstream from the upstream edge of the cylinder. As given in Table 2.3, △, ◯, ▽, and □ indicate the results for quadrants 1 to 4, respectively. Fr=0.2-0.5.

greater stresses exerted by $Q_1$ and $Q_3$. This result is clearer in Fig. 4.8 and 4.9, with the latter indicating that of the order of 70% of the total velocity covariance is from these quadrants in this region, which is similar to that due to $Q_2$ and $Q_4$ further from the cylinder. The distance to this crossover position both in $mm$ and $X/D$ for $\alpha/\gamma$ was also employed in the regression analysis. These findings came consistant with the results of Section 3.4 were 25 experiments analysed, confirming that is a characteristic behaviour of the HV system upstream of the circular cylinder.

#### 4.2.2.1 Stepwise regression analysis of the turbulent stresses

The results of the stepwise regression analyses are stated in Table 4.5 and while $D$, and Fr played a role in the prediction of the location (the measured distance from the cylinder edge is in $mm$) of the quadrant maximum stress for the following quantities ($D$ and Fr for $\alpha/U^2$ and $\alpha/\beta$, $D$ and $h$ for $\alpha/\gamma$, and $D$ for quadrant cross-over for $\alpha/\gamma$) only $h$ controls the location of the quadrant maximum stress

Table 4.4: Dependent variables used in the stepwise regression. The predictor variables are given in Table 2.2.

| Exp. No. | $x_{max}(\alpha/U^2$ and $\alpha/\beta)$ $(mm)$ | $x_{max}(\alpha/U^2$ and $\alpha/\beta)$ $(\frac{x_{max}}{D})$ | $(\alpha/U^2)_{max}$ | $(\alpha/\beta)_{max}$ (%) | $x_{max}(\alpha/\gamma)$ $(mm)$ | $x_{max}(\alpha/\gamma)$ $(\frac{x_{max}}{D})$ | $(\alpha/\gamma)_{max}$ (%) | Quadrant cross-over for $\alpha/\gamma$ $(mm)$ | Quadrant cross-over for $\alpha/\gamma$ $(\frac{X}{D})$ |
|---|---|---|---|---|---|---|---|---|---|
| 26 | 11.08 | 0.185 | 0.0120 | 4.0 | 12.31 | 0.205 | 55.23 | 4.92 | 0.082 |
| 27 | 12.31 | 0.205 | 0.0121 | 4.4 | 14.77 | 0.246 | 56.90 | 4.92 | 0.082 |
| 28 | 13.54 | 0.226 | 0.0135 | 4.5 | 14.77 | 0.246 | 57.22 | 4.92 | 0.082 |
| 29 | 7.39 | 0.164 | 0.0038 | 5.6 | 7.39 | 0.164 | 46.84 | 3.69 | 0.082 |
| 30 | 7.39 | 0.164 | 0.0046 | 3.5 | 9.85 | 0.219 | 46.12 | 3.69 | 0.082 |
| 31 | 9.85 | 0.219 | 0.0098 | 4.1 | 12.31 | 0.274 | 55.05 | 3.69 | 0.082 |
| 32 | 12.31 | 0.176 | 0.0130 | 4.0 | 14.77 | 0.211 | 55.37 | 4.92 | 0.070 |
| 33 | 7.35 | 0.185 | 0.0040 | 3.5 | 9.85 | 0.246 | 51.06 | 3.69 | 0.092 |
| 34 | 4.92 | 0.176 | 0.0026 | 2.7 | 6.15 | 0.220 | 42.50 | 1.23 | 0.044 |

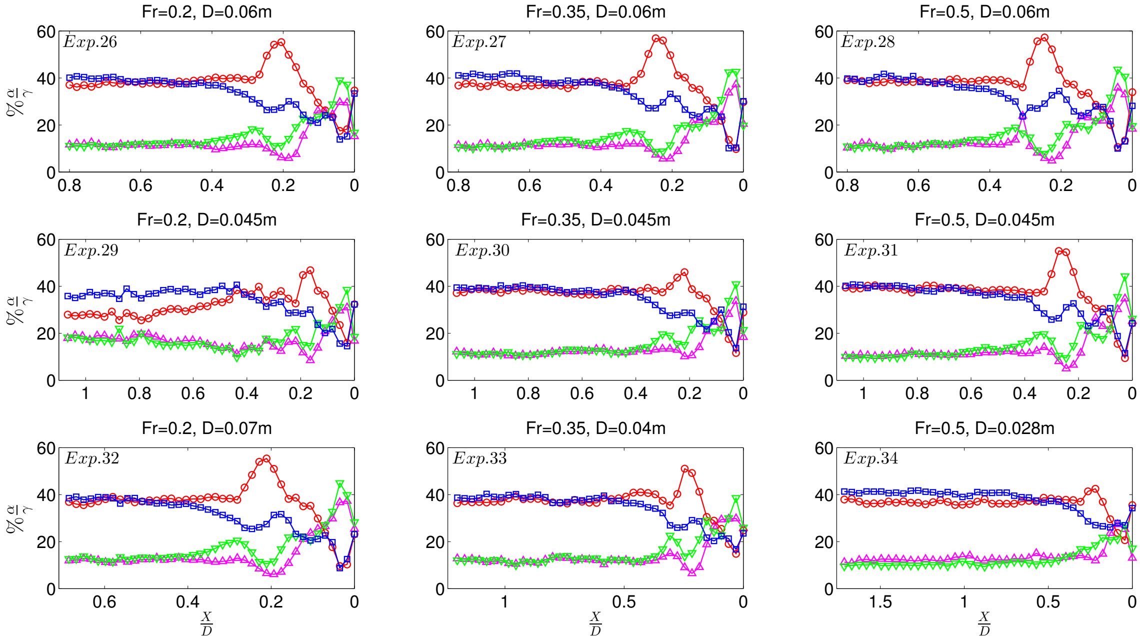

Figure 4.9: Mean of absolute contributions of turbulent stresses of each quadrant normalised by the summation of means of absolute covariance at each position, $\frac{\alpha}{\gamma}$. The abscissa indicates distance upstream from the upstream edge of the cylinder. As given in Table 2.3, $\triangle$, $\bigcirc$, $\bigtriangledown$, and $\square$ indicate the results for quadrants 1 to 4, respectively. Fr=0.2-0.5.

for the same variables when the distance normalised by the cylinder diameter ($h$ for $\alpha/U^2$, $\alpha/\beta$, and $\alpha/\gamma$, and no significant control found for quadrant cross-over for $\alpha/\gamma$) and that is quite understandable when the effect of cylinder diameter is removed from the controlling variables when the distance is normalised by it. The peak stress values were controlled by two variables ($D$ and Fr for $\alpha/U^2$, and $D$ for $\alpha/\gamma$, with no control for $\alpha/\beta$).

An inspection of Table 4.5 shows that the control variables are much more effective at explaining the location of the mean absolute peak stresses when the distance is in *mm* rather than when it is in $X/D$ ($R^2 = 0.967$, 0.947, and 0.869 rather than $R^2 = 0.675$, 0.761 and no significant result), where $R^2$ is the coefficient of determination. Regarding the magnitude of the peak stresses, it is in between of the two cases with $R^2 = 0.886$, and 0.749 for $\alpha/U^2$ and $\alpha/\gamma$ respectively, and no significant result for $\alpha/\beta$. Hence, the basic geometry of the HV system based on distance in *mm* is a strong function of the control parameters, while the dynamic properties are more weakly so. Tables 2.2 and 4.4 clearly show how Fr and $D$

Table 4.5: The predictor variables contributing significantly to a stepwise regression equation for the selected response variables, together with their significance levels and the $R^2$ associated with the regression equation for turbulent stresses contribution distributed by quadrants.

| Regression | $R^2$ | Pred. 1 | $p$-value | Pred. 2 | $p$-value |
|---|---|---|---|---|---|
| $x_{max}(\alpha/U^2$ and $\alpha/\beta)$ $(mm)$ | 0.967 | $D$ | $< 0.001$ | Fr | 0.0037 |
| $x_{max}(\alpha/U^2$ and $\alpha/\beta)$ $(\frac{x_{max}}{D})$ | 0.675 | $h$ | 0.0287 | - | - |
| $(\alpha/U^2)_{max}$ | 0.886 | $D$ | $< 0.001$ | Fr | 0.0278 |
| $(\alpha/\beta)_{max}$ | - | - | - | - | - |
| $x_{max}(\alpha/\gamma)$ $(mm)$ | 0.947 | $D$ | $< 0.001$ | $h$ | 0.0057 |
| $x_{max}(\alpha/\gamma)$ $(\frac{x_{max}}{D})$ | 0.761 | $h$ | 0.0058 | - | - |
| $(\alpha/\gamma)_{max}$ | 0.749 | $D$ | 0.0074 | - | - |
| Quadrant cross-over for $\alpha/\gamma$ $(mm)$ | 0.869 | $D$ | $< 0.001$ | - | - |
| Quadrant cross-over for $\alpha/\gamma$ $(\frac{X}{D})$ | - | - | - | - | - |

interact to control the location of the quadrant peak stresses. The overall results of this section showed a similar results in terms of finding $D$ as a control parameter on the location of the maximum of near-bed stresses (measured in $mm$) and that came along with the results from the previous section in which they match with the results obtained from the analyses of the three groups of experiments in Chapter three. Also, cylinder diameter found to be the shared controlling parameter for the quadrants cross-over when the distance measured in millimetres among this case and the equivalent cases of Chapter 3. Regarding the magnitude of the predicting variables, only few similarities have been found between the results in Table 4.5 and the results in the equivalent Tables 3.10, 3.12, and 3.14. The role of $D$ is very significant in controlling the dynamics of the HV system represented by the magnitude and location of the peak values of the near-bed stresses as is shown in Fig. 4.10.

#### 4.2.2.2 The controlling parameter during instances when high turbulent stresses are exerted

The cylinder diameter dependence for the maximum observed value for $\alpha/\beta$ at a single point, and its position, for the dominant quadrant ($Q_2$) was explored further from a consideration of the high stress state frames, which must dominate the quadrant-dependent values for $|u'w'|$. The frames corresponding to these times were extracted and the percentage of the total number of frames selected ranged from

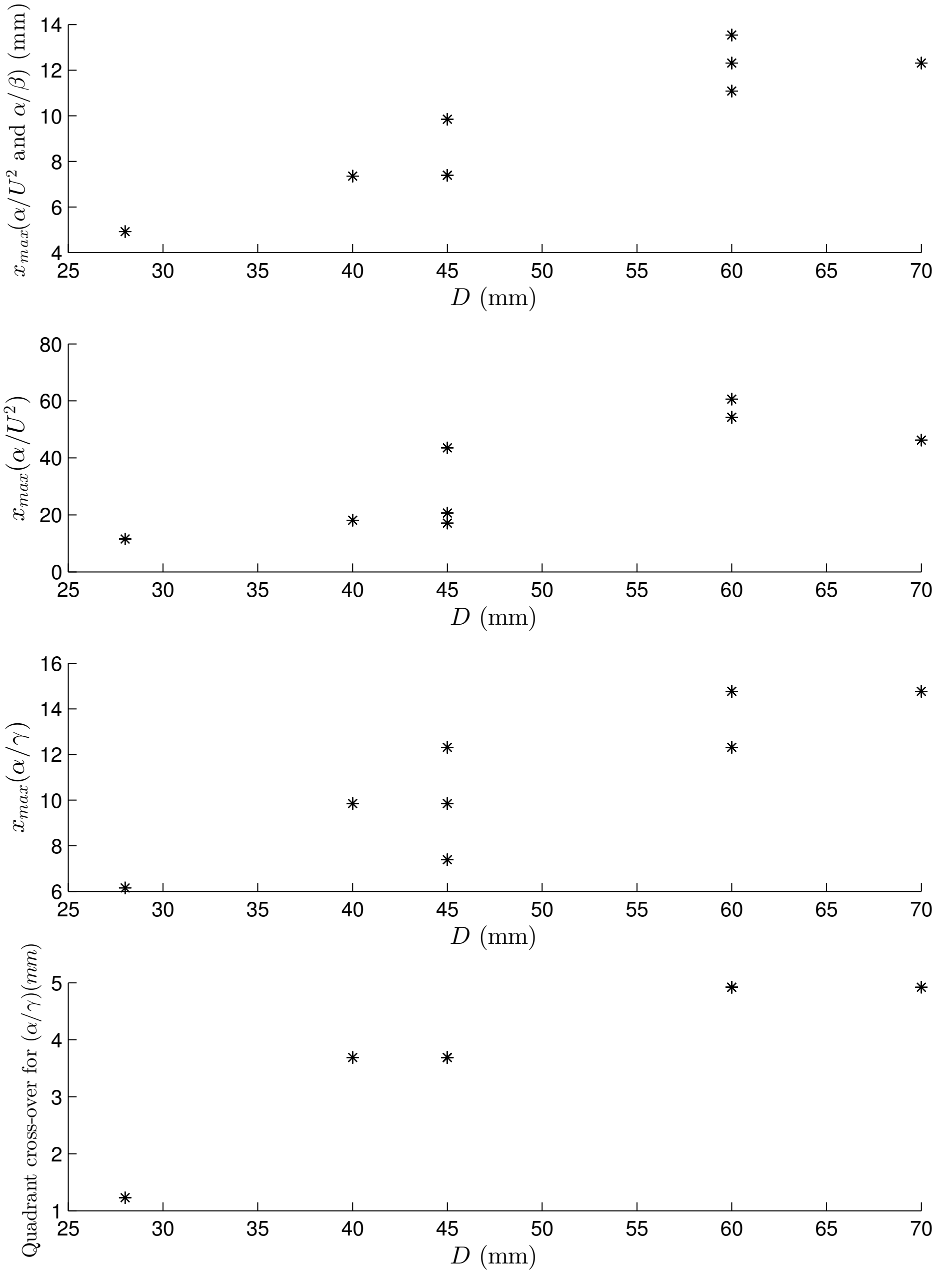

Figure 4.10: The relation between cylinder diameter, the peak stress locations, and the position of the quadrant cross-over for the nine experiments.

5.5 to 7.2% over the nine experiments. The summation of the stress magnitudes exceedance at the peak stress locations of the single points contributed from 27.25 to 32.04% $\sum |u'w'|$ over all frames of each of the different experiment.

The vorticity fields for these frames were then automatically classified into two groups ($K_1$ and $K_2$) using the $K$-Means classifier and the number of frames in each cluster ($C_{k_1}$ and $C_{k_2}$) was extracted. It is clear from the results that experiments 26, 27, 28, and 32 may be grouped together with a clear first cluster dominance and this is true for the single point and whole frame analysis. Fig. 4.8 shows that the peak for $Q_2$ is furthest from the cylinder for these same three experiments.

Table 4.4 shows that this group of experiments share the biggest cylinder diameters. Again the cylinder diameter affects the whole HV system with a similar extent as it does for the near-bed conditions only.

Figure 4.11 shows the centroids for clusters 1 and 2 for the whole frame analysis, and no visual difference can be noticed in comparison with Figure 4.6, hence a relevant explanation is available in relation to Fig. 4.6.

Table 4.6: The number of frames from each experiment allocated to the two clusters found from the $K$-Means analysis ($C_{k_1}$ and $C_{k_2}$), as well as the classifier used to define cluster membership for each experiment $(C_{k_1} - C_{k_2})/(C_{k_1} + C_{k_2})$. The two groups of results represent frames chosen using a single point near the bed on the one hand, and using the whole frame points on the other. Results with a strong positive value for $(C_{k_1} - C_{k_2})/(C_{k_1} + C_{k_2})$ are shown in bold.

| | Single Point | | | Whole Frame | | |
|---|---|---|---|---|---|---|
| Experiment | $C_{k_1}$ | $C_{k_2}$ | $\frac{C_{k_1}-C_{k_2}}{C_{k_1}+C_{k_2}}$ | $C_{k_1}$ | $C_{k_2}$ | $\frac{C_{k_1}-C_{k_2}}{C_{k_1}+C_{k_2}}$ |
| 26 | 285 | 30 | **+0.81** | 282 | 33 | **+0.79** |
| 27 | 281 | 43 | **+0.74** | 258 | 66 | **+0.59** |
| 28 | 284 | 34 | **+0.79** | 294 | 24 | **+0.85** |
| 29 | 3 | 293 | -0.98 | 16 | 280 | -0.89 |
| 30 | 19 | 240 | -0.85 | 88 | 171 | -0.28 |
| 31 | 83 | 209 | -0.43 | 116 | 176 | -0.21 |
| 32 | 260 | 30 | **+0.79** | 266 | 24 | **+0.83** |
| 33 | 11 | 251 | -0.92 | 13 | 249 | -0.9 |
| 34 | 0 | 249 | -1.00 | 0 | 249 | -1.0 |

### 4.2.3 Summation of Turbulent Stresses in Quadrants 1, 3, and 4 in front of the Cylinder

In this section the value of the turbulent stress contribution, of a group of 40 points near the wall upstream of the cylinder based on three quadrants ($Q_1$, $Q_3$, and $Q_4$), is considered for the analysis, where the mean of the absolute turbulent stresses at

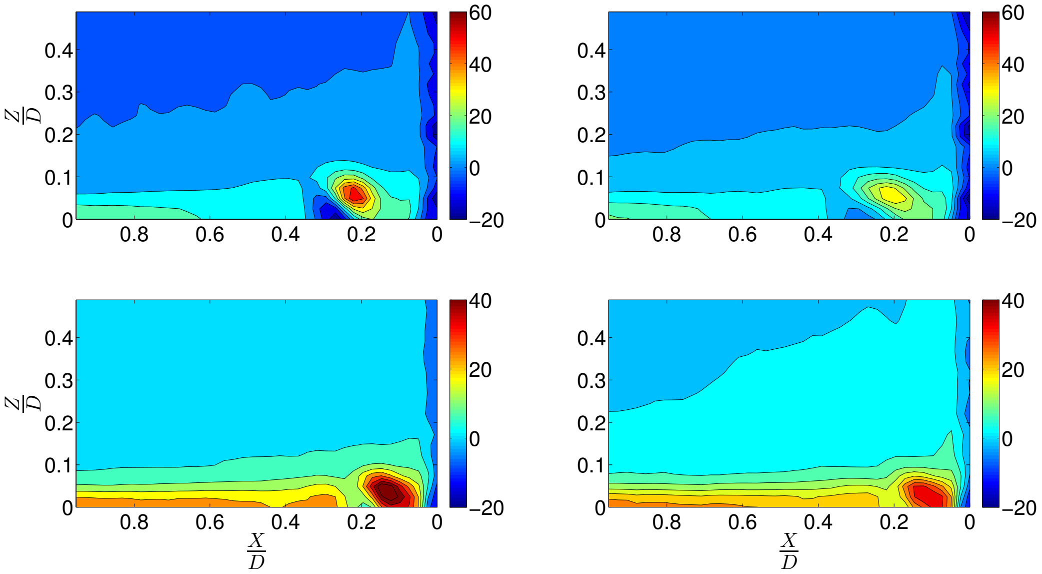

Figure 4.11: The centroids of the clusters extracted from the vorticity fields $\omega$ $(s^{-1})$ over the nine experiments. Results on the left are for the single point analysis while those on the right are for the whole frame method. Centroid of cluster 1 is shown at the top and the centroid of cluster 2 at the bottom in each case. The origin for the horizontal axis is the upstream edge of the cylinder.

each point was chosen as a criterion for the HV system and the point that attained the maximum value was selected to represent the whole group of points. The results of the velocity covariance are shown in Figs. 4.12, 4.13 and 4.14, the abscissa for the points shown, is the distance from the upstream edge of the cylinder. These figures are quite similar to Figures 4.1, 4.2 and 4.3. The only noticed difference is that the magnitudes in the latter figures are less from the formers as the stresses from quadrant 2 are not included.

This section has been added for the need of understanding the effect of quadrant 2 in a better way when its contribution to the stresses is removed. The procedures are similar to Section 4.2.1. The basic data for the stepwise regression analysis are shown in Table 4.7 and the results of the analysis are shown in Table 4.8, in which it is shown that the highest values for the coefficient of determination are for the location of the peak stress and the magnitude of $\eta$. These two relationships are represented in the plots of Fig. 4.15 from top to bottom, respectively. There is a primary cylinder diameter control on the location of the peak near-bed tresses with a secondary effect from the flow depth as the predicting distance is in $mm$. Cylinder diameter Reynolds number is showing a controlling role when the same distance is normalised by the diameter. Froude number control of the peak value of $\eta$ came matched with its control in the cases of low Fr analysed in Section 3.5.2 and Section 3.3.2.1. When $\eta$ normalised by the square of the approaching bulk flow velocity, $\eta/U^2$, the control of $\mathrm{Re}_h$ is the dominant. As in the previous equivalent cases, i.e. the peak stresses normalised by the summation of the stresses in the 40 points, no control parameter was shown. This is a clear evidence that the information that we collected in this set of experiments are not enough to come out with a result about the most effective parameter. So, to explore the normalisation effect for this range of experiments, more data should be collected as part of future studies.

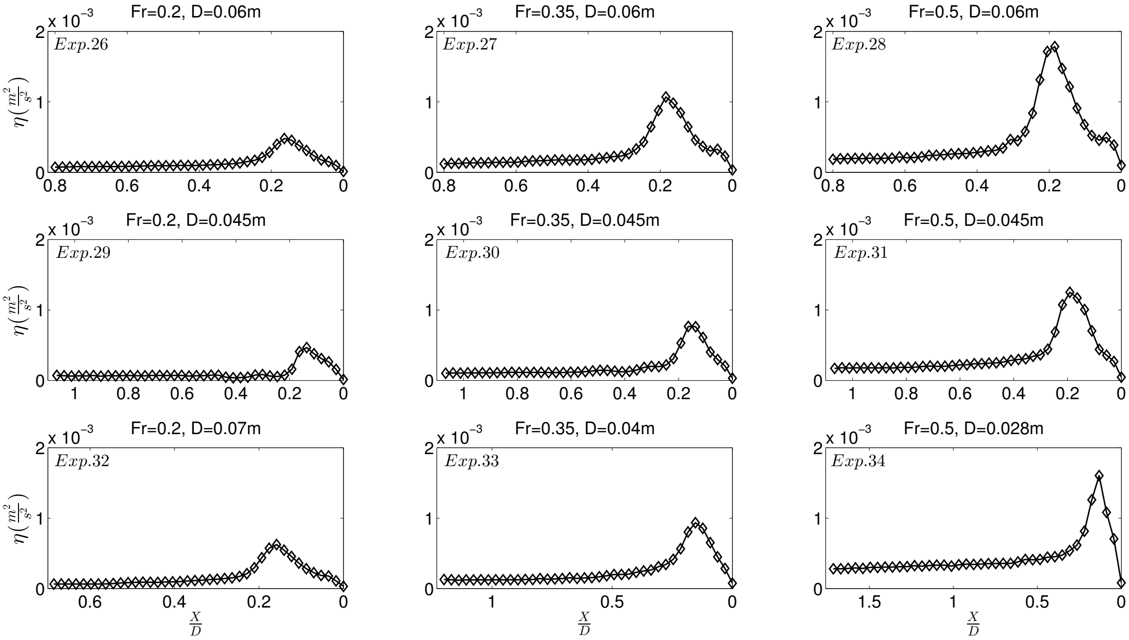

Figure 4.12: Mean of absolute velocity covariances of the summation of the three quadrants ($Q_1$+$Q_3$+$Q_4$) $\eta$. The abscissa indicates distance upstream from the upstream edge of the cylinder. Fr=0.2-0.5.

## 4.3 Discussion

This study shows the importance of adopting an experimental design that permits the separation of the controls upon the geometry and dynamical properties of the HV system. Other studies, Dargahi (1989); Devenport and Simpson (1990); Simpson

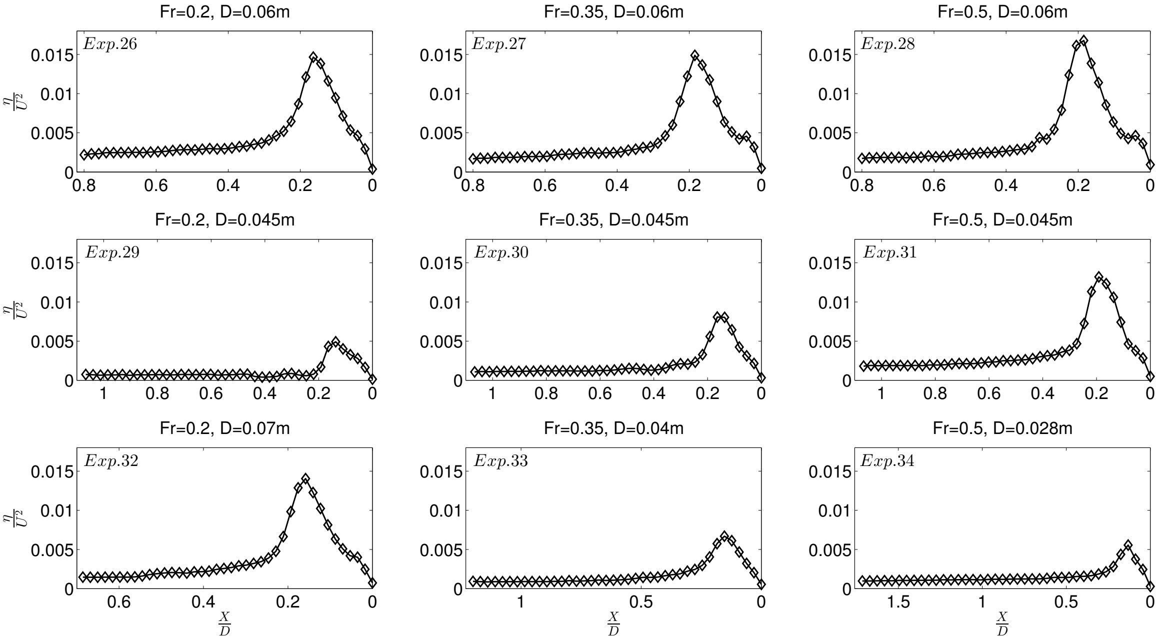

Figure 4.13: Mean of absolute velocity covariances of the summation of the three quadrants ($Q_1$+$Q_3$+$Q_4$) $\eta$ normalized by the square of the approaching bulk flow velocity $\frac{\eta}{U^2}$. The abscissa indicates distance upstream from the upstream edge of the cylinder. Fr=0.2-0.5.

(2001); Escauriaza and Sotiropoulos (2011) found a dependence upon $\mathrm{Re}_D$, but they adopted a single cylinder diameter. It is clearly the case that the dynamics of the *wake* depend upon $\mathrm{Re}_D$ because diameter controls the size of the flow structures in the $X-Y$ plane, while their advection is controlled by $U$. However, in the plane-of-symmetry at the front of the cylinder, the primary vorticity is oriented in the $X-Z$ plane and, as a consequence, it does not necessarily follow that in this region, the dynamics are a function of $\mathrm{Re}_D$.

On one hand, we observe from Section 4.2.1.1, where the summation of absolute turbulent stresses of the four quadrants was considered as a criterion for representing the HV characteristics, that $D$, and Fr control the near-bed stress conditions, in particular the location of the peak stresses and their magnitude $\gamma$ as shown in Table 4.2 and Fig. 4.5. From the results shown in Section 4.2.1.2 we found that the geometry of the HV system in the plane-of-symmetry is a function of $D$ (Table 4.3 and Fig. 4.6). The parameter $D$ can be considered as a key factor that controls the geometry of the HV system as it is shown similar results in the following two

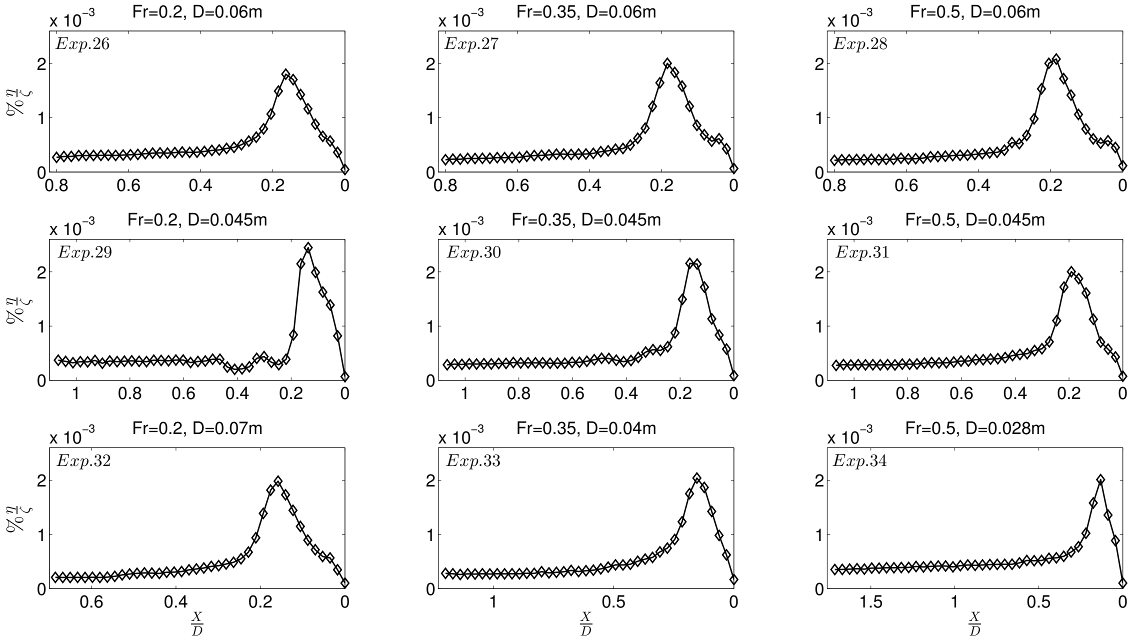

Figure 4.14: Mean of absolute velocity covariances of the summation of the three quadrants ($Q_1$+$Q_3$+$Q_4$) $\eta$ normalized by the summation of the means of absolute velocity covariances over all forty positions $\frac{\eta}{\zeta}$. The abscissa indicates distance upstream from the upstream edge of the cylinder. Fr=0.2-0.5.

sections when depending on the stresses of quadrant 2 as a representing criterion and also when the summation of the stresses in quadrants 1,3, and 4 were considered as a representative criterion.

On the other hand, the results of Section 4.2.2.1, where the absolute turbulent stresses were partitioned into four quadrants and quadrant two was considered as a criterion for representing the HV characteristics, are shown that $D$, $h$ and Fr control the near-bed stress conditions, including the location of peak stress value in quadrant two and their magnitudes. Here, the effect of $h$ came as a new contributor particularly for the location of the peak stresses, and probably is because of the response of quadrant 4 to the flow depth changes. The results from Section 4.2.2.2 represented in Table 4.6 and Fig. 4.11, showed quite similar results to the case when representing the turbulent stresses by the summation values. However, we cannot find evidence in our study that this is a $\mathrm{Re}_D$ control. Instead, it would appear that $D$ and $U$ affect different aspects of the near-wall stress distributions (Tables 4.5 and 4.2). These different findings rise the importance of a systematic investigation of

Table 4.7: Dependent variables used in the stepwise regression for the turbulent stresses. The predictor variables are given in Table 2.2.

| Exp. No. | $x_{max}$ for $\eta$, $\eta/U^2$, and $(\eta/\zeta)$ $(mm)$ | $x_{max}/D$ for $\eta$, $\eta/U^2$, and $\eta/\zeta$ | $\eta_{max}$ $(\times 10^{-4} m^2 s^{-2})$ | $(\eta/U^2)_{max}$ | $(\eta/\zeta)_{max}$ (%) |
|---|---|---|---|---|---|
| 26 | 9.9 | 0.164 | 2.16 | 65.98 | 8.12 |
| 27 | 11.1 | 0.185 | 4.81 | 67.01 | 9.01 |
| 28 | 11.1 | 0.185 | 8.03 | 75.52 | 9.37 |
| 29 | 6.2 | 0.137 | 2.10 | 22.13 | 11.00 |
| 30 | 7.4 | 0.164 | 3.45 | 36.36 | 9.70 |
| 31 | 8.6 | 0.192 | 5.63 | 59.38 | 9.01 |
| 32 | 11.1 | 0.158 | 2.81 | 63.22 | 8.92 |
| 33 | 6.2 | 0.154 | 4.21 | 30.11 | 9.18 |
| 34 | 3.7 | 0.132 | 7.22 | 25.02 | 9.05 |

Table 4.8: The predictor variables contributing significantly to a stepwise regression equation for the selected response variables, together with their significance levels and the $R^2$ associated with the regression equation for the summation of turbulent stresses of quadrants 1, 3, and 4.

| Regression | $R^2$ | Pred. 1 | $p$-value | Pred. 2 | $p$-value |
|---|---|---|---|---|---|
| $x_{max}(\eta, \eta/U^2, \eta/\zeta)$ $(mm)$ | 0.977 | $D$ | $< 0.001$ | $h$ | 0.0038 |
| $x_{max}(\eta, \eta/U^2, \eta/\zeta)$ $(\frac{x_{max}}{D})$ | 0.845 | $\mathrm{Re}_h$ | $< 0.001$ | - | - |
| $\eta_{max}$ | 0.886 | Fr | $< 0.001$ | - | - |
| $(\eta/U^2)_{max}$ | 0.812 | $\mathrm{Re}_h$ | 0.0019 | - | - |
| $(\eta/\zeta)_{max}$ | - | - | - | - | - |

the parameters that affect dynamics of hydraulic phenomena.

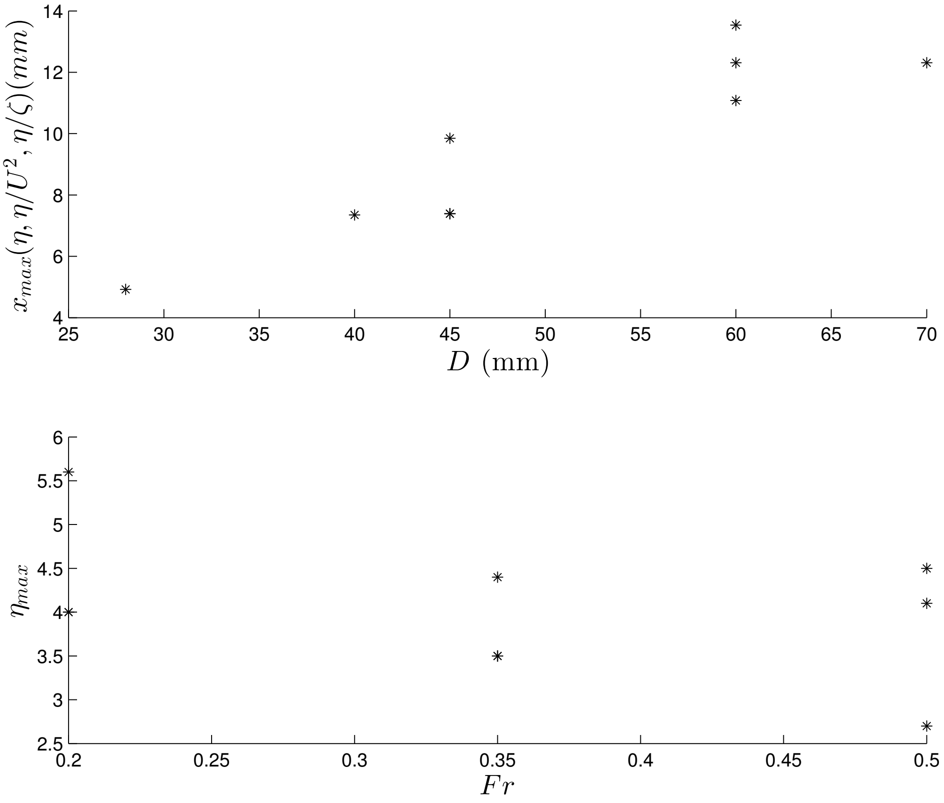

Figure 4.15: The plots above are showing the relationship between the location and magnitude of the peak stress with the cylinder diameter and Froude number in the top and bottom plots respectively.

# Chapter 5

# Conclusions and Future Work

## 5.1 Objectives and Structure of the Chapter

This chapter has three objectives:

1. To summarise the results of the study and present them in summary diagrams.
2. To present the conclusions of this study in both general and specific cases of flow conditions.
3. To highlight and discuss the limitations of the current study and suggest some future research directions.

## 5.2 Summary of Results

In this research, the adopted experimental design covered a wide range of different flow conditions and permitted the separation of the controls upon the geometry and dynamical properties of the HV system. The main goal of this research was to explore the effect of Froude number and other parameters on the behaviour of the horseshoe vortex system upstream of a circular cylinder compared to other studies, we undertook our measurements over a range of flow conditions from low sub-critical to super-critical Froude numbers. Because the applied context for this work was problems such as bed scouring, the attention was focused on the near-bed turbulent stresses.

By systematically controlling $Q$, $D$, $U$ and $h$, it has been possible to examine the Froude number and Reynolds number dependencies more carefully. For the analysis of the independent and dependent parameters of the experiments, multivariate statistical techniques (stepwise regression and $K$-Means classification) were used, the first was used to find the effect of the controlling parameters on the dynamics of the HV system, and the second was used to explore the effect of the same parameters on its geometry.

It would appear that $D$, $h$ and Fr affect different aspects of the near-wall stress distributions in most of the cases analysed in this study rather than the $\mathrm{Re}_D$ as shown from the literature. This difference highlights the value of a systematic investigation of the parameters influencing the dynamics of hydraulic phenomena.

In the following four Figures 5.1, 5.2, 5.3, and 5.4, the results from the analyses of Chapters 3 and 4 are displayed. The three diagrams, shown in Figures 5.1, 5.2, and 5.3, concern the dynamics of the HV system from the stepwise regression analyses. The fourth diagram, shown in Fig. 5.4, summarises the results of the $K$-Means clustering analysis results referring to the geometry characteristics of the HV.

### 5.2.1 The Effect of Different Parameters on the Dynamics of the HV System

The three diagrams shown in Figures 5.1, 5.2, and 5.3, represent the cases when the peak values were chosen from the total stresses, quadrant 2 stresses, and the summation of the stresses in quadrants, 1, 3, and 4 respectively. The three diagrams, include results from the four groups of experiments analysed before in Chapters 3 and 4. These groups of experiments are classified into two sub groups due to the controlling parameters including the location and magnitude of the peak stresses. Then for each case the parameters are sub-divided according to their influence into primary and secondary parameters. For the location part of the diagram, the cylinder diameter was found to be the only parameter that always had an effect on the location of the peak stress values in all of the three selection criteria and the four different groups of experiments, this gives $D$ a fundamental importance as a controlling parameter of the peak location. For the case of quadrant 2, the parameters that affect the location of the peak stresses in all of the four groups are cylinder diameter and flow depth. A cylinder diameter Reynolds number effect appeared when the whole experiments were put together, while the Froude number effect existed in both of the upper sub-critical and super-critical flow conditions as well as in the case of the selected sub-critical flow conditions examined in Chapter 4.

For the magnitude parametrisation, Fr is the most influential parameter for both, the total stresses case and the summation of stresses in quadrants 1, 3, and 4, where it dominates all the groups of experiments except the one for Fr=0.6-2.46. For quadrant 2 stresses criteria, cylinder diameter is the shared control parameter in all ranges of experiments, and in addition to $D$, flow depth and the cylinder diameter Reynolds number have influence in the case of all the experiments and the case of very low sub-critical flow conditions. Froude number has a secondary effect in the case of the selected sub-critical flow conditions.

### 5.2.2 The Effect of Different Parameters on the Geometry of the HV System

The diagram in Fig. 5.4 shows the two approaches used in the analysis of data and it is clear that there is no difference in results when using a single point under the HV system or using the whole frame when representing the high stress instances, and this confirms how the high stress instances in the flow field of the HV system can be represented by the near-bed turbulent stresses rather than the need for snapshots from the whole field. The four groups of experiments are classified into two groups due to the parameter that the frames were clustered. The first set includes both cases with a wide range of Fr (Fr=0.015-2.46) and the high Fr (Fr=0.6-2.46), where the controlling parameter is Fr. For the rest of the experiments represented in groups of Fr=0.015-0.2 and Fr=0.2-0.5, $D$ is the only controlling parameter. It is anticipated, that the effect of $D$ is shown in cases of lower sub-critical flow conditions and reason this was replaced with Fr is attributed to the effect of high flow velocity that pumped energy, and turbulence as a consequence, in the region and caused the high stress instances.

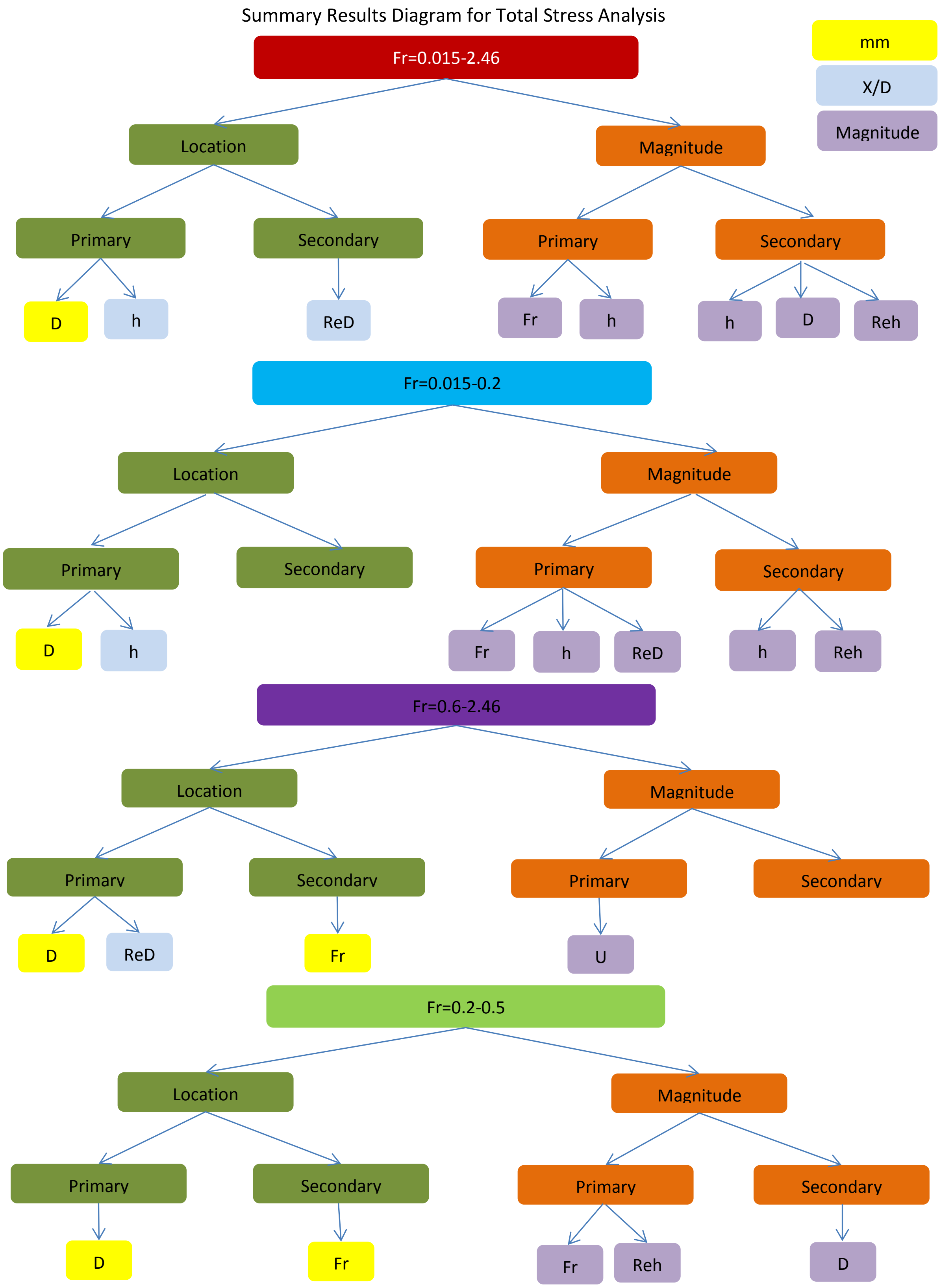

Figure 5.1: The summary diagram of the results of different groups of experiments for the location and magnitude of the peak stress values from the total stresses curve.

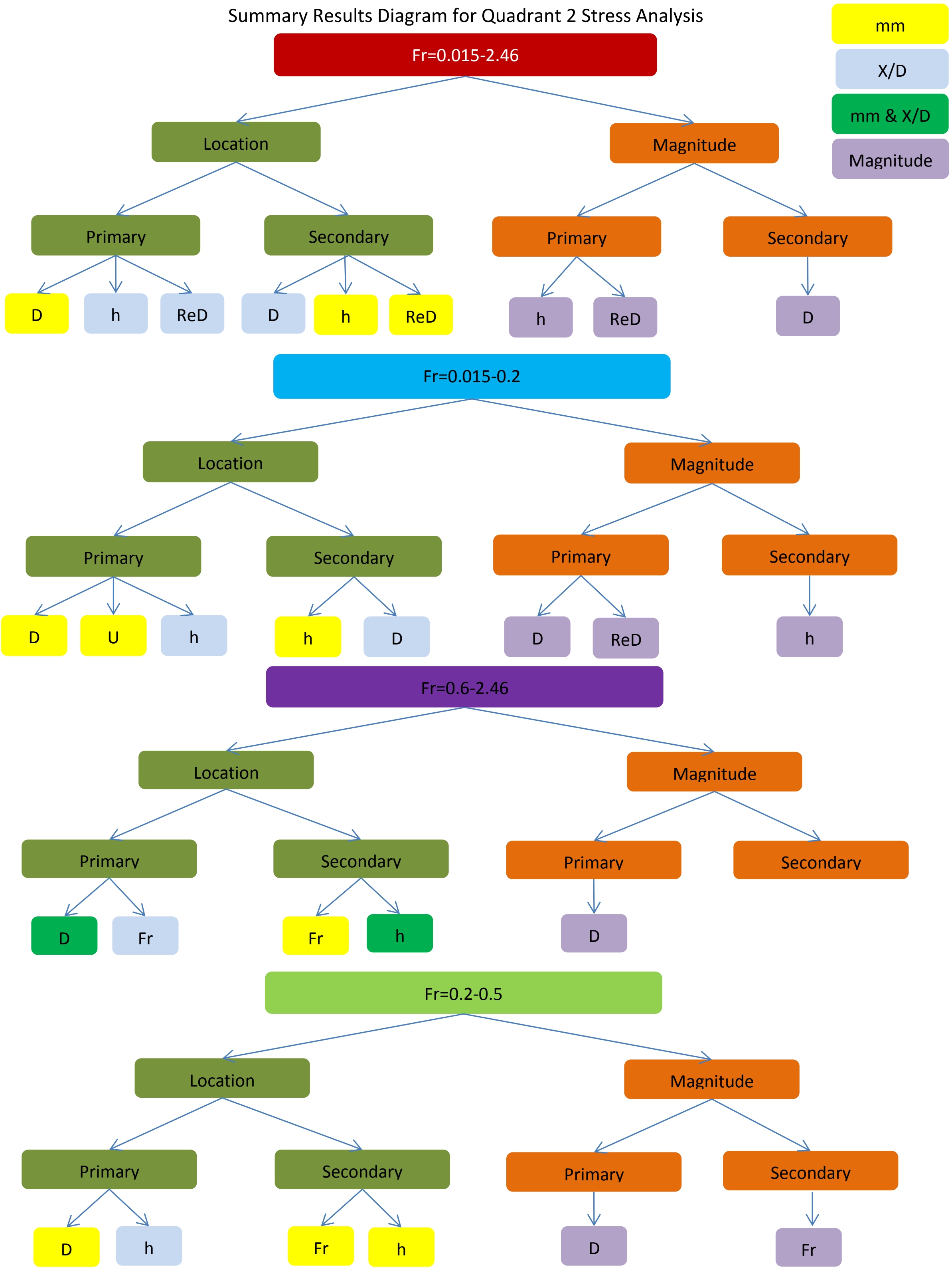

Figure 5.2: The summary diagram of the results of different groups of experiments for the location and magnitude of the peak stress values in quadrant 2 curves.

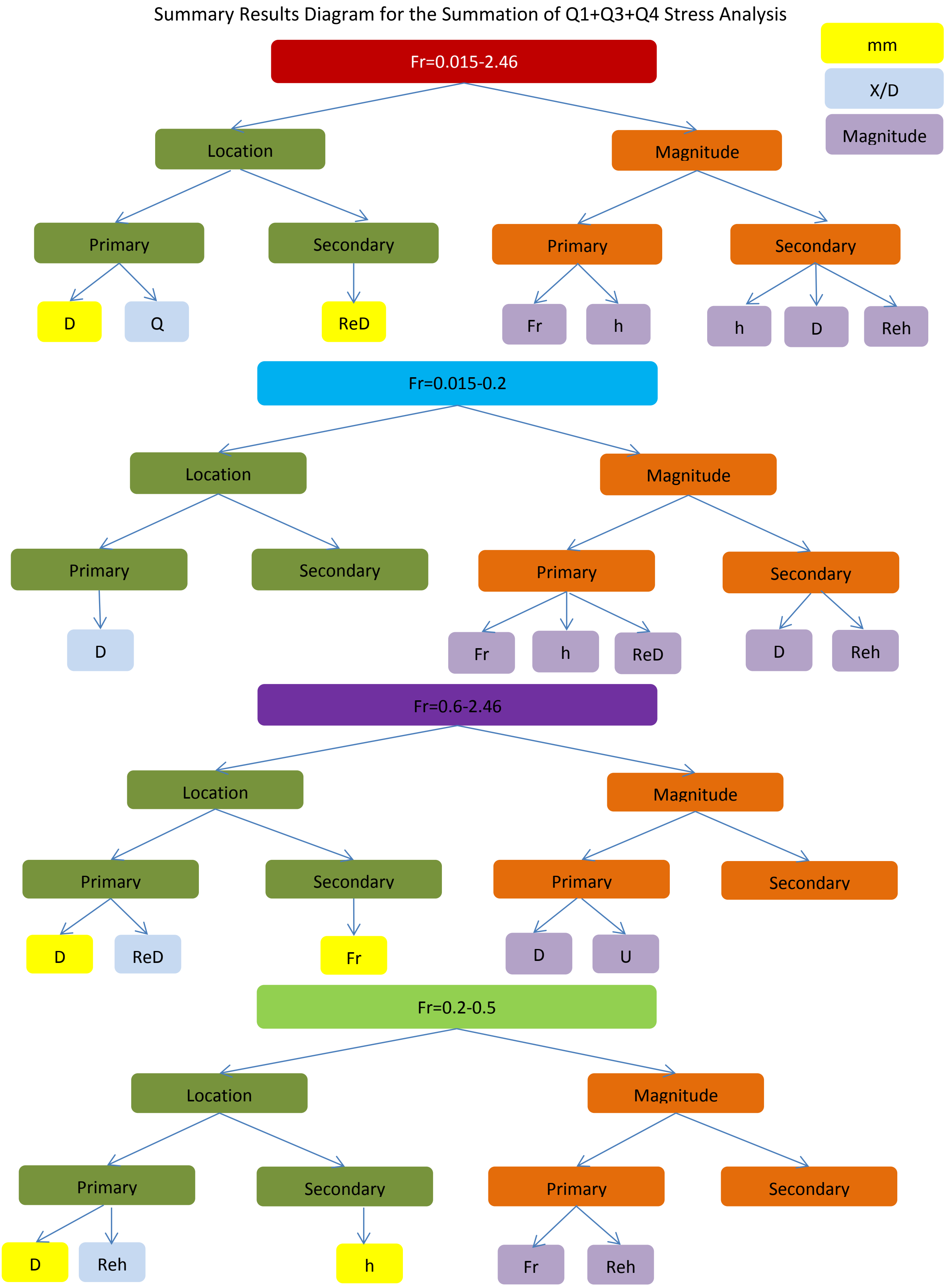

Figure 5.3: The summary diagram of the results of different groups of experiments for the location and magnitude of the peak stress values from the summation of quadrants 1, 3, and 4 curve.

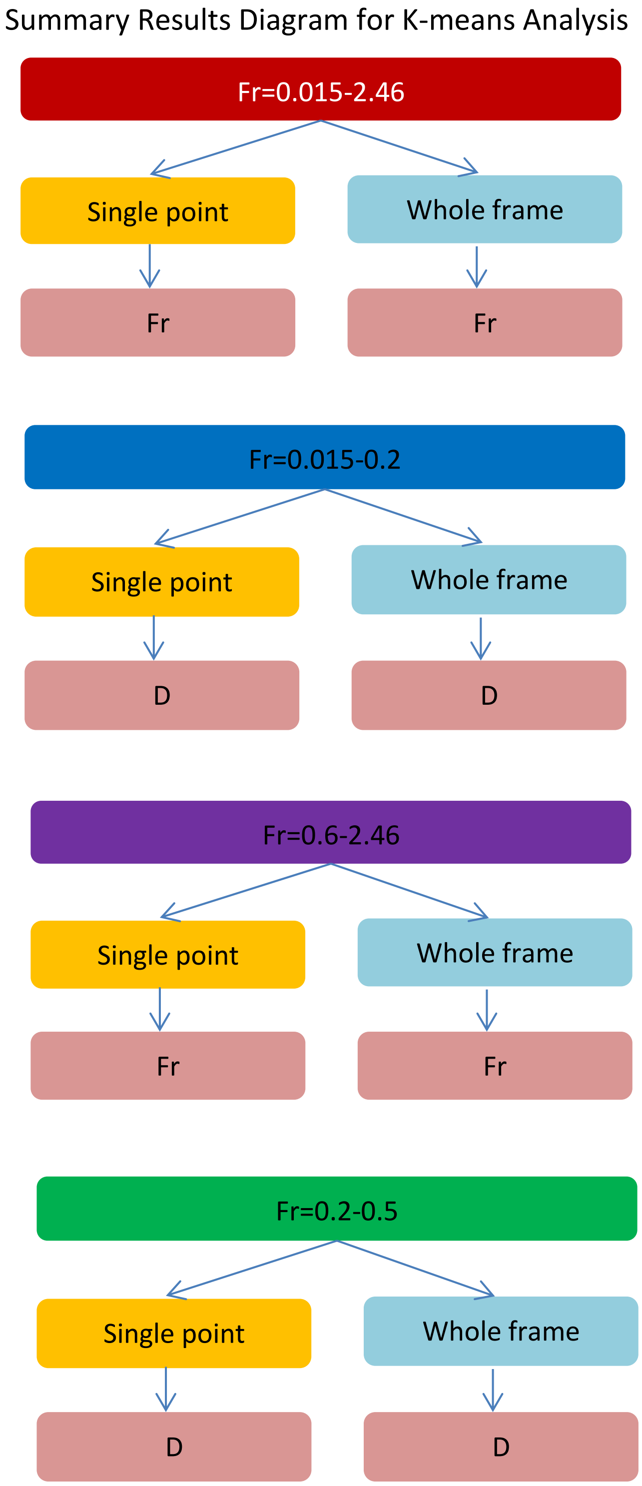

Figure 5.4: The summary diagram of the results of different groups of experiments for the vorticity fields with high instance of stress using the $K$-Means clustering algorithm.

## 5.3 Conclusions

An experimental study was carried out to investigate the controls on the vorticity fields and contributions of the turbulent stresses, (in three different ways, where the results are summarised in Figs. 5.1, 5.2, and 5.3), upstream of a vertically mounted circular cylinder using Particle Image Velocimetry. Experiments under different sub-critical, critical, and super-critical Froude numbers, cylinder diameters, flow depths and flow velocities were analysed. The results revealed some parameters that control the turbulent stresses under the HV system as well as the geometry of the system. From the investigation of the results, it is possible to conclude the following:

1. It was found that the peak stress properties of the HV system are controlled by Fr for the experiments with Fr $\lesssim$ 0.3, and again for the experiments of Fr $\gtrsim$ 1.7. There is no definite parameter control for the peak stresses in the transitional region between these two thresholds. These thresholds can be used as a benchmark for the future numerical studies.

2. The turbulent stresses have a greater magnitude beneath the HV system and, consequently, make a major contribution to scour, as was anticipated. The increase in the turbulent stresses under the HV system was quantified as being a factor of $\sim 2-7$ increase over the background near-wall stresses upstream of the cylinder in the plane of symmetry for most of the dependent variables.

3. For all groups of experiments, the use of the three different criteria shows that cylinder diameter is the main parameter that controls the location of the near-bed peak of the mean stresses values under the HV system. Hence, pier diameters could be used in the prediction of the maximum scour hole location upstream of the circular cylinder. At the same time it confirms the importance of studying dimensional parameters as well as dimensionless ones.

4. It was found that quadrant 2 dominates the stress contributions beneath the

horseshoe vortex system. It is because the boundary layer in the region where HV system exists, behaves like any turbulent boundary layer, where quadrant two is dominant followed by quadrant 4.

5. There are two general topologies for the horseshoe vortex system in the range of the experiments conducted in this study, one of two vortices and the other with one weak vortex, and the extent to which one is expressed is a function of either cylinder diameter, or Fr. There are no major differences in the results when the criterion is either the total stresses, or only the stresses of quadrant 2, concluding that the contribution from quadrants 1, 3, and 4 is not dominant.

6. For the topological classification of the vorticity fields, it is shown that the centroids extracted using a single point approach are more successful in defining the vortices than the whole frame approach. This is because the HV system is commonly attached to the bed and in the whole frame analysis there are other effects arising such as vorticity away from the bed. This finding makes it easier to represent the HV system by the near-bed turbulent stresses rather than the need of the instances from the whole field.

7. The percentage of number of frames that exceeds a threshold of hole size $H > 2$ is between 4.84% and 7.02% in all cases and the contribution value of stresses in these cases found to be between 24.68% and 40.93%, these values may be considered for the validation of numerical studies within this range of flow conditions. These results have been found from studying a region of $X = 48\ mm$ and $Z = 24\ mm$ in the plane of symmetry just upstream of circular cylinders.

8. It has been found that the POD method captured more vorticity structures, with three vortices found in most cases, while in $K$-Means clustering the centroids of the clusters showed either one or two vortices. This may be attributed to the differences between these methods, with frames with a greater number of vortices located somewhere else in the clustering space and not well repre-

sented by the centroids.

9. As different parameters have been found to affect the different aspects of the near-wall turbulent stress distribution, and particularly $D$, Fr, and $h$, as the most influential parameters, a systematic investigation of the parameters influencing the dynamics of hydraulic phenomena is a valuable thing to be done.

Overall, the results in Chapters 3 and 4 demonstrated that the study of the effect of the dimensional and dimensionless parameters on the HV dynamics upstream of a circular cylinder in a wide range of flow conditions has resulted in a better understanding of the controlling parameters. The results are also encouraging and suggest that the near-bed shear stresses are good measures for representing the HV characteristics.

## 5.4 Future Work

There is a need for future work on this topic mainly for two reasons: to obtain additional validation using different instrumentation and analysis methods; To explore additional features of the flow that could not be investigated at the time.

***More experiments to be done***: There is a need to conduct experiments in the transitional region that we defined earlier in order to find the exact parameters that affect the dynamics of the HV system and how the topology of the HV system varies as a function of these parameters, particularly for the high Fr cases.

***Velocity measurements***: Repeating the same experiments and collecting long duration time series at high temporal resolution using laser doppler velocimetry near the bed to understand the oscillation of the system. From these measurements the spectra of the velocity components can be found and the frequency of the vorticies can be determined and added to the characteristics of the HV system for each flow condition. In addition this will make studying the behaviour of the instantaneous change of the horseshoe dynamics in both the horizontal and vertical planes possible, particularly for the high Froude number cases where numerical simulations are still a challenge.

***Numerical simulations***: It is recommended to have numerical simulations for the cases that we have in our experiments, using Detached Eddy Simulation as used by Escauriaza and Sotiropoulos (2011). For the free surface modelling, which is necessary for higher Froude numbers, Volume of Fluid methods can be used in combination with a Navier Stokes solver to simulate free-surface deformations (Löhner et al., 2007).

***Downstream flow measurements***: Due to the lack of information about the behaviour of the HV system downstream of the cylinder in the range of flow conditions of this study, there is a need to study the region downstream of the cylinder and see if there is a correlation between the characteristics of the HV system in both, the upstream and downstream regions, particularly for the shallow flow cases where the wake vortex shedding is more effective, where Baker (1979, 1980) found that the shedding frequency of the wake vortex is independent of the oscillation of the HV system.

***A real scale measurements***: It will be of an interest to see how measurements for the real scale flow field upstream of actual structures under natural boundary conditions compare with the experimental work, and if vortex size still scales with the size of the obstacle or if there are constraints that limit the nature of the scaling.

***Monitoring of water surface fluctuations***: A study is needed to explore if there is any relationship between the water surface fluctuations and the oscillation of the Horseshoe vortex system upstream of the obstacle. There is ambiguity about the effect of the water surface fluctuations on the HV system where the literature shows no study addressed this issue.

# Bibliography

Adrian, R. J. and Westerweel, J. (2011), *Particle image velocimetry*, Vol. 30, Cambridge University Press.

Akan, A. O. (2011), *Open channel hydraulics*, Butterworth-Heinemann.

Ashworth, P., Bennett, S., Best, J. and McLelland, S. (1996), *Coherent flow structures in open channels*, John Wiley and Sons.

Baker, C. (1979), 'The laminar horseshoe vortex', *Journal of Fluid Mechanics* **95**(02), 347–367.

Baker, C. (1980), 'The turbulent horseshoe vortex', *Journal of Wind Engineering and Industrial Aerodynamics* **6**(1), 9–23.

Baker, C. (1991), 'The oscillation of horseshoe vortex systems', *Journal of Fluids Engineering* **113**(3), 489–495.

Bakewell Jr, H. P. and Lumley, J. L. (1967), 'Viscous sublayer and adjacent wall region in turbulent pipe flow', *Physics of Fluids* **10**(9), 1880–1889.

Berkooz, G., Holmes, P. and Lumley, J. L. (1993), 'The Proper Orthogonal Decomposition in the analysis of turbulent flows', *Annual Review of Fluid Mechanics* **25**(1), 539–575.

Bogard, D. and Tiederman, W. (1986), 'Burst detection with single-point velocity measurements', *Journal of Fluid Mechanics* **162**, 389–413.

Bolsin, S. and Colson, M. (2000), 'The use of the cusum technique in the assessment of trainee competence in new procedures', *International Journal for Quality in Health Care* **12**(5), 433–438.

Brevis, W. and García-Villalba, M. (2011), 'Shallow-flow visualization analysis by Proper Orthogonal Decomposition', *Journal of Hydraulic Research* **49**, 586–594.

Briaud, J.-L., Ting, F. C., Chen, H., Gudavalli, R., Perugu, S. and Wei, G. (1999), 'Sricos: Prediction of scour rate in cohesive soils at bridge piers', *Journal of Geotechnical and Geoenvironmental Engineering* **125**(4), 237–246.

Cai, W.-H., Li, F.-C., Zhang, H.-N., Li, X.-B., Yu, B., Wei, J.-J., Kawaguchi, Y. and Hishida, K. (2009), 'Study on the characteristics of turbulent drag-reducing channel flow by particle image velocimetry combining with proper orthogonal decomposition analysis', *Physics of Fluids* **21**(11), 115103.

Castro, I. P. (2009), Turbulent flow over rough walls, *in* 'Advances in Turbulence XII', Springer, pp. 381–388.

Chakraborty, P., Balachandar, S. and Adrian, R. J. (2005), 'On the relationships between local vortex identification schemes', *Journal of Fluid Mechanics* **535**, 189–214.

Chang, W., Constantinescu, G., Tsai, W. and Lien, H. (2011), 'Coherent structure dynamics and sediment erosion mechanisms around an in-stream rectangular cylinder at low and moderate angles of attack', *Water Resources Research* **47**(12).

Chatfield, C. (1996), *The analysis of time series: an introduction*, CRC press.

Chevillard, L., Lévêque, E., Taddia, F., Meneveau, C., Yu, H. and Rosales, C. (2011), 'Local and nonlocal pressure hessian effects in real and synthetic fluid turbulence', *Physics of Fluids* **23**(9), 095108.

Christensen, K. and Scarano, F. (2015), 'Uncertainty quantification in particle image velocimetry', *Measurement Science and Technology* **26**(7), 070201.

Constantinescu, G. and Koken, M. (2005), 'Time dependent and time averaged turbulence structure of flow past a surface mounted cylinder', *Proc. 4-th ICCHMT, Paris, France* (139), 1–3.

Dargahi, B. (1989), 'The turbulent flow field around a circular cylinder', *Experiments in Fluids* **8**(1-2), 1–12.

Devenport, W. J. and Simpson, R. L. (1990), ‘Time-dependent and time-averaged turbulence structure near the nose of a wing-body junction’, *Journal of Fluid Mechanics* **210**, 23–55.

Donoho, D. L. and Johnstone, J. M. (1994), ‘Ideal spatial adaptation by wavelet shrinkage’, *Biometrika* **81**(3), 425–455.

Dubief, Y. and Delcayre, F. (2000), ‘On coherent-vortex identification in turbulence’, *Journal of Turbulence* **1**(1), 011–011.

Escauriaza, C. and Sotiropoulos, F. (2011), ‘Reynolds number effects on the coherent dynamics of the turbulent horseshoe vortex system’, *Flow, Turbulence and combustion* **86**(2), 231–262.

Everitt, B. S., Landau, S., Leese, M. and Stahl, D. (2011), ‘Hierarchical clustering’, *Cluster Analysis, 5th Edition* pp. 71–110.

Fage, A. and Falkner, V. (1931), *Further experiments on the flow around a circular cylinder*, HM Stationery Office.

Goring, D. G. and Nikora, V. I. (2002), ‘Despiking acoustic doppler velocimeter data’, *Journal of Hydraulic Engineering* **128**(1), 117–126.

Grant, H. (1958), ‘The large eddies of turbulent motion’, *Journal of Fluid Mechanics* **4**(02), 149–190.

Guide, U. (2012), ‘Dantec dynamicstudio users guide’.

Gurka, R., Liberzon, A. and Hetsroni, G. (2006), ‘POD of vorticity fields: A method for spatial characterization of coherent structures’, *International Journal of Heat and Fluid Flow* **27**(3), 416–423.

Heathershaw, A. D. and Thorne, P. D. (1985), ‘Sea-bed noises reveal role of turbulent bursting phenomenon in sediment transport by tidal currents’, *Nature* **316**, 339–342.

Hill, D. F. and Younkin, B. D. (2006), ‘PIV measurements of flow in and around scour holes’, *Experiments in Fluids* **41**(2), 295–307.

Hunt, J. C., Wray, A. and Moin, P. (1988), ‘Eddies, streams, and convergence zones in turbulent flows’.

Hussain, A. F. (1983), ‘Coherent structures reality and myth’, *Physics of Fluids* **26**(10), 2816–2850.

Jeong, J. and Hussain, F. (1995), ‘On the identification of a vortex’, *Journal of Fluid Mechanics* **285**, 69–94.

Kawamura, T., Mayer, S., Garapon, A. and Sørensen, L. (2002), ‘Large eddy simulation of a flow past a free surface piercing circular cylinder’, *Journal of Fluids Engineering* **124**(1), 91–101.

Keffer, J. (1965), ‘The uniform distortion of a turbulent wake’, *Journal of Fluid Mechanics* **22**(01), 135–159.

Keylock, C. J. (2007), ‘The visualisation of turbulence data using a wavelet-based method’, *Earth Surface Processes and Landforms* **32**, 637–647.

Keylock, C. J. (2015), ‘Flow resistance in natural, turbulent channel flows: The need for a fluvial fluid mechanics’, *Water Resources Research* **51**(6), 4374–4390.

Khosronejad, A., Kang, S. and Sotiropoulos, F. (2012), ‘Experimental and computational investigation of local scour around bridge piers’, *Advances in Water Resources* **37**, 73–85.

Kirkil, G. and Constantinescu, G. (2012), ‘A numerical study of the laminar necklace vortex system and its effect on the wake for a circular cylinder’, *Physics of Fluids* **24**(7), 073602.

Kirkil, G., Constantinescu, G. and Ettema, R. (2005*a*), The horseshoe vortex system around a circular bridge pier on equilibrium scoured bed, *in* ‘World water and environmental resources congress, Alaska’.

Kirkil, G., Constantinescu, G. and Ettema, R. (2009), ‘Detached eddy simulation investigation of turbulence at a circular pier with scour hole’, *Journal of Hydraulic Engineering* **135**(11), 888–901.

Kirkil, G., Constantinescu, S. and Ettema, R. (2005*b*), The horseshoe vortex system around a circular bridge pier on a flat bed, *in* 'XXXIst International Association Hydraulic Research Congress, Seoul, Korea, pp.1-10'.

Kirkil, G., Constantinescu, S. and Ettema, R. (2006), Investigation of the velocity and pressure fluctuations distributions inside the turbulent horseshoe vortex system around a circular bridge pier, *in* 'River Flow', pp. 709–718.

Kirkil, G., Constantinescu, S. and Ettema, R. (2008), 'Coherent structures in the flow field around a circular cylinder with scour hole', *Journal of Hydraulic Engineering* **134**(5), 572–587.

Kline, S., Reynolds, W., Schraub, F. and Runstadler, P. (1967), 'The structure of turbulent boundary layers', *Journal of Fluid Mechanics* **30**(04), 741–773.

Kostas, J., Soria, J. and Chong, M. (2005), 'A comparison between snapshot POD analysis of PIV velocity and vorticity data', *Experiments in Fluids* **38**(2), 146–160.

Kurniawan, A. and Altinakar, M. S. (2002), Velocity and turbulence measurements in a scour hole using an acoustic Doppler velocity profiler, *in* 'Proceedings of the third international symposium on ultrasonic Doppler methods for fluid mechanics and fluid engineering, Lausanne, Switzerland', pp. 37–43.

Landreth, C. C. and Adrian, R. J. (1990), 'Impingement of a low Reynolds number turbulent circular jet onto a flat plate at normal incidence', *Experiments in Fluids* **9**(1-2), 74–84.

Lin, C., Chiu, P.-H. and Shieh, S.-J. (2002), 'Characteristics of horseshoe vortex system near a vertical plate–base plate juncture', *Experimental Thermal and Fluid Science* **27**(1), 25–46.

Lin, C., Ho, T. C. and Dey, S. (2008), 'Characteristics of steady horseshoe vortex system near junction of square cylinder and base plate', *Journal of Engineering Mechanics* **134**(2), 184–197.

Lin, C., Lai, W.-J. and Chang, K.-A. (2003), 'Simultaneous particle image velocimetry and laser Doppler velocimetry measurements of periodical oscillatory horseshoe vortex system near square cylinder-base plate juncture', *Journal of Engineering Mechanics* **129**(10), 1173–1188.

Löhner, R., Yang, C. and Oñate, E. (2007), 'Simulation of flows with violent free surface motion and moving objects using unstructured grids', *International Journal for Numerical Methods in Fluids* **53**(8), 1315–1338.

Lu, S. and Willmarth, W. (1973), 'Measurements of the structure of the Reynolds stress in a turbulent boundary layer', *Journal of Fluid Mechanics* **60**(03), 481–511.

Lumley, J. L. (1967), 'The structure of inhomogeneous turbulent flows', *Atmospheric Turbulence and Radio Wave Propagation* pp. 166–178.

Nakagawa, H. and Nezu, I. (1977), 'Prediction of the contributions to the Reynolds stress from bursting events in open-channel flows', *Journal of Fluid Mechanics* **80**(01), 99–128.

Nelson, J. M., Shreve, R. L., McLean, S. R. and Drake, T. G. (1995), 'Role of near-bed turbulence structure in bed load transport and bed form mechanics', *Water Resources Research* **31**, 2071–2086.

Norman, R. S. (1972), On obstacle generated secondary flows in laminar boundary layers and transition to turbulence, PhD thesis, Illinois Institute of Technology Chicago, IL, USA.

Olsen, N. R. and Kjellesvig, H. M. (1998), 'Three-dimensional numerical flow modeling for estimation of maximum local scour depth', *Journal of Hydraulic Research* **36**(4), 579–590.

Paik, J., Escauriaza, C. and Sotiropoulos, F. (2007), 'On the bimodal dynamics of the turbulent horseshoe vortex system in a wing-body junction', *Physics of Fluids* **19**(4), 045107.

Paik, J., Escauriaza, C. and Sotiropoulos, F. (2010), 'Coherent structure dynamics in turbulent flows past in-stream structures: Some insights gained via numerical simulation', *Journal of Hydraulic Engineering* **136**(12), 981–993.

Pattenden, R., Turnock, S. and Zhang, X. (2005), ‘Measurements of the flow over a low-aspect-ratio cylinder mounted on a ground plane’, *Experiments in Fluids* **39**(1), 10–21.

Pham, D. T., Dimov, S. S. and Nguyen, C. (2005), ‘Selection of k in k-means clustering’, *Proceedings of the Institution of Mechanical Engineers, Part C: Journal of Mechanical Engineering Science* **219**(1), 103–119.

Press, S. J. (2012), *Applied multivariate analysis: using Bayesian and frequentist methods of inference*, Courier Corporation.

Quadrio, M. and Luchini, P. (2003), ‘Integral space-time scales in turbulent wall flows’, *Physics of Fluids* **15**(8), 2219–2227.

Rajagopalan, S. and Antonia, R. (1982), ‘Use of a quadrant analysis technique to identify coherent structures in a turbulent boundary layer’, *Physics of Fluids* **25**(6), 949–956.

Richardson, J. E. and Panchang, V. G. (1998), ‘Three-dimensional simulation of scour-inducing flow at bridge piers’, *Journal of Hydraulic Engineering* **124**(5), 530–540.

Rodríguez y Domínguez, M., Romero-Méndez, R., Ramos-Paláu, M. and Pérez-Gutiérrez, F. G. (2006), ‘The laminar horseshoe vortex upstream of a short-cylinder confined in a channel formed by a pair of parallel plates’, *Journal of Visualization* **9**(3), 309–318.

Roper, A. T. (1967), A cylinder in a turbulent shear layer, PhD thesis, Colorado State University.

Roshko, A. (1961), ‘Experiments on the flow past a circular cylinder at very high Reynolds number’, *Journal of Fluid Mechanics* **10**(03), 345–356.

Roulund, A., Sumer, B. M., Fredsøe, J. and Michelsen, J. (2005), ‘Numerical and experimental investigation of flow and scour around a circular pile’, *Journal of Fluid Mechanics* **534**, 351–401.

Sahin, B., Akilli, H., Karakus, C., Akar, M. A. and Ozkul, E. (2010), ‘Qualitative and quantitative measurements of horseshoe vortex formation in the junction of horizontal and vertical plates’, *Measurement* **43**(2), 245–254.

Sahin, B., Ozturk, N. A. and Akilli, H. (2007), ‘Horseshoe vortex system in the vicinity of the vertical cylinder mounted on a flat plate’, *Flow Measurement and Instrumentation* **18**(2), 57–68.

Salaheldin, T. M., Imran, J. and Chaudhry, M. H. (2004), ‘Numerical modeling of three-dimensional flow field around circular piers’, *Journal of Hydraulic Engineering* **130**(2), 91–100.

Sarkar, S. and Dey, S. (2010), ‘Double-averaging turbulence characteristics in flows over a gravel bed’, *Journal of Hydraulic Research* **48**(6), 801–809.

Schwind, R. G. (1962), The three dimensional boundary layer near a strut, PhD thesis, Massachusetts Institute of Technology, Department of Mechanical Engineering.

Seal, C., Smith, C., Akin, O. and Rockwell, D. (1995), ‘Quantitative characteristics of a laminar, unsteady necklace vortex system at a rectangular block-flat plate juncture’, *Journal of Fluid Mechanics* **286**, 117–135.

Sharma, S. (1988), Experimental investigation of vortex flow and its modification around wall/cylinder junctions, PhD thesis, PhD thesis, IIT, Kanpur, India.

Simons, D. B. and Richardson, E. V. (1961), ‘Forms of bed roughness in alluvial channel’, *Journal of the Hydraulics Division* **87**(3), 87–105.

Simpson, R. L. (2001), ‘Junction flows’, *Annual Review of Fluid Mechanics* **33**(1), 415–443.

Song, C. C. and Yuan, M. (1990), ‘Simulation of vortex-shedding flow about a circular cylinder at high Reynolds numbers’, *Journal of Fluids Engineering* **112**(2), 155–161.

Sumer, B. M., Christiansen, N. and Fredsøe, J. (1997), 'The horseshoe vortex and vortex shedding around a vertical wall-mounted cylinder exposed to waves', *Journal of Fluid Mechanics* **332**, 41–70.

Thomas, A. S. (1987), 'The unsteady characteristics of laminar juncture flow', *Physics of Fluids* **30**(2), 283–285.

Townsend, A. (1976), 'The structure of turbulent shear flow', *Cambridge UP, Cambridge* .

Travin, A., Shur, M., Strelets, M. and Spalart, P. (2000), 'Detached-eddy simulations past a circular cylinder', *Flow, Turbulence and Combustion* **63**(1-4), 293–313.

Tseng, M.-H., Yen, C.-L. and Song, C. (2000), 'Computation of three-dimensional flow around square and circular piers', *International Journal for Numerical Methods in Fluids* **34**(3), 207–227.

Venditti, J. G., Best, J. L., Church, M. and Hardy, R. J. (2013), *Coherent Flow Structures at Earth's Surface*, John Wiley & Sons.

Wang, M. and Moin, P. (2002), 'Dynamic wall modeling for large-eddy simulation of complex turbulent flows', *Physics of Fluids* **14**(7), 2043–2051.

Westerweel, J. and Scarano, F. (2005), 'Universal outlier detection for PIV data', *Experiments in Fluids* **39**(6), 1096–1100.

Yanmaz, A. M. and Ustun, I. (2001), 'Generalized reliability model for local scour around bridge piers of various shapes', *Turkish Journal of Engineering and Environmental Sciences* **25**(6), 687–698.